

# Characterization of coronary atherosclerosis on computed tomography using advanced image processing techniques

PhD Thesis

**Márton József Kolossváry MD**

Doctoral School of Basic and Translational Medicine

Semmelweis University



Supervisor: Pál Maurovich-Horvat MD, PhD

Official reviewers: Pál Kaposi Novak MD, PhD

Gál Viktor MD, PhD

Head of the Complex Examination Committee:

Tivadar Tulassay MD, PhD

Members of the Complex Examination Committee:

Attila Patócs MD, PhD

Péter Andrkéa MD, PhD

Budapest

2020

# TABLE OF CONTENTS

<b>1. INTRODUCTION</b> .....	<b>6</b>
<b>1.1. Imaging atherosclerosis using CTA in clinical practice</b> .....	<b>8</b>
<b>1.2. Assessment of plaque composition using coronary CTA</b> .....	<b>9</b>
1.2.1. Degree of calcification.....	9
1.2.2. Plaque attenuation pattern.....	10
<b>1.3. Assessment of high-risk plaque features using coronary CTA</b> .....	<b>12</b>
1.3.1. Napkin-ring sign.....	12
1.3.2. Low attenuation .....	13
1.3.3. Spotty calcification .....	14
1.3.4. Positive remodeling .....	15
<b>1.4. Assessment of stenosis degree using coronary CTA</b> .....	<b>17</b>
<b>1.5. Radiomics: the potential to objectively analyze radiological images</b> .....	<b>19</b>
1.5.1. Intensity-based metrics .....	21
1.5.2. Texture-based metrics.....	23
1.5.3. Shape-based metrics .....	28
1.5.4. Transform-based metrics.....	29
<b>1.6. Artificial intelligence: the hope to synthesize it all</b> .....	<b>31</b>
<b>2. OBJECTIVES</b> .....	<b>33</b>
<b>2.1. Defining the effect of using coronary CTA to assess coronary plaque burden as opposed to ICA</b> .....	<b>33</b>
<b>2.2. Defining the potential of using radiomics to identify napkin-ring sign plaques on coronary CTA</b> .....	<b>33</b>
<b>2.3. Defining the potential of radiomics to identify invasive and radionuclide imaging markers of vulnerable plaques on coronary CTA</b> .....	<b>33</b>

2.4. Defining the potential effect of image reconstruction algorithms on reproducibility of volumetric and radiomic signatures of coronary lesions on coronary CTA .....	34
2.5. Defining the potential of using radiomic markers as inputs to machine learning models to identify advanced atherosclerotic lesions as assessed by histology .....	34
3. <i>METHODS</i> .....	35
3.1. Study design and statistics for defining the effect of using coronary CTA to assess coronary plaque burden as opposed to ICA.....	35
3.2. Study design and statistics for defining the potential of using radiomics to identify napkin-ring sign plaques on coronary CTA.....	37
3.3. Study design and statistics for defining the potential of radiomics to identify invasive and radionuclide imaging markers of vulnerable plaques on coronary CTA	40
3.4. Study design and statistics for defining the potential effect of image reconstruction algorithms on reproducibility of volumetric and radiomic signatures of coronary lesions on coronary CTA .....	43
3.5. Study design and statistics for defining the potential of using radiomic markers as inputs to machine learning models to identify advanced atherosclerotic lesions as assessed by histology.....	46
4. <i>RESULTS</i> .....	50
4.1. Comparison of quantity of coronary atherosclerotic plaques detected by coronary CTA versus ICA.....	50
4.2. Identification of napkin-ring sign plaques using radiomics .....	53
4.3. Identification of invasive and radionuclide imaging markers of vulnerable plaques using radiomic analysis of coronary CTA .....	64
4.4. Effect of image reconstruction algorithms on volumetric and radiomics features derived from coronary CTA .....	69

4.5. Identification of advanced atherosclerotic images using radiomics-based machine learning validated using histology .....	74
5. <i>DISCUSSION</i> .....	80
5.1. Coronary CTA for the characterization of plaque burden .....	80
5.2. Potential of radiomics to identify napkin-ring sign plaques.....	82
5.3. Possibility to identify radionuclide and invasive imaging markers using non-invasive coronary CTA.....	85
5.4. Robustness of volumetric and radiomic features to image reconstruction algorithms .....	89
5.5. Potential of radiomics-based machine learning to classify coronary lesions to corresponding histology categories .....	91
6. <i>CONCLUSIONS</i> .....	93
7. <i>SUMMARY</i> .....	96
8. <i>ÖSSZEFOGLALÁS</i> .....	97
9. <i>BIBLIOGRAPHY</i> .....	98
10. <i>CANDIDATE'S PUBLICATIONS</i> .....	124
10.1. Publications discussed in the present thesis .....	124
10.2. Publications not related to the present thesis.....	124
11. <i>ACKNOWLEDGEMENTS</i> .....	130

## ABBREVIATIONS

ACS	acute coronary syndrome
AI	artificial intelligence
AUC	area under the curve
CAD	coronary artery disease
CI	confidence interval
CNR	contrast-to-noise ratio
CT	computed tomography
CTA	computed tomography angiography
CVD	cardiovascular diseases
D	dimension
DL	deep learning
FBP	filtered back projection
FFR	fractional flow reserve
GLCM	gray-level co-occurrence matrix
GLRLM	gray level run length matrix
GTSDM	gray-tone spatial dependencies matrix
HU	Hounsfield unit
HIR	hybrid iterative reconstruction
ICA	invasive coronary angiography
ICC	intra-class correlation coefficient
IQR	interquartile range
IVUS	intravascular ultrasound
LDL	low-density lipoproteins
MACE	major adverse cardiovascular events
MIR	model-based iterative reconstruction
ML	machine learning
NCP	non-calcified plaque
NRS	napkin-ring sign
OCT	optical coherence tomography
PET	positron emission tomography
RIA	radiomics image analysis

ROC	receiver operating characteristics
ROI	region of interest
SD	standard deviation
SIS	segment involvement score
SIS <sub>i</sub>	segment involvement score index
SNR	signal-to-noise ratio
SSS	segment stenosis score
SSS <sub>i</sub>	segment involvement score index
TCFA	thin-cap fibroatheroma

# 1. INTRODUCTION

Despite advancements in the diagnosis and therapy of cardiovascular diseases (CVD), it still remains the leading cause of morbidity and mortality worldwide (1, 2). Numerous anthropometric and lab-based risk models have been established to predict CVD (3-6). Multiethnic evaluation of these models showed systematic overestimation of CVD risk by up to 115%, indicating the need for more precise risk estimation (7, 8). Coronary artery disease (CAD), the leading pathology behind CVD is a progressive disease of the intimal layer of the coronaries, which can cause acute and/or chronic luminal obstruction (9).

Computed tomography (CT) based technologies have evolved considerably in recent years (10). Coronary CT angiography (CTA) has emerged as a useful and highly reliable imaging modality for the examination of the coronaries and is considered as a non-invasive alternative to invasive coronary angiography (ICA) (11). With its excellent sensitivity and negative predictive value, coronary CTA is a robust diagnostic test to rule out severe coronary stenosis and it is widely used as a “gate-keeper” for ICA (12-15). Even though, numerous studies have validated the diagnostic performance of CTA for the detection of obstructive coronary artery disease, as compared to ICA as reference standard, only a few studies have compared these two modalities regarding semi-quantitative plaque burden measurements (16, 17).

Modern CT scanners allow not only the visualization of the coronary lumen as ICA, but also the vessel wall granting non-invasive analysis of atherosclerosis itself (18). With around half of plaque ruptures occurring at lesion sites with smaller than 50% diameter stenosis, plaque morphology assessment seems equally as important as stenosis assessment (19-21). Four distinct plaque characteristics have been linked to major adverse cardiovascular events (MACE) using coronary CTA (18). Out of these four characteristics positive remodeling, low-attenuation and spotty calcification are quantitative high-risk plaque features. While the napkin-ring sign (NRS) is a qualitative marker, defined as a plaque cross-section with a central area of low CT attenuation apparently in contact with the lumen, which is surrounded by a ring-shaped higher attenuation plaque tissue (22). Due to its qualitative nature, identification of the NRS is affected by clinical experience and inter-reader variability (23). Therefore, more objective methods of compositional assessment are warranted.

Radiology images are multi-dimensional (D) datasets, where each voxel value represents a specific measurement based on some physical characteristic (24). Radiomics is the process of obtaining quantitative parameters from these spatial datasets, in order to create 'big data' datasets, where each lesion is characterized by hundreds of different parameters (25). These features aim to quantify morphological characteristics difficult or impossible to comprehend by visual assessment (26). Radiomics has proven to be a valuable tool in oncology (27). Several studies have shown radiomics to improve the diagnostic accuracy (28, 29), staging and grading of cancer (30), response assessment to treatment (31-33) and also to predict clinical outcomes (34, 35). However, application of radiomics in cardiovascular imaging is lacking.

The vast information present in radiological images not only allows to objectively identify pathologies as opposed to current irreproducible visual classification schemes, but also to expand the capabilities of an imaging technique. Implementing radiomics with machine learning (ML) and artificial intelligence (AI) may allow to increase the abilities of coronary CTA imaging to allow better identification of vulnerable plaques by localizing plaques with metabolic activity, or by identifying the exact histological category of a given lesion using simple CT images.

The current thesis aims to assess the potentials of advanced image analysis of atherosclerosis using coronary CTA images.

## **1.1. Imaging atherosclerosis using CTA in clinical practice**

Atherosclerosis is initiated by deposition of low-density lipoproteins (LDL) in the intima. With oxidation of the lipids, an inflammatory response is triggered, which is characterized by macrophages engulfing oxidized LDL particles, thus becoming foam cells (36). Poorly understood genetic and environmental factors propagate inflammation, resulting in further deposition of lipids, deterioration of the extracellular matrix and cell death (37). These processes lead to distinct plaque morphologies, which have been identified on histological samples (38).

After the first description of CTA in 1992 (39, 40), further technological advances, such as: more powerful X-ray tubes, faster gantry rotation times, multiple parallel detector rings and decreased slice thickness (41, 42) were introduced which allowed the visualization of the coronary arteries (43). With its excellent sensitivity and negative predictive value (12, 14), coronary CTA is a robust diagnostic test to rule out severe coronary stenosis and it is widely used as a “gate-keeper” for ICA (13, 15). Coronary CTA is currently the first imaging choice for stable chest pain patients in the United Kingdom and is a class 1 recommendation for initial testing of CAD based-on the European Society of Cardiology (44).

Nevertheless, modern CT scanners allow not only the visualization of the coronary lumen as ICA, but also the vessel wall, granting non-invasive analysis of atherosclerosis. This unique property of coronary CTA holds many advantages for patient risk stratification that other non-invasive tests do not. With submillimeter resolution coronary CTA allows non-invasive morphological assessment of coronary atherosclerosis.

Coronary CTA is interpreted based-on the guidelines of the Society of Cardiovascular Computed Tomography (45). Coronary plaques can be classified as being non-calcified, partially calcified or calcified based on the amount of calcium in the lesion. Furthermore, non-calcified plaque composition can be classified as homogeneous, heterogeneous and the showing the napkin-ring sign, which as one of the four high-risk plaque features that have been linked to MACE. Also the degree of stenosis caused by the plaque can be graded as minimal (<25% stenosis), mild (25% to 49% stenosis), moderate (50% to 69% stenosis), severe (70% to 99% stenosis) or occluded (46).

## 1.2. Assessment of plaque composition using coronary CTA

### 1.2.1. Degree of calcification

Coronary plaques can be classified as being non-calcified, partially calcified or calcified based on the amount of calcium in the lesion (*figure 1*).

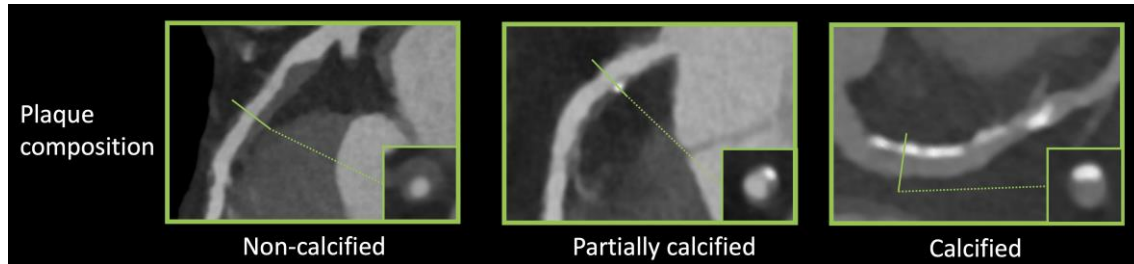


**Figure 1.** Representative images of plaque characteristics identifiable using coronary CTA (46).

Coronary plaques can be classified as non-calcified, partially calcified and calcified based on the degree of calcification present in the plaque. Curved multiplanar images are shown with a corresponding cross-section at the site of the solid line.

Large multicenter cohorts such as the COronary CT Angiography EvaluationN For Clinical Outcomes: An InteRnational Multicenter registry (CONFIRM) (47), investigated the prognostic value of plaque composition on all-cause mortality. Based on 17,793 suspected CAD patients' 2-year survival data, the number of segments with partially calcified or calcified plaque had a significant effect on mortality (hazard ratios: non-calcified: 1.00,  $p = 0.90$ ; partially calcified: 1.06,  $p \leq 0.0001$ ; calcified: 1.08,  $p \leq 0.0001$ ). After adjusting for clinical factors, none of the plaque components improved the diagnostic accuracy of the model (non-calcified:  $p = 0.99$ ; partially calcified:  $p = 0.60$ ; calcified:  $p = 0.10$ ) (48). Hadamitzky et al. found similar results when investigating the prognostic effect of plaque composition on 5-year mortality rate based on suspected CAD patients. After adjusting of clinical risk based on the Morise score (49), only the number of segments with calcified plaques improved significantly the diagnostic accuracy of the model (non-calcified:  $p = 0.083$ ; partially calcified:  $p = 0.053$ , calcified:  $p = 0.041$ ) (50). Dedic et al. found similar results in a different patient population. When investigating the effects of different plaque components of non-culprit lesions on future MACE in acute coronary syndrome (ACS) patients, they found none of the plaque types to have a significant impact on future MACE rates (hazard ratios: non-calcified: 1.09,  $p = 0.11$ ;

partially calcified: 1.11,  $p = 0.35$ ; calcified: 1.11,  $p = 0.15$ ) (51). Interestingly Nance et al. found very different results when analyzing 458 patients' data, who presented to the emergency room with acute chest pain but based on ECG and serum creatinine had inconclusive results and thus underwent coronary CTA. All patients had low to intermediate risk for CAD. After a follow-up of 13 months, they split the patients into three groups: only non-calcified plaques; exclusively calcified plaques; any partially calcified plaque or both non-calcified and calcified plaques. After adjustment for clinical characteristics and calcium-score they found the following hazard ratios: 57.64 for non-calcified, 55.76 for partially calcified and 26.45 for patients with solely calcified plaques (52). The difference compared to other studies might be due to the different methodological approach used. While previously mentioned papers examined the effect of plaque composition on a segment based level incrementally, giving the hazard ratio of an increase in the number of segments with a given plaque type, Nance et al. reported the results on a patient based level dichotomized, giving the hazard ratio of having a specific type of plaque as compared to patients without any plaques.

Overall, the effect of plaque composition on mortality still remains controversial. It seems simply classifying plaques based on the amount of calcium present holds little information regarding clinical outcome. These findings suggest, that identification of more complex morphologies is needed for better prediction of adverse outcomes.

### **1.2.2. Plaque attenuation pattern**

Histopathologic examinations demonstrated that thin-cap fibroatheromas (TCFA) exhibit similar plaque morphologies as ruptured plaques (38, 53). TCFAs are composed of a lipid-rich necrotic core surrounded by a thin fibrotic cap. Coronary CTA is capable of distinguishing between lipid-rich and fibrotic tissue based on different CT attenuation values, however the reliable classification of non-calcified plaques into these two categories remains challenging.

A more qualitative approach is not to look at the absolute HU values, but rather to classify non-calcified plaques as homogeneous or heterogeneous in attenuation patterns (*figure 2*). Heterogeneous plaques are characterized by at least two regions with different attenuations values, while homogeneous plaques do not have regions visually differentiable. Based on cross sectional images, heterogeneous plaques can be divided

into ones with NRS and ones without (22). NRS plaques are characterized by a low attenuation central area, which is apparently in touch with the lumen, encompassed by a higher attenuation ring-like peripheral area (18).

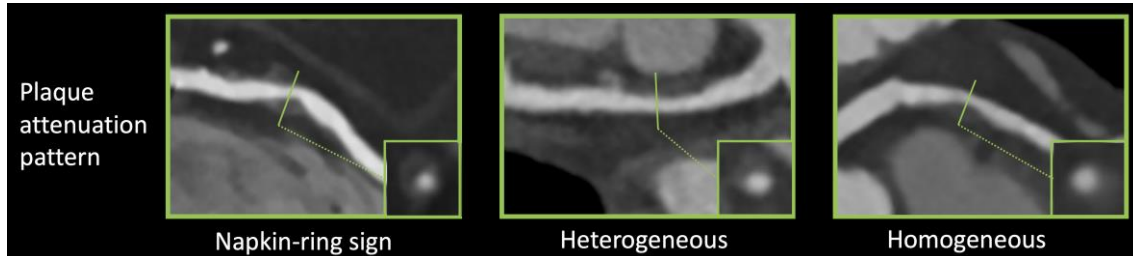


**Figure 2.** Representative images of plaque attenuation patterns (46).

Non-calcified plaque regions may be classified as homogeneous, heterogeneous and the napkin-ring sign, which is one of the four high-risk plaque features. Curved multiplanar images are shown with a corresponding cross-section at the site of the solid line.

The napkin-ring sign has been identified as a specific imaging biomarker of vulnerable plaques. So called high-risk plaque features aim to identify plaque prone to rupture. Overall, four high risk plaque features have been identified to date: the napkin-ring sign, low attenuation, spotty calcification and positive remodeling.

### 1.3. Assessment of high-risk plaque features using coronary CTA

High-risk plaque features have been identified in the literature to indicate morphologies which might be prone of plaque rupture (*figure 2-3*). These are the NRS, low attenuation, spotty calcification and positive remodeling.

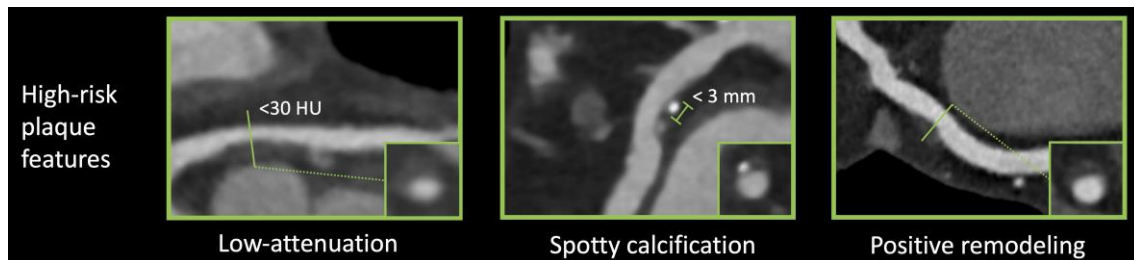


**Figure 3.** Representative images of high-risk plaque features (46).

Next to the napkin-ring sign plaque (*figure 2*), three further plaque imaging markers have been linked to major adverse cardiac events. Curved multiplanar images are shown with a corresponding cross-section at the site of the solid line.

HU: Hounsfield unit

#### 1.3.1. Napkin-ring sign

Maurovich-Horvat et al. showed based on ex-vivo examinations that NRS plaques have excellent specificity and low sensitivity (98.9%; 24.4%, respectively) to identify plaques with a large necrotic core, which is a key feature of rupture prone TCFA's (54). Histological evaluation of NRS plaques showed that NRS plaques had greater area of lipid-rich necrotic core (median 1.1 vs. 0.5 mm<sup>2</sup>, p = 0.05), larger non-core plaque area (median 10.2 vs. 6.4 mm<sup>2</sup>, p < 0.01) and larger vessel area (median 17.1 vs. 13.0 mm<sup>2</sup>, p < 0.01) as compared to non-NRS plaques (55). Interestingly, these results are in line with Virmani et al. who investigated the morphology of ruptured plaques (38). Furthermore, results of the Rule Out Myocardial Infarction/Ischemia Using Computer-Assisted Tomography – II trial strengthen the concept of NRS plaques being precursors of ruptured plaques. Based on the results of 472 patients suspected of ACS they found NRS plaques to be an independent predictor of ACS (odds ratio: 8.9; 95% confidence interval (CI): 1.8 - 43.3; p = 0.006) independent of stenosis severity (23). Kashiwagi et al. found similar results, when analyzing the results of ACS patients and stable angina patients. They found NRS plaques to be more frequent at culprit and also at non-culprit sites in ACS patients

as compared to stable angina patients (culprit: 49.0% vs. 11.2%,  $p < 0.01$ , respectively; non-culprit: 12.7% vs. 2.8%,  $p < 0.01$ , respectively) (56). Otsuka et al. conducted the first prospective clinical trial to assess the predictive values of NRS plaques for future ACS events (57). They showed that NRS plaques were significant independent predictors of later ACS events (hazard ratio: 5.55, CI: 2.10–14.70,  $p < 0.001$ ). Similarly, Feuchtner et al. showed NRS to have the highest hazard ratio (7.0, CI: 2.0 - 13.6) over other high risk features when investigating 1469 patients with a mean follow-up of 7.8 years (58). Overall it seems the napkin-ring sign has additive information beyond simple plaque composition information. However, with many factors effecting assessment of attenuation patterns, we only have limited censored information regarding the prognostic effect of these entities.

### **1.3.2. Low attenuation**

Several studies have investigated the use of region of interest (ROI) to define the plaque components using coronary CTA as compared to intravascular ultrasound (IVUS) as the gold standard of *in vivo* plaque characterization (59-62). These validation studies were able to find significant differences in mean Hounsfield unit (HU) values for the different plaque components, however there is a considerable overlap between these categories ( $121 \pm 34$  HU vs.  $58 \pm 43$  HU,  $p < 0.001$ ) (60). Several studies were inspired by these results and found lower mean and minimal attenuation values of plaques in ACS patients as compared to plaques of stable angina patients (63-65). However, there was still a significant overlap in attenuation values between the two groups. Nevertheless, Motoyama et al. showed that with the use of a strict cut-off value ( $<30$  HU), ACS patients have significantly more low attenuation plaques as compared to stable angina patients (79% vs. 9%,  $p < 0.001$ ), suggesting low attenuation to be a useful marker for identifying vulnerable patients (66). Marwan et al. proposed a more quantifiable approach using quantitative histogram analysis. For all cross-sections for each plaque, a histogram was created from the CT attenuation numbers, and the percentage of pixels with a density  $\leq 30$  HU was calculated. They found similarly overlapping HU values for lipid-rich versus fibrous plaques. However, using a cut-off value of 5.5% for pixels with  $\leq 30$  HU, they were able to differentiate between predominantly lipid-rich plaques versus predominantly fibrous plaques (sensitivity: 95%; specificity: 80%; area under the curve: 0.9) using IVUS

as reference standard (67). Despite these encouraging results, there is still a major concern because of the overlapping HU values of different plaque components. Furthermore, several studies have shown slice thickness (68), imaging protocols (69), tube voltage settings (70), intra coronary contrast attenuation values (71), reconstruction algorithms, filters and noise (68, 72) all to influence CT attenuation values.

Overall, it seems discrimination of non-calcified plaques based on HU value thresholds into lipid-rich and fibrous categories has additional prognostic value, but the different modifying effects of image acquisition and reconstruction limit the robust use of attenuation values for patient risk prediction.

### **1.3.3. Spotty calcification**

Histological examinations identified calcified nodules in patients with coronary thrombosis (73). Several histological studies have shown the frequency of such findings to be around 2-7% in sudden death cases (74-76). Intra-plaque micro calcifications are thought to destabilize plaques and promote plaque rupture (77, 78). Unfortunately, spatial resolution of current CT scanners is under the threshold needed for identifying microcalcification. Nevertheless, coronary CTA has excellent sensitivity to identify calcium, thus spotty calcification defined as a <3 mm calcified plaque component with a >130 HU density surrounded by non-calcified plaque tissue has been proposed as a CTA (*figure 3*) marker of histological microcalcifications (66, 79). Van Velzen et al. suggested to further classify such lesions as small (<1 mm), intermediate (1–3 mm), and large (>3 mm) (80). They found small spotty calcifications to be more frequently present with TCFA's identified by IVUS as compared to large spotty calcifications (31% vs 9%;  $p < 0.05$ ). These results support the hypothesis, that small calcified nodules are indicators of high-risk plaques, and that CTA is at the limits of identifying real calcified nodules, which have been identified using histological studies. Even so, several studies have shown culprit lesions of ACS patients to have spotty calcifications as compared to stable angina patients or non-culprit lesions (81, 63, 66, 64). However, there are only few prospective studies evaluating the prognostic effect of spotty calcifications, thus the relationship between intra-plaque calcification and MACE remains uncertain (82).

A promising technique for the identification of micro calcifications beyond the resolution limits of CTA is positron emission tomography (PET) imaging (83). Dweck et al. used

NaF<sup>18</sup> to mark microcalcifications not visible on CTA. NaF<sup>18</sup> has been used previously for decades to image new bone formation, primarily in cancer metastases, and recently has been used to image active calcification in coronary plaques. In their study based on 119 volunteers, they showed higher uptake values in patients with prior cardiovascular events, angina and higher Framingham risk scores, as compared to control subjects ( $p = 0.016$ ;  $p = 0.023$ ;  $p = 0.011$ , respectively).

Altogether, it seems spotty calcifications have additional additive values for identifying vulnerable plaques. However current resolution of CT scanners prohibits the imaging of microcalcifications that are seen as one of the common features of ruptured plaques. Nevertheless, spotty calcification detectable using CTA seems to correlate well with adverse cardiac events, and NaF<sup>18</sup>-PET is also a promising new technique to visualize micro calcifications. However prospective studies are needed to evaluate the predictive value of these markers.

#### **1.3.4. Positive remodeling**

Atherosclerotic plaques initially tend to grow outwards leaving luminal integrity unchanged (84). Thus, while many coronary plaques accumulate lipids and become TCFAs, they might not cause any clinical symptoms. This phenomenon is referred to as positive remodeling (*figure 3*). Varnava et al. examined 88 sudden cardiac death cases and showed that plaques with positive remodeling have larger lipid cores and more macrophages, both which are considered vulnerability markers (85). Using coronary CTA, the remodeling index is calculated as the vessel cross-sectional area at the level of the maximal stenosis divided by the average of the proximal and distal reference sites' cross-sectional areas (86). Coronary CTA has a tendency to overestimate remodeling index, thus Gauss et al. proposed a cut-off value of  $\geq 1.1$ , meaning a 10 % increase in the vessel cross sectional area at the site of the maximal stenosis compared to the average of the reference cross sectional areas (87). This resulted in an increased sensitivity and a moderate drop in specificity as compared to a lower cut-off value of  $\geq 1.05$  (sensitivity: 78% vs. 45%; specificity: 78% vs. 100%) using IVUS as reference standard. Motoyama et al. showed positively remodeled plaques to be more frequent in ACS patients as compared to stable angina patients (87% vs. 12%,  $p < 0.0001$ , respectively) (66). Positive remodeling had the best sensitivity and specificity (87%; 88%,

respectively) as compared to low-attenuation and spotty calcification to identify ACS patients (88).

Overall it seems that positive remodeling is an important plaque feature for the identification of vulnerable plaques. Being less conditional to image noise as plaque attenuation, and having a more quantitative definition as the NRS, positive remodeling might become a more robust marker for vulnerable plaques. However, more prospective studies are needed to assess the effect of positive remodeling on later outcomes.

#### 1.4. Assessment of stenosis degree using coronary CTA

Based on guidelines published by the Society of Cardiovascular Computed Tomography (SCCT), luminal diameter stenosis can be graded as: minimal (<25% stenosis), mild (25% to 49% stenosis), moderate (50% to 69% stenosis), severe (70% to 99% stenosis) or occluded (*figure 4*). . In case of left main stenosis, diameter stenoses above 50% are also considered severe.

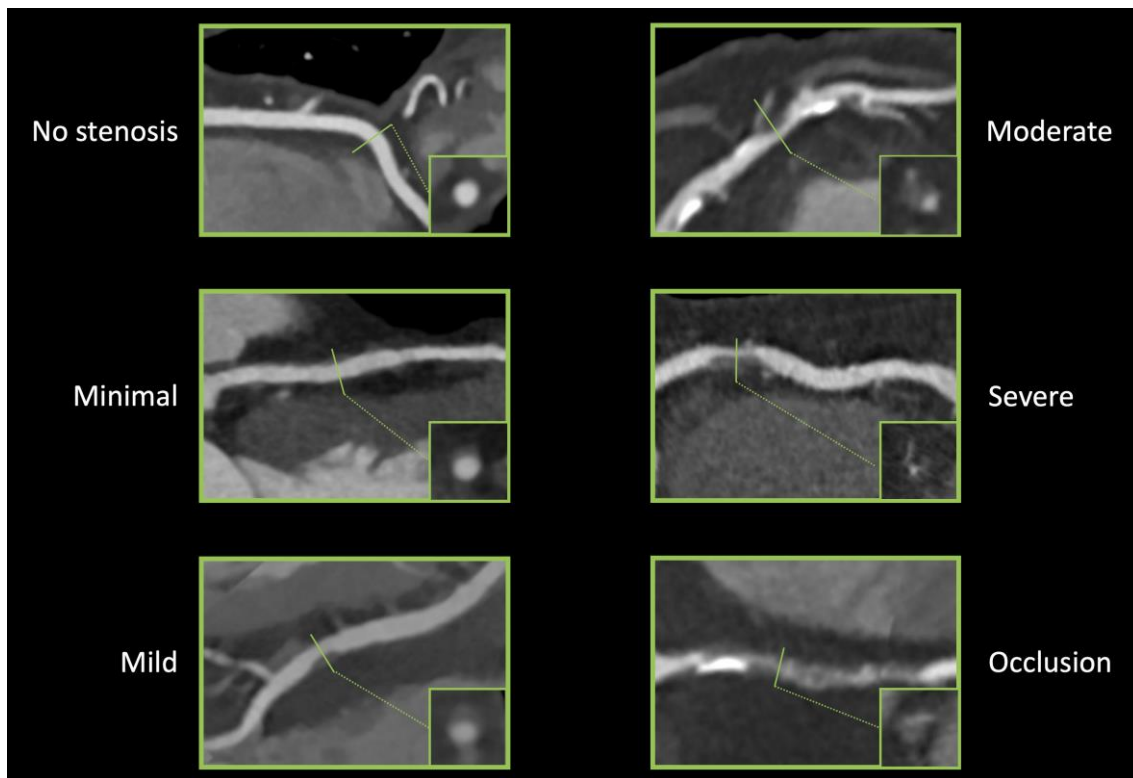


**Figure 4.** Representative images of grades of stenoses caused by coronary plaques on coronary CTA (46).

Coronary stenosis can be graded as minimal (<25% stenosis), mild (25% to 49% stenosis), moderate (50% to 69% stenosis), severe (70% to 99% stenosis) or occluded. In case of left main stenosis, diameter stenoses above 50% are also considered severe. Curved multiplanar images are shown with a corresponding cross-section at the site of the solid line

As coronary plaques grow, blood flow is eventually disrupted causing ischemia distal to the lesion. Originally coronary CTA was considered as a non-invasive alternative to ICA; thus many studies have looked into the predictive value of luminal stenosis seen on CTA. All studies focus on obstructive lesions, since most patients referred to coronary CTA have minimal and mild plaques, thus the predictive value of such stenosis is poor. Two

cut-off values:  $\geq 50\%$  and  $\geq 70\%$  diameter stenosis is frequently used to determine obstructive lesions. Min et al. investigated the prognostic effect of obstructive lesion on a patient-based level and found both  $\geq 50\%$  and  $\geq 70\%$  lesions to be significant predictors of later outcomes (hazard ratio: 2.89; 4.31, respectively) (89). Several other studies have also found obstructive lesions to be significant predictors of later outcome, but considerably different hazard ratios have been reported (90-92, 50, 93, 94). Interestingly, there is a discrepancy in the results when correcting the models for clinical risk factors. The significant hazard ratios reported by Min et al. became non-significant when including cardiac risk factors in the model, but when looking at a segment-based level not a patient based level, the presence of obstructive stenosis remained significant, but with a smaller hazard ratio (1.05; CI: 1.02–1.09) (89). However, Nakazato et al. and Andreini et al. did not find similar tendencies when correcting for clinical factors, as obstructive CAD remained a significant predictor (90, 93). Increasing further the discrepancy in the results, a 5-year follow-up study published by Hadamitzky et al. reported that while non-obstructive CAD was a significant predictor of hard endpoints (Hazard ratio: 3.33; CI: 1.40-7.91), one and two vessel obstructive disease was not (Hazard ratio: 1.46; CI:0.50-2.43; 3.85; CI: 0.96-15.04) (50).

One explanation for the disparity in the results might be that luminal stenosis on CTA is a poor indicator of hemodynamically significant lesions (95), which has been shown to be a good predictor of adverse events (96-98). Using computational fluid dynamics it is possible to simulate blood flow in the coronaries and estimate the hemodynamic characteristics of a lesion with good diagnostic accuracy (99, 100). The Prospective Longitudinal Trial of FFR<sub>CT</sub>: Outcome and Resource Impacts (PLATFORM) further demonstrated, that the use of CT derived fractional flow reserve (FFR<sub>CT</sub>) values significantly lowered the rate of ICA and used less resources at lower costs (101-103). However, current FFR<sub>CT</sub> simulations are expensive and time consuming, as the simulations are performed off-site. Recently on-site FFR<sub>CT</sub> techniques have been introduced, which are able to calculate FFR<sub>CT</sub> in couple of seconds to minutes (104-108). Overall, it seems the effect of significant stenosis on patient outcomes is controversial, which is mainly caused by the poor correlation between stenosis seen on CTA and hemodynamic information.

## **1.5. Radiomics: the potential to objectively analyze radiological images**

Medical imaging has developed exponentially in the past decades (109). While new techniques are frequently introduced for each imaging modality, our interpretation of medical images is still based mainly on qualitative image characteristics in the daily clinical routine. State-of-the-art scanners can achieve submillimeter spatial and millisecond temporal resolution, significantly increasing the amount of information gained from radiological examinations. Qualitative evaluation of medical images discards vast amounts of information, which may hold new perspectives for the identification and classification of diseases (110). For most cases, this kind of image interpretation might be sufficient for clinical judgement, but in the era of precision medicine, when we seek to refine our taxonomy of diseases, and cure illnesses based on subtle differences in the genome (111), a lot more is expected from radiology– the medical profession of imaging pathologies.

Radiological images are in fact extensive 2 or 3D datasets, where the values present in the pixels (or volumetric pixels called voxels) are used to create the picture. Each and every voxel is a measurement itself, based on some physical characteristics of the underlying anatomical structure, such as the degree of electromagnetic radiation absorption which is used by CT. These values can be assessed by visual inspection, which is done in daily clinical routine, or they can be analyzed using advanced image analysis. *Radiomics* is the process of extracting several different features from a given ROI to create large datasets where each abnormality is characterized by hundreds of parameters (24). Some of these parameters are commonly known and used by radiologist, such as the mean attenuation value or the longest diameter of a lesion, while others that quantify the heterogeneity or shape of an abnormality are less apparent. From these values novel analytical methods are used to identify connections between the parameters and the clinical or outcome data. *Datamining* is the process of finding new meaningful patterns and relationships between numerous variables. From these results, novel imaging biomarkers can be identified which could increase the diagnostic accuracy of radiological examinations and expand our knowledge of the underlying pathological processes (*figure 5*).

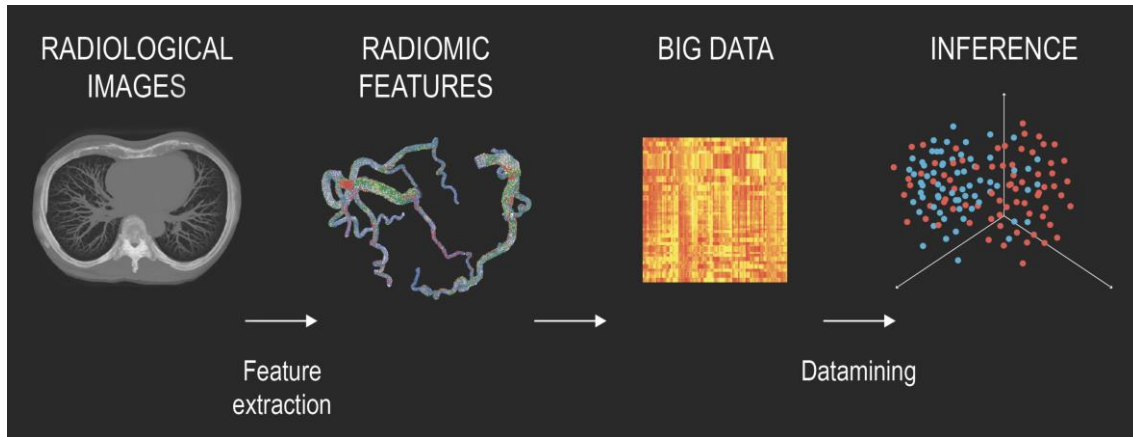


**Figure 5.** Pipeline of radiomics-based patient analysis (24).

After image acquisition, new novel radiomics-based image characteristics are extracted to quantify different lesion properties. The hundreds of variables are joined together to create ‘big data’ databases. Datamining is used to find new meaningful connections between the parameters and the clinical outcome data. Based on the results, new imaging biomarkers can be identified which have the potential to increase the diagnostic accuracy of radiological examinations.

Coronary lesions are complex pathologies made up of several different histological components. These different tissues all absorb radiation to a different extent; thus, they are depicted as having different attenuation values on CT. Basically, each voxel is a separate measurement of how much radiation is absorbed in a given volume, thus CT can be used to evaluate the underlying anatomical structure *in vivo*. Therefore, it is rational to assume that distinct morphologies of different coronary lesions appear differently on CT. As a result, numerous qualitative imaging markers have been identified on coronary CTA angiography (18, 22). These characteristics have been shown to be indicators of future MACE (58, 57), but they are prone to inter- and intra-observer variations due to their qualitative nature (112). Therefore, it would be desirable to have quantitative image parameters instead of qualitative markers to express different lesion characteristics. Radiomics is the specialty of mathematically describing different lesion characteristics such as heterogeneity, shape, etc.

Radiomic techniques can be grouped into 4 major categories: 1) Intensity-based metrics, 2) Texture-based analysis, 3) Shape-based measures and 4) Transform-based metrics.

### 1.5.1. Intensity-based metrics

Intensity-based metrics are often referred to as first-order statistics, which means that statistics are calculated from the values themselves, not considering any additional information which might be gained from analyzing the relationship of the voxels to each other. These statistics can be calculated by selecting a ROI and extracting the voxel values from it. The values then can be analyzed with the tools of histogram analysis. These statistics can be grouped into three major categories, which quantify different aspects of the distribution: 1) average and spread, 2) shape and 3) diversity.

Most of these statistics are well-known to medical professionals and in some cases are used for describing the characteristics of a coronary lesion. *Mean*: the value that resembles our values the best, since its distance from all other values is minimal. *Median*: the value that divides the distribution into two equal halves. *Minimum* and *maximum*: which are the two extremes of the values. *Percentiles*: which divide the distribution into a given percent of the data. *Interquartile range*: which are two specific values which enclose the middle 50% of the data points. These statistics all have to do with average and the spread of the data, they do not convey any information regarding the shape or the diversity of the values themselves. Several different distributions may exist that have the same mean and spread but have very different shapes. Therefore, these statistics are not enough to describe the properties of coronary lesions, since distinct plaque morphologies can have very similar values (*figure 6*).

The shape of a distribution is commonly described by moments. Moments are a family of mathematical formulas that capture different aspects of the distribution. They are defined as the average of the values ( $x_i$ ) minus a given value ( $c$ ) raised to a given power ( $q$ ). If  $c$ =the mean ( $\mu$ ) and  $q=2$ , then we get the *variance*, which tells us how spread-out our data is from the mean. If we take the square root of the variance, we receive the *standard deviation (SD)*. In cases of normally distributed data, the SD informs us where approximately 68% of the data is located around the mean. If  $c=\mu$  and  $q=3$  and we divided our moment by  $SD^3$ , then we get *skewness*, which quantifies how asymmetric our distribution is around the mean. Negative skew indicates that a large portion of the data is to the right of the mean, while positive skew means just the opposite. If  $c=\mu$  and  $q=4$  and we normalize by  $SD^4$  we receive *kurtosis*, which enumerates how close our data points are to the mean. Small values indicate that there are few outliers in the data, and

most values are in one SD distance of the mean, while higher values indicate that a larger proportion of values situated further away from the mean the one SD. In cases of normally distributed data the kurtosis is 3, therefore it is reasonable to compare our kurtosis values to this value to analyze how our values differ as compared to the normal distribution.

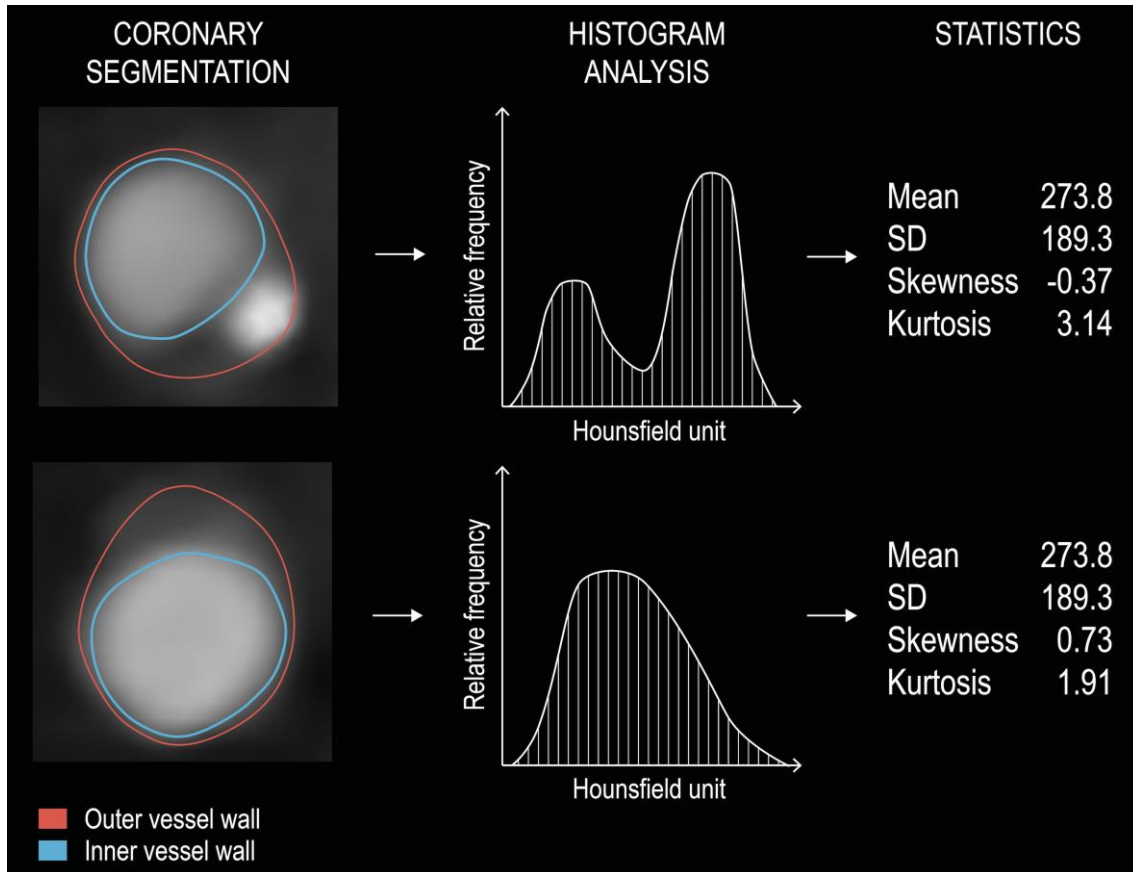


**Figure 6.** Pipeline for calculating first-order statistics on two representative examples of coronary lesions (24).

First the coronary arteries need to be segmented. Then histograms need to be created showing the relative frequency of given Hounsfield-unit values. From these different statistics can be calculated. The image also justifies the use of several different parameters to reflect a lesion, since the average attenuation values and the standard deviations are the same, while only higher moments can differentiate between these two plaques.

SD: standard deviation

Previous statistics gave information regarding the average, the spread and the shape of our distribution, but these give no information regarding the dissimilarity of the voxel values. Concepts from information theory can be used to quantify the heterogeneity of our values. *Energy* quantifies the overall magnitude of the intensities and is calculated by squaring the values and then summing them. *Uniformity* measures the similarity of the

values and is calculated by squaring the relative frequency of the given attenuation values and then summing them. If we only have one type of value then its relative frequency is 1, and therefore uniformity is 1, while if we have several different values, then their probabilities are all smaller than 1 and thus their squared sum will also be smaller than 1. *Entropy* is a concept proposed by Shannon in 1948, which measures the information content of our data (113). Events with higher probabilities ( $p$ ) carry less information since we could have guessed the outcome, while unlikely events carry more information since their occurrence is infrequent thus highlight specific instances. Entropy quantifies uncertainty by weighing the information content of an event with its probability. The entropy of a system is equal to adding up these values and multiplying it by minus 1. The higher the value the more heterogeneous is our data. The amount of entropy is commonly measured in *bits*.

### **1.5.2. Texture-based metrics**

Previously mentioned parameters discarded all spatial information and only use the absolute values of the voxels themselves, even though we know that the spatial relation of different plaque components has a major effect on plaque vulnerability (38). Plaque composition is expressed by the spatial relationship of the voxels on CTA. This relationship is hard to conceptualize using mathematical formulas. A solution emerged in the 70s, when scientists were presented with the problem of identifying different terrain types from satellite imagery. The field of *texture analysis* has been evolving ever since. Texture is the broad concept of describing patterns on images. Patterns are systematic repetitions of some physical characteristic, such as intensity, shape or color. Texture analysis tries to quantify these concepts with the use of mathematical formulas, which are based on the spatial relationship of the voxels.

In 1973 Haralick et al. proposed the idea of *gray-tone spatial dependencies matrix (GTSDM)* commonly known as *gray-level co-occurrence matrix (GLCM)* for the texture analysis of 2D images. GLCMs are second-order statistics, which means that statistics are calculated from the relationship of 2 pixels' values, not the values themselves. The goal of these matrices is to quantify how many times similar value voxels are located next to each other in a given direction and distance, and to derive statistics from this information.

First the coronary arteries need to be segmented to determine the inner and the outer vessel wall boundaries to locate the coronary lesions. Then the HU values of the voxels need to be discretized into a given number of groups, since exactly the same value voxels occur only very rarely in an image. Our GLCM will have exactly the same number of columns as rows, which equals the number of HU groups we discretized our image to. Next a direction and a distance need to be determined to examine texture. Direction is usually given by an angle. By convention voxels to the east of a reference voxel are at  $0^\circ$ , ones to the north-east are at  $45^\circ$ , ones to the north are at  $90^\circ$  and ones to the north-west are at  $135^\circ$ . One only needs to calculate the statistics in these four directions, since the remaining four directions are exact counterparts of these. For example, if our angle equals  $0^\circ$  and the distance equals 1, then the raw GLCM is created by calculating the number of times a value  $j$  occurs to the right of value  $i$ . This number is then put into the  $i^{\text{th}}$  row and  $j^{\text{th}}$  column of the raw GLCM. If we were to calculate the GLCM in the opposite direction (at  $180^\circ$ ), then we would get very similar results, just that the rows and the columns would be interchanged as compared to the original GLCM (at  $0^\circ$ ), since asking how many times do we find a voxel value  $j$  to the right of voxel value  $i$  is the same thing as asking how many times will we find a voxel value  $i$  to the left of voxel value  $j$ . Therefore, for convenience we add the transpose matrix (rows and columns interchanged) to our original raw GLCM matrix to receive a symmetrical GLCM matrix (a value in the  $i^{\text{th}}$  row and  $j^{\text{th}}$  column equals the value in  $j^{\text{th}}$  row and  $i^{\text{th}}$  column). Since the absolute numbers are not too informative, we normalize the matrix by dividing all the values in the matrix by the sum of all values in the GLCM to receive relative frequencies instead of absolute numbers. Pipeline for calculating GLCMs can be found in *figure 7*.

These matrices contain lot of information on their own. The values on the main diagonal represent the probabilities of finding same value voxels. The further away we move from the main diagonal the bigger the difference between the intensity values. One extreme would be to have only elements on the main diagonal, which would mean that only similar value voxels are present in that given direction and distance. Another extreme would be when all elements of the GLCM would have the same value. In this case the intensity values occur at random in our image.

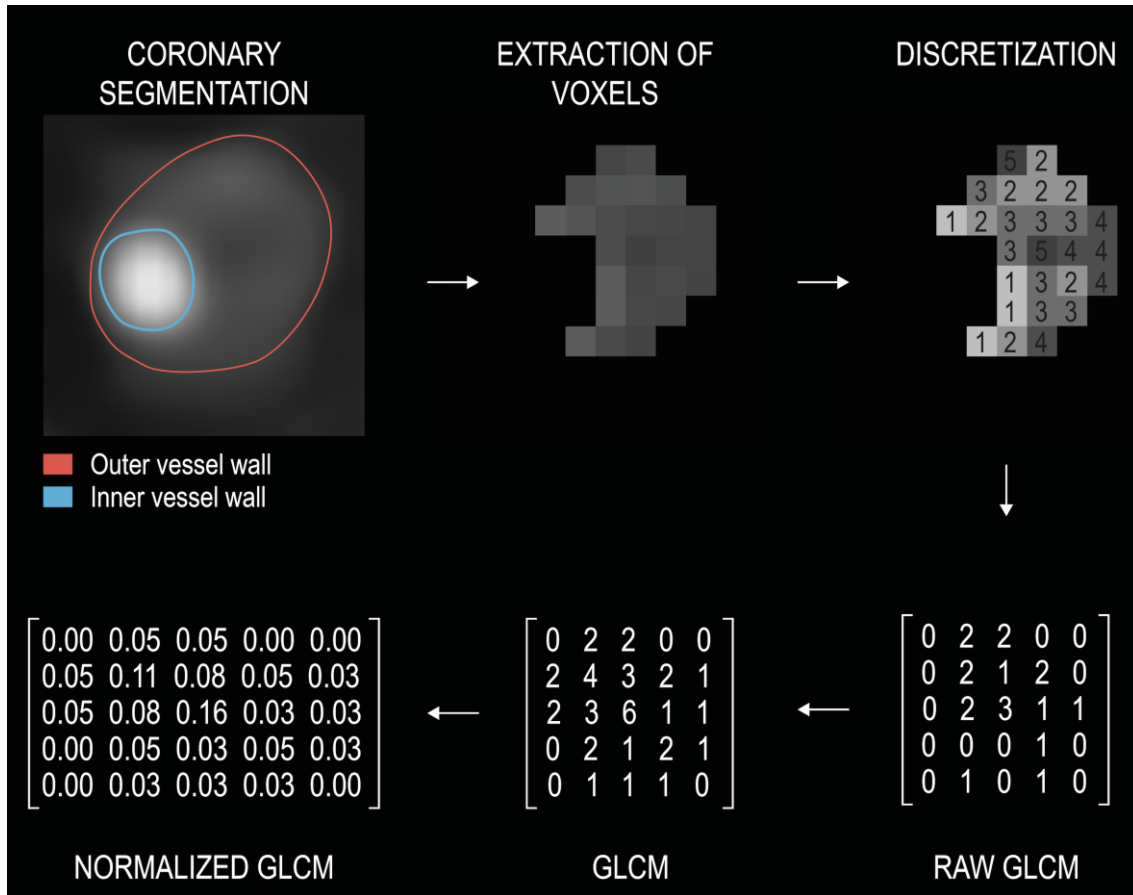


**Figure 7.** Pipeline for calculating gray-level co-occurrence matrices (24).

First the coronary arteries need to be segmented. Then the voxels need to be extracted from the images. Next the images need to be discretized into  $n$  different value groups. Then a given direction and distance is determined to calculate the GLCM (distance 1, angle  $0^\circ$ ). Raw GLCMs are created by calculating the number of times a value  $j$  occurs to the right of value  $i$ . This value is then inserted into the  $i^{\text{th}}$  row and  $j^{\text{th}}$  column of the raw GLCM. To achieve symmetry, the transpose is added to the raw GLCM. Next, the matrix is normalized by substituting each value by its frequency, this results in the normalized GLCM. Afterward, different statistics can be calculated from the GLCMs. To get rotationally invariant results, statistics are calculated in all four directions and then averaged.

GLCM: gray level co-occurrence matrix

Haralick et al. proposed 14 different statistics that can be determined from the GLCMs, but many more exist. All derived metric weight the entries of the matrix by some value depending on what property one wants to emphasize. *Angular second moment/uniformity/energy* squares the elements of the GLCM and then sums them up. The fewer the number of different values present in the matrix the higher the value of uniformity. *Contrast* is calculated by multiplying each value of the GLCM by the difference in the attenuation values squared for that given row and column  $(i - j)^2$ , and

then adding up all the numbers. We receive bigger weights where there is a large difference between the intensity values of the neighboring voxels, and we receive a weight of 0 for elements on the main diagonal, for cases where the two voxel intensities are equal. Therefore, contrast quantifies the degree of different HU value voxels present in a given direction and distance. *Homogeneity/inverse difference moment* uses the reciprocal value of the previous weights. This way elements closer to the main diagonal receive higher weights, while values farther away receive smaller values. Since the denominator cannot be 0, thus we add 1 to all weights. Since texture is an intrinsic property of the picture, we should not get different results if we simply rotate our image by 90°. Therefore, to achieve rotationally invariant results, statistics are calculated on the four GLCMs and then averaged.

While second-order statistics looked at the relationship of two voxels, *higher-order statistics* assess the relationship of three or more voxels. The easiest concept proposed by Galloway is the *gray level run length matrix (GLRLM)*, which assess how many voxels are next to each other with the same value (114). The rows of the matrix represent the attenuation values, the columns the run lengths. Pipeline for calculating GLRLMs can be found in *figure 8*.

Galloway proposed 5 different statistics to emphasize different properties of these matrices. *Short runs emphasis* divides all values by their squared run length and adds them up. Therefore, the number of short run lengths will be divided by a small value, while the number of long run lengths will be divided by a large value, thus short run lengths will be emphasized. *Long runs emphasis* does just the opposite by instead of dividing the values, it multiplies the entries with the squared run length and then adds them up. *Gray level nonuniformity* squares the number of run lengths for each discretized HU group and then sums them up. If the run lengths are equally probable in all cases of intensities, then it takes up its minimum. These statistics can also be calculated in all four directions to receive rotationally invariant results we average them.

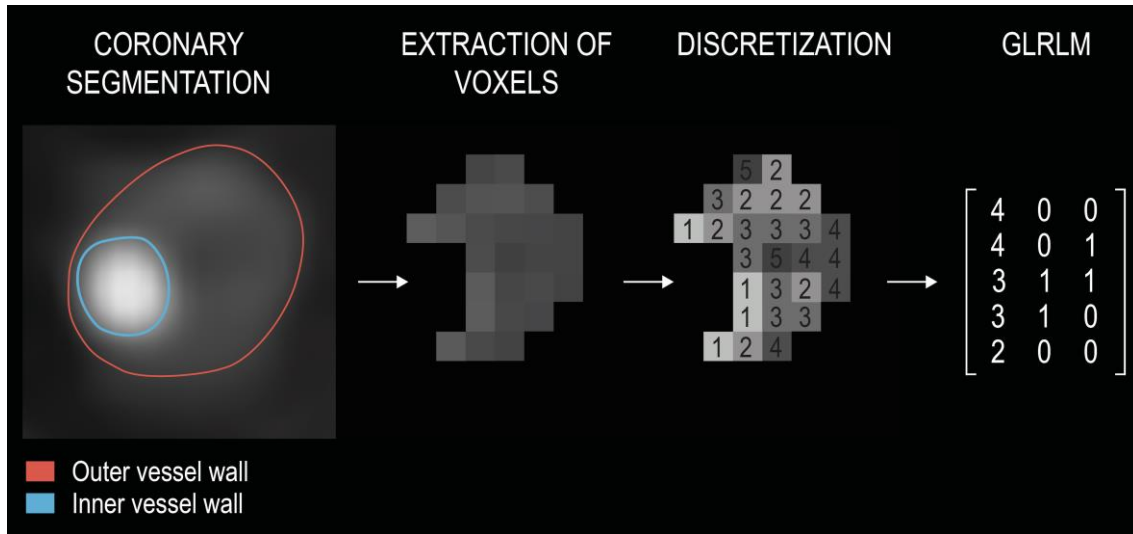


**Figure 8.** Pipeline for calculating gray level run length matrices (24).

First the coronary arteries need to be segmented. Next the voxels need to be extracted from the images. Then the images need to be discretized into  $n$  different value groups. Next a given direction (angle  $0^\circ$ ) is determined. GLRLMs are created by calculating the number of times a  $i$  value voxels occur next to each other in the given direction. The  $i^{\text{th}}$  row and  $j^{\text{th}}$  column of the GLRLM represents how many times it occurs in the image, that  $i$  value voxels are next to each other  $j$  times. To get rotationally invariant results, the statistics calculated in different directions are averaged.

GLRLM: gray level run length matrix

GLCMs and GLRLMs have inspired many to create their own matrices based on some other rule. These are, but not limited to: gray level gap length matrix (115), gray level size zone matrix (116), neighborhood gray-tone difference matrix (117) or the multiple gray level size zone matrix (118).

Laws suggested a different method to emphasize different features of an image (119). This is done through convolution, which is the multiplication of our voxel values by its neighbors weighted values which results in a new image. Depending on the weights, we can filter out different properties, while emphasizing others. The weights are stored in the kernel matrix. Laws proposed 5 different 1D kernels which emphasize some characteristic, such as ripples or edges. These 1D kernels can be used to create 2 and 3D kernels which can alter radiological images. We can calculate any statistics, for example energy, on these new images to summarize them.

### 1.5.3. Shape-based metrics

Atherosclerotic plaques are complex 3D structures situated along the coronary arteries. The spatial distribution and localization of different plaque components can also have an effect on plaque vulnerability.

*1D metrics* are based on measuring the distance between 2 points. These parameters are commonly used in clinical practice to describe the magnitude of an abnormality. On coronary CTA the *diameter stenosis* is used to assess the severity of a lesion, or the *length* to quantify the extent of a plaque. Diameters measured in different directions can be used to derive new statistics that can resemble some new property, for example the ratio of the longest and the shortest diameter resembles the roundness of a lesion.

*2D metrics* are calculated on cross-sectional planes and are used to calculate different parameters that are based on *areas*. These parameters are most often used to approximate some 3D property of the abnormality. The 1D metric diameter and the 2D metric area are all considered approximations of the 3D metric *volume*. For example, cross-sectional plaque burden is used to approximate full vessel volume-based plaque burden in coronary CTA.

3D metrics try to enumerate different aspects of shape. The geometrical properties of shapes have been thoroughly examined in the field of rigid body mechanics. All objects have so-called *principle axes* or *eigenvectors*. These mutually perpendicular axes cross each other at the center of mass. Force applied to these axes act independently, meaning that if we push or rotate the object along on of these principle axes, our object will not move or rotate in any other direction. These eigenvectors also have *eigenvalues* which can be seen as weights which are proportional to the amount of mass or in our case HU intensity located in that given principle axis. These eigenvectors can be used to quantify different shape-based metrics, for example: roundness, which is the difference between the largest eigenvalues of the smallest enclosing and the largest enclosed ellipse.

*Minkowski functionals* originate from integral geometry (120). They can be used to calculate the *Euler characteristic* or *genus* which is a parameter resembling the connectivity of the data points. It is estimated by calculating the number of voxel groups with information minus the enclosed regions where there is no signal (121). By taking a different threshold of our image, we can calculate separate parameters for each image.

These values can be used to describe the connectedness of different intensity values in the image.

Fractal geometry quantifies self-symmetry by examining repeating patterns at different scales. Objects showing no fractal dimension scale their characteristics exponentially depending on the dimension. For example, if we enlarge a line by 2, its length will increase to  $2^1$ , since it is a 1D object. If we scale one side of a square by 2, then the area of the square will increase by  $2^2$  since it is a 2D object. A cube's volume would increase to  $2^3$  if we were to grow one of its sides by 2. However, fractals act differently. Fractal dimensions do not have to be integers as topological dimensions. In example, the fractal dimension of a line can be anywhere between 1 and 2. This means, if we magnify our line, we see more details that we were not able to see at larger scales. Therefore, if we enlarge a line whose fractal dimension is not equal to its topological dimension, then its length would be more than twice as long. Actually, the length is undefined, since the more we magnify our object the more details we see, therefore this would affect the overall length of the line.

*Fractal dimensions* measure self-symmetry of objects and quantify how the detail of the object changes as we change our scale (122). *Rényi dimensions* can be used to calculate fractal dimensions generally. The *box-counting dimension* or *Minkowski–Bouligand dimension* is the easiest concept. We calculate how many voxels are occupied by the object. We repeat this at increasing scales. Then we plot the number of voxels containing the object versus the reciprocal of the scale on a log-log plot. The slope of the line will be equal to the box-counting dimension (123, 124).

#### **1.5.4. Transform-based metrics**

Images are a vast number of signals arranged in the *spatial domain*. The images can also be transformed into a different domain, such as the *frequency domain*, without losing any information. This is basically a different representation of the same information. In the frequency domain the rate at which image intensity values change is used to describe the image instead of assigning intensity values to spatial coordinates.

*Fourier transform* takes a signal and decomposes it to sinusoidal waves which represent the frequencies present in the signal. Applying the Fourier transform on an image transforms it from the spatial domain to the frequency domain. *Gabor transform* first

filters the image by applying a Gaussian-filter before the Fourier transform is performed. In the frequency domain the images can be filtered from specific components, such as noise, or individual characteristics such as edges can be emphasized or cancelled out. Using the *inverse Fourier transform*, we can receive back our modified image in the spatial domain where we can extract different statistics from the filtered image.

*Wavelet transform* are similar to Fourier transforms in that they also convert the image into the frequency domain, but not all spatial information is lost (125). We can weigh how much frequency and how much spatial information we wish to keep, but we can only increase our spatial information by sacrificing frequency precision, and vice versa. A family of transformed images can be received from different parameter settings, which can be further analyzed using different statistics.

## 1.6. Artificial intelligence: the hope to synthesize it all

The increased amount of information can then be analyzed using novel data analytic techniques such as ML and deep learning (DL), which utilize the power of big data to build predictive models, which seek to mimic human intelligence, artificially. These techniques may decrease inter-reader variations, increase the amount of quantitative information and improve the diagnostic and prognostic accuracy, while reducing subjectivity and biases (126).

The amount of available medical information is increasing at exponential speeds (127). Currently the difficulty is not how to get medical big data, but how to organize, analyze and clinically utilize the data collected in biobanks and repositories. Conventional statistical methods utilize probability theory to create mathematical formulas which describe the relationship between variables. This approach is usually acceptable for population-based analysis, but in the era of precision medicine and big data, new methods are needed which can model complex non-linear relationships and infer results specific to each case rather than being generally true to the population.

Humans are skilled at identifying unique patterns and inferring complex connections between data. However, this *natural intelligence* is not based on mathematical equations, but on observations and experience. AI tries to create models which think and act humanly and rationally (128). To achieve this, first inputs are needed from the environment. Then this information and the previous observations need to be stored and analyzed, which can be performed using ML. ML is an analytic method a sub-division of AI, which uses computer algorithms with the ability to learn from data, without being explicitly programmed (129). These algorithms are similar to the human learning process, in the sense that more data they are trained on, the better they perform. In the medical field the main goal of ML techniques is to harvest the potential of big data to discover new relationships in the data that conventional statistical methods might not be able to. While conventional statistical approaches can provide a clear mathematical formula regarding the relationship of the variables, not all methods of ML are capable of describing the connection between parameters through mathematical equations. Instead they build their predictive models based-on patterns in the data experienced through training, and make prediction by comparing a new instance to previous similar

occurrences (130). Nevertheless, ML has the potential to revolutionize medical through providing more accurate predictions of outcomes (*figure 9*).

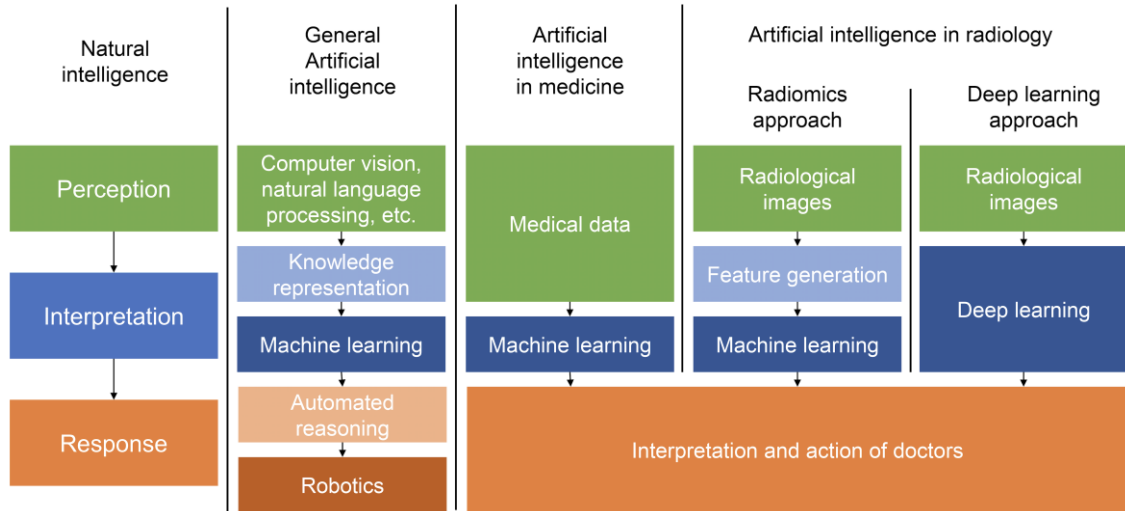


**Figure 9.** Flow diagram showing the possible implementations of artificial intelligence to medical data and showing the similarities and differences between radiomics, machine learning and deep learning (126).

Artificial intelligence tries to mimic natural intelligence through automating processes that are needed for an intelligent system to perceive, interpret and respond to its surroundings. The medical field can utilize the benefits of machine learning to help interpret the large amounts of data currently available in medicine. In case of radiological images, radiomics can be used to extract vast amounts of information, which can be inputs to machine learning. On the other hand, deep learning automatically identifies imaging markers in the neural network while training, rather than defining them beforehand.

## **2. OBJECTIVES**

### **2.1. Defining the effect of using coronary CTA to assess coronary plaque burden as opposed to ICA**

Even though ICA is considered as the gold-standard of coronary atherosclerosis imaging, the unique ability of coronary CTA to image atherosclerosis itself may provide the opportunity to identify CAD earlier. Therefore, our objective was to compare coronary CTA and ICA regarding semi-quantitative plaque burden assessment and to assess the effect of imaging modality on cardiovascular risk classification.

### **2.2. Defining the potential of using radiomics to identify napkin-ring sign plaques on coronary CTA**

High-risk plaque morphologies such as the NRS have proven to have additive value in identifying patients vulnerable to MACE. However, the reproducibility of such metrics is poor. As there was no implementation of radiomics to cardiovascular imaging, we sought to assess whether calculation of radiomic features is feasible on coronary lesions. Furthermore, we aimed to evaluate whether radiomic parameters can differentiate between plaques with or without NRS.

### **2.3. Defining the potential of radiomics to identify invasive and radionuclide imaging markers of vulnerable plaques on coronary CTA**

Invasive imaging modalities due to their better spatial resolution have a better accuracy to identify rupture prone plaques. Furthermore, radionuclide imaging is capable of identifying plaques with inflammation and micro-calcifications which are hallmarks of plaque vulnerability. We wished to assess whether coronary CTA radiomics could outperform current standards to identify invasive and radionuclide imaging markers of high-risk plaques described by intravascular ultrasound (IVUS), optical coherence tomography (OCT) and NaF<sup>18</sup>-Positron Emission Tomography (NaF<sup>18</sup>-PET).

## **2.4. Defining the potential effect of image reconstruction algorithms on reproducibility of volumetric and radiomic signatures of coronary lesions on coronary CTA**

Recent advancements in image reconstruction have led to the wide-spread utilization of novel iterative reconstruction techniques. As volumetric and radiomics features are calculated from the voxel values themselves, it is important to know how these may change the calculated metric values. Therefore, our primary aim was to assess whether filtered back projection (FBP), hybrid (HIR) or model-based (MIR) iterative reconstruction have any significant effect on volumetric and radiomic parameters of coronary plaques. Furthermore, we sought to evaluate the impact of the type of binning and the number of bins used for discretization on radiomic parameter values.

## **2.5. Defining the potential of using radiomic markers as inputs to machine learning models to identify advanced atherosclerotic lesions as assessed by histology**

The plaque attenuation pattern scheme outperforms conventional plaque classification to identify advanced atherosclerotic lesions. Recently, quantitative histogram analysis and the area or volume of low attenuation plaque have been proposed as markers of high-risk lesions. Furthermore, radiomics represents a process of extracting thousands of imaging markers from radiological images describing the heterogeneity and spatial complexity of lesions. These quantitative features can be used as the input to ML. Therefore, our objective was to compare the diagnostic performance of radiomics-based ML with visual and histogram-based plaque assessment to identify advanced coronary lesions using histology as reference standard.

### **3. METHODS**

#### **3.1. Study design and statistics for defining the effect of using coronary CTA to assess coronary plaque burden as opposed to ICA**

The Genetic Loci and the Burden of Atherosclerotic Lesions study enrolled patients who were referred to coronary CTA due to suspected CAD (NCT01738828). Detailed description of the patient population, including the inclusion and exclusion criteria, has been published (131). This ancillary study was designed as a nested single-center observational cohort study in patients who were referred to ICA due to obstructive CAD detected by CTA. The study was approved by the Institutional Ethical Review Board, and all participants provided written informed consent (131).

Out of the 868 patients enrolled by our institution, we selected individuals who underwent both coronary CTA and ICA within 120 days. In total, 71 patients (mean age  $61.6 \pm 9.0$  years, 36.6% female) were included in our analysis. In 58 patients, ICA followed CTA based on clinical findings, while in 13 cases ICA was carried out before CTA. These patients were either referred to CTA after revascularization due to atypical chest pain (7 patients) or were referred to left atrial angiography before radiofrequency ablation (6 patients). An average of 40.2 days passed between the two examinations.

All images were randomly and independently analyzed. Semi-quantitative plaque burden quantification of ICA images was performed by an interventional cardiologist. A minimum of 5 projections of the left and right coronary systems were acquired in each patient. All coronary segments were analyzed blinded to CTA results, using a minimum of 2 projections. Coronary CTA images were analyzed by a cardiologist.

A total of 1016 segments were assessed based on the 18-segment SCCT classification with both modalities (132). We excluded 16 segments due to presence of coronary stents leading to overall 1000 analyzed segments. All segments were scored for the presence or absence of plaque (0: Absent; 1: Present) and the degree of stenosis (0: None; 1: Minimal (<25%); 2: Mild (25%-49%); 3: Moderate (50%-69%); 4: Severe (70%-99%) or 5: Occlusion (100%)). In case multiple lesions were present in a segment, the observers recorded the highest degree of stenosis for that segment. In each patient, segment involvement score (SIS) was used to quantify the number of segments with any plaque,

whereas segment stenosis score (SSS) was calculated by summing the stenosis scores of each segment. Indexed values were calculated by dividing the SIS and SSS scores by the number of segments: segment involvement score index (SISi) = SIS / number of segments; segment stenosis score index (SSSi) = SSS / number of segments.

Based on Bittencourt et al. the extent of CAD was classified as non-extensive (SIS  $\leq$  4) or extensive (SIS > 4) and obstructive (at least one segment with  $\geq$ 50% stenosis) or non-obstructive (no segment with  $\geq$ 50% stenosis).(133) Patients were classified as extensive obstructive, nonextensive obstructive, extensive nonobstructive or nonextensive nonobstructive based on ICA and also CTA results.

All continuous variables are expressed as mean  $\pm$  SD, while categorical variables are expressed as frequencies and percentages. Presence of plaque was compared using the chi-square test between modalities. Sensitivity, specificity, positive predictive value and negative predictive value were calculated to assess the diagnostic accuracy of CTA as compared to ICA as reference standard. SIS, SSS and SISi, SSSi were compared using the paired t-test between modalities. Reclassification rate was calculated by dividing the number of people who shifted groups based on the two modalities by the total study population. All statistical calculations were performed using SPSS software (SPSS version 23; IBM Corp., Armonk, NY). A *p*-value of 0.05 or less was considered significant.

### **3.2. Study design and statistics for defining the potential of using radiomics to identify napkin-ring sign plaques on coronary CTA**

From 2674 consecutive coronary CTA examinations due to stable chest pain we retrospectively identified 39 patients who had NRS plaques. Two expert readers reevaluated the scans with NRS plaques. To minimize potential variations due to inter-reader variability the presence of NRS was assessed using consensus read. Readers excluded 7 patients due to insufficient image quality and 2 patients due to the lack of the NRS, therefore 30 coronary plaques of 30 patients (NRS group; mean age: 63.07 years [interquartile range (IQR): 56.54; 68.36]; 20% female) were included in our analysis. As a control group, we retrospectively matched 30 plaques of 30 patients (non-NRS group; mean age: 63.96 years [IQR: 54.73; 72.13]; 33% female) from our clinical database with excellent image quality. To maximize similarity between the NRS and the non-NRS plaques and minimize parameters potentially influencing radiomic features, we matched the non-NRS group based on degree of calcification and stenosis, plaque localization, tube voltage and image reconstruction.

All plaques were graded for luminal stenosis and degree of calcification. Furthermore, plaques were classified as having low attenuation if the plaque cross-section contained any voxel with  $<30$  HU and having spotty calcification if a  $<3$  mm calcified plaque component was visible.

Image segmentation and data extraction was performed using a dedicated software tool for automated plaque assessment (QAngioCT Research Edition; Medis medical imaging systems bv, Leiden, The Netherlands). After automated segmentation of the coronary tree the proximal and distal end of each plaque were set manually. Automatic lumen and vessel contours were manually edited by an expert if needed (134). From the segmented datasets 8 conventional quantitative metrics (lesion length, area stenosis, mean plaque burden, lesion volume, remodeling index, mean plaque attenuation, minimal and maximal plaque attenuation) were calculated by the software. The voxels containing the plaque tissue were exported as a DICOM dataset using a dedicated software tool (QAngioCT 3D workbench, Medis medical imaging systems bv, Leiden, The Netherlands). Smoothing or interpolation of the original HU values was not performed. Representative examples of

volume rendered and cross-sectional images of NRS and non-NRS plaques are shown in *figure 10*.

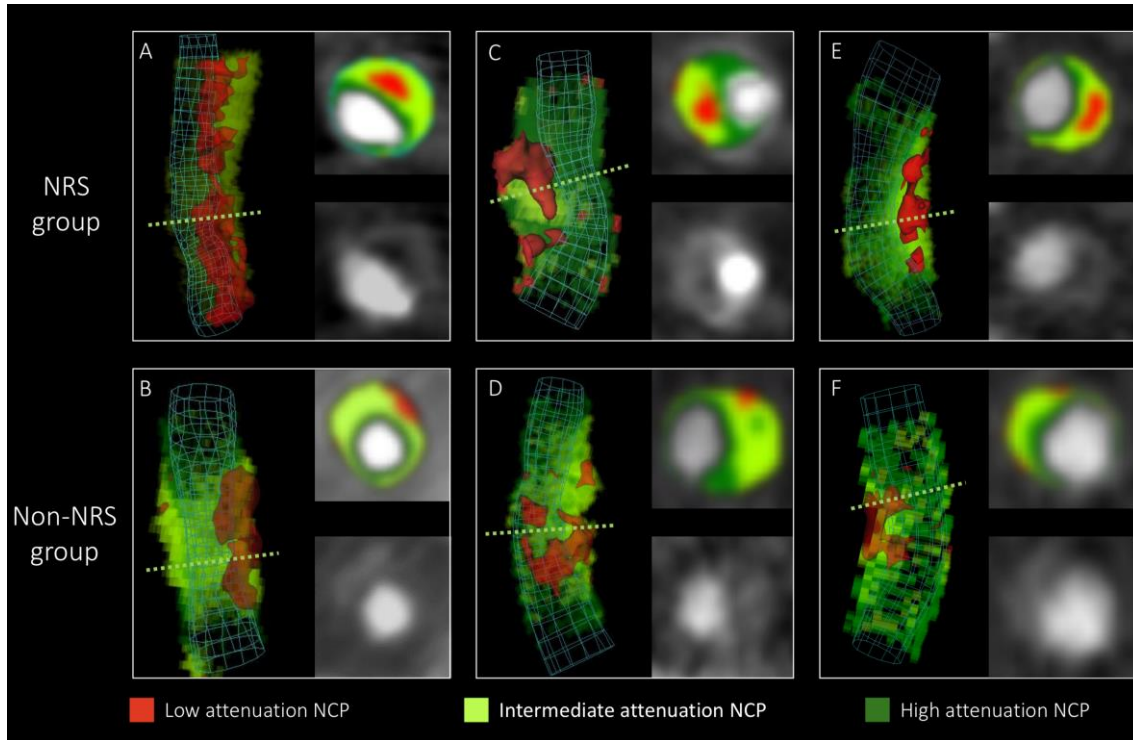


**Figure 10.** *Representative images of plaques with or without the napkin ring sign (135).* Volume rendered and cross-sectional images of plaques with napkin-ring sign in the top row (A, C, E) and their corresponding matched plaques in the lower row (B, D, E). Green dashed lines indicate the location of cross-sectional planes. Colors indicate different CT attenuation values.

NCP: non-calcified plaque; NRS: napkin-ring sign

We developed an open source software package in the R programming environment (Radiomics Image Analysis (RIA)) which is capable of calculating hundreds of different radiomic parameters on 2D and 3D datasets (136). We calculated 4440 radiomic features for each coronary plaque using the RIA software tool. Detailed description on how radiomic features were calculated can be found in published literature (135).

Binary variables are presented as frequencies and percentages, while ordinal and continuous variables are presented as medians and IQR due to possible violations of the normality assumption. For robust statistical estimates, parameters between the NRS and the non-NRS group were compared using the permutation test of symmetry for matched samples using conditional Monte Carlo simulations with 10,000 replicas (137). For diagnostic performance estimates, we conducted receiver operating characteristics (ROC)

analysis and calculated area under the curve (AUC) with bootstrapped CI values using 10,000 samples with replacement and calculated sensitivity, specificity, positive and negative predictive value by maximizing the Youden index (138). To assess potential clusters among radiomic parameters, we conducted linear regression analysis between all pairs of the calculated 4440 radiomic metrics. The  $1-R^2$  value between each radiomic feature was used as a distance measure for hierarchical clustering. The average silhouette method was used to evaluate the optimal number of different clusters in our dataset (139). Furthermore, to validate our results we conducted a stratified 5-fold cross-validation using 10,000 repeats of the three best radiomic and conventional quantitative parameters. The model was trained on a training set and was evaluated on a separate test set at each fold using ROC analysis. The derived curves were averaged and plotted to assess the discriminatory power of the parameters. The number of additional cases classified correctly was calculated as compared to lesion volume. The McNemar test was used to compare classification accuracy of the given parameters as compared to lesion volume (140). Due to the large number of comparisons, we used the Bonferroni correction to account for the family wise error rate. Bonferroni correction assumes that the examined parameters are independent of each other, thus the question is not how many parameters are being tested, but how many independent statistical comparisons will be made. Therefore, based on methods used in genome-wide association studies we calculated the number of informative parameters accounting for 99.5% of the variance using principal component analysis (141, 142). Overall, 42 principal components identified, therefore p values smaller than 0.0012 ( $0.05/42$ ) were considered significant. All calculations were done in the R environment (143).

### **3.3. Study design and statistics for defining the potential of radiomics to identify invasive and radionuclide imaging markers of vulnerable plaques on coronary CTA**

The current study is a post-hoc retrospective analysis of patients who have also undergone coronary CTA due to suspected coronary artery disease between March and October of 2015 within 90 days prior to invasive angiography. In total, 27 patients with at least one moderate (40-70%) stenosis on the proximal or mid-portion of any major coronary artery were included in our study. All patients underwent NaF<sup>18</sup>-PET and invasive coronary angiography. During the invasive procedure, both IVUS and OCT was performed. Two patients were excluded due to inadequate image quality of imaging procedures. Overall, 44 plaques of 25 patients using all four imaging modalities were investigated. The study protocol was approved by the institutional review board and was in accordance with the Declaration of Helsinki. All patients provided written informed consent before enrolment. Coronary CTA images were obtained in accordance with the Society of Cardiovascular Computed Tomography Guidelines, with a 64-detector row scanner platform (Somatom Definition; Siemens Medical Solutions, Forchheim, Germany) (45). The following conventional morphologic adverse plaque characteristics were reported by a core lab (Severance Cardiovascular Hospital, Seoul, Republic of Korea) blinded to all other results: low attenuation plaque (density  $\leq 30$  HU), positive remodelling (remodelling index  $\geq 1.1$ ), spotty calcification (density  $> 130$  HU and diameter  $< 3$  mm), and NRS (ring-like attenuation pattern with peripheral high attenuation tissue surrounding a central lower attenuation area) (46, 54). Lesions with at least two of the four morphologic adverse plaque characteristics were regarded as two-feature positive high-risk plaque on coronary CTA (144).

Each coronary plaque was segmented blinded to other imaging modality results using a semi-automated software tool (QAngioCT Research Edition; Medis medical imaging systems bv, Leiden, The Netherlands) at a designated core laboratory (Semmelweis University, Budapest, Hungary). Lumen and vessel contours were manually adjusted if necessary. Using the segmented datasets, voxels containing plaque were exported as a DICOM image (QAngioCT 3D workbench, Medis medical imaging systems bv, Leiden, The Netherlands). Based on the Hounsfield units (HU) values, the volume of low

attenuation non-calcified plaque (<30 HU), non-calcified plaque (30-130 HU) and calcified plaque volume (>130 HU) was calculated (145, 146).

Four different classes of radiomic features were used in our analysis. First-order statistics, GLCM parameters, GLRLM metrics (147, 148). For these calculations, similar value voxels need to be grouped together. This is done through discretization of HU values to a given number of bins. In our analysis, we discretized the lesions into 2, 8, 32 equally sized (range of values were equally wide) bins creating 3 replicas of the image. All GLCM and GLRLM metrics were calculated using all three types of binning. Geometry-based statistics were calculated on the original image, as well as each discretized component.

Radiomic features were analysed at a core facility (Semmelweis University, Budapest, Hungary). Overall 935 different radiomic parameters were calculated using the RIA software package in the R environment (136, 143). Of these parameters 44 were first-order statistics; 342 were statistics calculated from GLCM; 33 were statistics extracted from GLRLM, while 516 were geometry-based statistical parameters (135). The median time to calculate all 935 parameters for each plaque was: 7.3 [range: 3.8-12.6] minutes.

All patients underwent NaF<sup>18</sup>-PET before invasive angiography. Electrocardiography-gated NaF<sup>18</sup>-PET images were obtained using a dedicated PET/CT scanner (Biograph 40 TruePoint; Siemens Healthcare, Germany) 60 minutes after the injection of 3 MBq/kg of NaF<sup>18</sup>. Images were reconstructed in 4 frames and fused with the non-enhanced CT images. Diastolic phases (frames of 50% to 75% and 75% to 100% of the R–R intervals) were evaluated blinded to all other results at a core facility (Seoul National University Hospital – Nuclear Medicine, Seoul, Republic of Korea). Maximum standard uptake value was measured and corrected for blood pool activity measured in the inferior vena cava to provide tissue-to-background ratio measurements. The highest tissue-to-background ratio value measured on two diastolic-phase images was adopted for the final analysis. Plaques with NaF<sup>18</sup> uptakes higher than 25% were considered as NaF<sup>18</sup>-positive lesions (149, 144).

Selective invasive coronary angiography was performed utilizing standard techniques. IVUS images were acquired according to the American College of Cardiology Clinical Expert Consensus Document on Standards for Acquisition, Measurement and Reporting of Intravascular Ultrasound Studies (150, 151). The presence of echo attenuation (hypoechoic plaque with deep ultrasound attenuation) was analysed blindly at a core lab

(Seoul National University Hospital – CV Research Institute, Seoul, Republic of Korea). All OCT data was assessed blindly at a core laboratory for the presence of TCFA (144). Continuous variables are presented as medians and interquartile ranges, while categorical variables are reported as frequencies and percentages. Calculating diagnostic accuracy on the whole dataset, would be overly optimistic and ungeneralizable to other datasets. Therefore, we conducted a stratified 5-fold cross-validation with 1,000 repeats, which decreases the bias of overfitting and provides a robust estimate of the expected performance in real-life (152). A ROC curve was calculated for each repeat resulting in overall 1000 ROC curves. These ROC curves were averaged to model the diagnostic performance on the whole population. AUC was calculated as an overall measure of diagnostic accuracy. To compare the diagnostic accuracy of conventional and radiomic coronary CTA features, we calculated the two-sided Wilcoxon signed-rank test to compare the distribution of AUC values resulting from the repeated cross-validations. We calculated CI as the 2.5 and 97.5 percentile of the AUC distribution resulting from the repeated cross-validations. All statistical calculations were done in the python environment using the Scikit-learn package (153).

### **3.4. Study design and statistics for defining the potential effect of image reconstruction algorithms on reproducibility of volumetric and radiomic signatures of coronary lesions on coronary CTA**

Between August 1<sup>st</sup> and October 31<sup>st</sup> 2017, we retrospectively identified 20 non-calcified, 20 partially calcified and 20 calcified coronary atherosclerotic plaques of 60 patients (age  $60.4 \pm 9.8$ ; female:  $n=16$ ) showing at least 25% stenosis on excellent image quality coronary CTA scans. All images were acquired using a 256-slice scanner (Brilliance iCT 256, Philips Healthcare) with prospective ECG-triggered acquisition mode. Images were acquired in cranio-caudal direction during a single breath-hold in inspiration. Four-phasic injection protocol with 90-100 ml of Iomeprol contrast agent was used (Iomeron 400, Bracco Ltd) for the coronary CTA examinations (154). Examinations were performed using  $128 \times 0.625$  mm detector collimation, 270 ms gantry rotation time, 120 kV, mAs 250-300 depending on patient's body mass index and chest size. All images were reconstructed to a  $512 \times 512$  matrix using an XCB kernel with a slice thickness of 0.8 mm and 0.4 mm spacing between slices. All images were reconstructed using FBP, HIR (iDOSE4 level 5, Philips Healthcare) and MIR (IMR level 2, Philips Healthcare).

For image quality assessment, we measured the signal-to-noise ratio (SNR), which was defined as the mean coronary luminal CT attenuation in HU adjacent to the lesion divided by the standard deviation of the CT number in the aorta measured in a region of interest at least  $2 \text{ cm}^2$  at the level of the left main. Contrast-to-noise ratio (CNR) was defined as the mean luminal HU minus the perivascular HU at the site of the plaque divided by the standard deviation of the aortic HU. All measurements were performed on a clinical workstation (IntelliSpace portal, Philips Healthcare).

An expert reader manually segmented the coronary plaques on HIR image using a dedicated software tool (QAngioCT Research Edition; Medis medical imaging systems bv) (155). HIR images were chosen as they are available for each vendor and are most frequently used for plaque analysis. Voxels containing plaque tissue were extracted as a DICOM image with dimensions identical to the original image using a dedicated software (QAngioCT 3D workbench, Medis medical imaging systems bv). This DICOM image was used as a mask to select the same voxels from all three reconstructions. Using the same segmentation ensured that only the change in voxel values attributable to different

image reconstructions affected the results. For volumetric plaque analysis, voxels were grouped into calcified plaque volume (>130 HU), high attenuation (90–129 HU), intermediate attenuation (30–89 HU) and low attenuation (<30 HU) non-calcified plaque volumes (156).

Overall, 44 first-order metrics describing the distribution of HU values, 114 GLCM parameters enumerating the frequency at which similar HU values co-occur next to each other, and 11 GLRLM features quantifying the prevalence of many similar voxel values in a line next to each other, were calculated based-on a prior publication (135). Before calculation of GLCM and GLRLM statistics, images need to be preprocessed. To calculate parameters describing the spatial heterogeneity of a lesion, HU values need to be first discretized into given ranges (bins), since minimal differences in HU value have little effect on heterogeneity and therefore can be considered similar values. Therefore, replicate images were created by discretizing the voxel HU values either to equally sized bins where the discrete bins span equal ranges (i.e. 10-20; 20-30; 30-40; etc.) or to equally probable bins, where equal proportion of data are present in each bin (i.e. 10%; 10%; 10%; etc.). Radiomic parameters were calculated on all three reconstructions. GLCM and GLRLM parameters were calculated using with 2, 4, 8, 16, 32, 64, 128 and 256 number of bins both for equally sized and equally probable binning. This resulted in 2\*8 variations for each reconstruction of each plaque. Therefore, for first-order statistics  $3*60$  (number of reconstruction\*number of plaques) =180 values, for GLCM and GLRLM  $3*60*2*8$  (number of reconstructions\*number of plaques\*number of different types of discretization\*number of different bins) = 2880 different values were available for each radiomics parameter.

Categorical variables are presented as frequencies and percentages, while continuous variables are shown as averages and SD. Intra-class correlation coefficient (ICC) was calculated to assess the reproducibility of the radiomic parameters with regards to different reconstructions. ICC values greater than 0.80 were considered good, values above 0.90 were considered to have excellent reproducibility. To assess which parameters have an independent influence on radiomic values, we conducted linear regression analysis. Models included plaque composition (non-calcified, partially calcified, calcified) and reconstruction algorithms where HIR was considered as reference. In addition, for GLCM and GLRLM parameters the type of binning and the number of bins

were also added to the model. Beta ( $\beta$ ) and p values are reported for each independent variable.  $\Delta R^2$  was calculated for each independent variable by subtracting the  $R^2$  value calculated when considering all variables except the given variable from the regression model which considered all variables.  $\Delta R^2$  was calculated as an effect size measure, to show the proportion of variance attributable to a given parameter. In case of radiomic parameters, due to the large number of outcome parameters, results are summarized on Manhattan plots, where the given statistical results (ICC or  $\Delta R^2$ ) are plotted on the y axis while the radiomic parameters are lined up on the x axis in consecutive order and color coded based-on which family of radiomic metrics they belong to (157). All statistical calculations were done in the R environment. A p value of  $p < 0.05$  was considered statistically significant.

### **3.5. Study design and statistics for defining the potential of using radiomic markers as inputs to machine learning models to identify advanced atherosclerotic lesions as assessed by histology**

The donor hearts were provided by the International Institute for the Advancement of Medicine (Jessup, Pennsylvania). Inclusion criteria consisted of: men between 40 and 70 years with a history of myocardial infarction or coronary artery disease proven by diagnostic tests (54, 158). Donors with coronary artery bypass grafts were excluded. The maximum allowed warm and cold ischemia time was 6 and 15 hours respectively. Overall 7 isolated donor hearts (mean age of the donors:  $52.3 \pm 5.3$ , 7 men) were investigated. The cause of death was stroke (n=6) and suicide (n=1).

The heart preparation was described previously (54, 158). The fresh hearts were imaged without formalin fixation using a 64-detector row CT scanner (High-Definition, GE Discovery, CT 750HD, GE Healthcare, Milwaukee). For coronary CTA a 3% mixture of iodinated contrast material (iopamidol; Isovue 370, Bracco Diagnostics, Milan, Italy) with methylcellulose (Methocel, DOW Chemical Company, Midland, Michigan) was used. All datasets were acquired using sequential acquisition mode,  $64 \times 0.625$  mm collimation; 0.35-s rotation time; tube voltage: 120 kV; tube current time product: 500 mAs. The images were reconstructed with a slice thickness of 0.6 mm and an increment of 0.4 mm using an adaptive iterative reconstruction technique (ASIR, GE Healthcare, Milwaukee, Wisconsin). Coronary CTA images were analyzed on an offline workstation (Leonardo, Siemens Healthcare, Erlangen, Germany). After CT imaging, the coronary arteries were excised with surrounding tissue and the side branches were ligated. The preparation and the coronary CTA imaging was done within 4 hours after receiving the heart to avoid potential post-mortem changes of the tissue.

Histologic preparation and analysis were performed at a pathology institute that specializes in cardiovascular histopathology by a certified pathologist with over 20-years of experience (CVPath Institute, Gaithersburg, MD). Paraffin sections were obtained in 1.5-mm and 2-mm increments (382 and 185 cuts, respectively) of the coronary arteries. Coronary artery segments with no visible atherosclerotic disease were sectioned every 5 mm (44 cuts). The thickness of a single histological section was 6  $\mu\text{m}$ . All sections were stained with Movat pentachrome (159). Each cross-section was classified according the

modified American Heart Association scheme into the following categories: adaptive intima thickening, pathological intimal thickening, fibrous plaque, early fibroatheroma, late fibroatheroma and the thin cap fibroatheroma (160, 161). Among these, adaptive and pathological intimal thickening and fibrous plaque were considered early atherosclerotic lesions, while early and late fibroatheroma and thin cap fibroatheroma were categorized as advanced lesions.

The method of co-registration of histological slides with coronary CTA images was described previously (54). An experienced reader performed the qualitative reading of all (training and validation dataset) coronary CTA cross-sections and classified them based on the traditional and the plaque attenuation pattern scheme as described in detail previously (54). All readings were done blinded to the histological results and were performed with a fixed window setting (700 Hounsfield units (HU) width, 200 HU level). All coronary CTA cross-sections were manually segmented using a dedicated open-source software (3D Slicer v4.8.1., Boston, Massachusetts, open-source) based on the direct plaque tracing method (162, 163). Plaque segmentations were used as a mask image to select the voxels which contained plaque. Images were exported in NRRD files and imported into RIA (v1.4.1, Budapest, Hungary, open-source) software package in the R environment (136). For histogram-based assessment, the area of low attenuation (<30 HU) and the average HU values were calculated from the segmented coronary CTA images.

Segmented image voxel values were then discretized into 16, 32 and 64 equally sized (bins having identical HU ranges) and also equally probable bins (bins having the same amount of voxels) using the RIA software resulting in six additional images (136) (136, 164). Overall 44 first-order statistics (describing the HU distribution of the lesion) were calculated on the original voxel values. 114 gray level co-occurrence matrix (describing how often voxels with similar value co-occur next to each other) and 11 gray level run length matrix parameters (describing how many similar values voxel are next to each other) on the discretized images resulting in  $6*114=684$  and  $6*11=66$  parameters. Among geometry-based parameters (describing the spatial characteristics of the lesions such smoothness or self-symmetry): surface, surface ratio of a specific discretized value to total surface and fractal box counting, information and correlation dimensions were calculated on the original image and each value of the discretized image resulting in

$5+(2*16*5)+(2*32*5)+(2*64*5)=1125$  parameters. Altogether 1919 parameters were calculated for each cross-section. Detailed description of each radiomic parameter has been published previously (135, 24).

For unbiased estimates of diagnostic accuracy, our dataset was randomly split into a training-set and a validation-set (75%, n=333; 25%, n=112, respectively). Eight independent ML models were trained on the training-set. To select the best model and the best hyperparameters for each model, we conducted 5-fold cross-validation on the training-set. This technique randomly selects 80% of the dataset on which the models are trained and then evaluates them on the remaining 20% (tuning-set). This is repeated five times until each cross-section was part of the tuning-set once. Diagnostic performance was assessed using ROC curves' AUC value. The average of the 5 AUC values during cross-validation was used to describe the discriminatory power of that specific model using given hyperparameter values. This process was repeated 1000 times for each type of ML model by assigning random values to the hyperparameter values using randomized grid search (165, 153).

Model building consisted of the following steps: 1: exclusion of parameters with 0 variance. 2: robust scaling of parameters using the median and interquartile range. 3: selecting parameters which were under a random significance level (hyperparameter) using the false positive rate test or the family-wise error rate test. 4: conducting principal component analysis describing a randomly assigned (hyperparameter) portion of the variance. 5: fitting the given ML model with randomly assigned hyperparameters. The following types of ML models were fitted: logistic regression, K-nearest neighbors, random forest, least angle regression, naïve Bayes, Gaussian process classifier, decision trees, deep neural networks (153). The ML model that provided the best results on the training-set was then applied to the validation-set. In case of the plaque attenuation pattern scheme and histogram-based measurements, a logistic regression model was fitted to the training-set which was then applied to the validation-set to evaluate discriminatory power. All model building was done in the python environment (v3.6.2, Beaverton, Oregon, open-source) using the Scikit-learn package (v0.19.1, open-source) (153). Code used for analysis can be accessed at: [https://github.com/martonkolossvary/radiomics\\_ex-vivo\\_src](https://github.com/martonkolossvary/radiomics_ex-vivo_src)

Continuous variables are presented as average and standard deviation, while categorical variables are reported as frequencies and percentages. Categorical variables were compared using the chi-square test. Diagnostic accuracy of visual assessment, histogram-based methods and radiomics-ML were evaluated on the validation-set using ROC curves. 95% CI of the AUC values were calculated and the ROC curves were compared using the DeLong method (166).

All statistical calculations were done in the python (v3.6.2, Beaverton, Oregon, open-source) and R (v3.4.2, Vienna, Austria, open-source) environments. A two-sided p value <0.05 was considered statistically significant.

## 4. RESULTS

### 4.1. Comparison of quantity of coronary atherosclerotic plaques detected by coronary CTA versus ICA

Detailed demographics can be found in *table 1*. Coronary CTA detected coronary artery plaque in 49% (487/1000) of the segments, whereas ICA showed coronary plaques in 24% (235/1000) of all segments ( $p < 0.001$ ). Of the 235 positive segments with ICA, corresponding segments on CTA was also positive in 94%. CTA detected atherosclerotic plaque in 35% (266/765) of coronary segments where ICA was negative. 36% (95/266) of these plaques were non-calcified, 38% (102/266) were mixed and 26% (69/266) were calcified plaques on CTA. When considering the severity of coronary stenosis only seen by CTA, 79% of plaques caused minimal or mild luminal stenosis (211/266). Conversely, ICA detected plaque only in 3% (14/513) of segments where CTA was negative.

**Table 1.** Demographic information regarding patients who underwent coronary CTA and ICA (167).

Variable	n = 71
Age (years)	61.6 ± 9.0
Female	26 (37 %)
Body Mass Index (kg/m <sup>2</sup> )	27.9 ± 4.3
Hypertension	51 (72 %)
Diabetes Mellitus	13 (18 %)
HDL (mmol/l)	1.34 ± 0.4
LDL (mmol/l)	3.0 ± 1.3
Triglyceride (mmol/l)	1.7 ± 0.8
Cholesterol (mmol/l)	4.8 ± 1.6
Time between coronary CT angiography and invasive coronary angiography (days)	40.2 ± 32.1

Regarding segment scores, CTA showed more than two times as many segments with plaque compared to ICA, and also the overall degree of stenosis caused by the plaques was almost twice. Summary of segment score analysis is shown in *table 2*.

**Table 2.** Comparison of semiquantitative scores between coronary CT angiography and invasive coronary angiography (167). Segment involvement score (SIS) and index (SISi), segment stenosis score (SSS) and index (SSSi) all significantly differed between CTA and ICA images.

	CTA	ICA	<i>p</i>
SIS	6.9 ± 3.0	3.3 ± 2.0	<0.001
SISi	0.5 ± 0.2	0.2 ± 0.1	<0.001
SSS	16.4 ± 8.8	9.4 ± 6.8	<0.001
SSSi	1.2 ± 0.6	0.7 ± 0.5	<0.001

Analysis of diagnostic accuracy revealed high sensitivity with moderate specificity (96% CI: 87-100%; 53 % CI: 28-77%, respectively) with high positive and negative predictive value (87%, CI: 75-94%; 82 %, CI: 48-100%, respectively).

Out of 71 patients, based on CTA results 72% (51/71) was classified as extensive obstructive, 3% (2/71) as extensive non-obstructive, 13% (9/71) as non-extensive obstructive and 13% (9/71) as non-extensive non-obstructive. Using ICA based measurements, 27% (19/71) of the patients was extensive obstructive, 1% (1/71) was extensive non-obstructive, 49% (35/71) was non-extensive obstructive and 23% (16/71) was non-extensive non-obstructive. Overall 52% (37/71) of the patients moved to a higher risk category, while 1% (1/71) moved to a lower category using CTA based measurements as compared to ICA based measurements. Graphical representation of the risk groups and exact number of patients moving from one group to another can be found in *figure 11*.

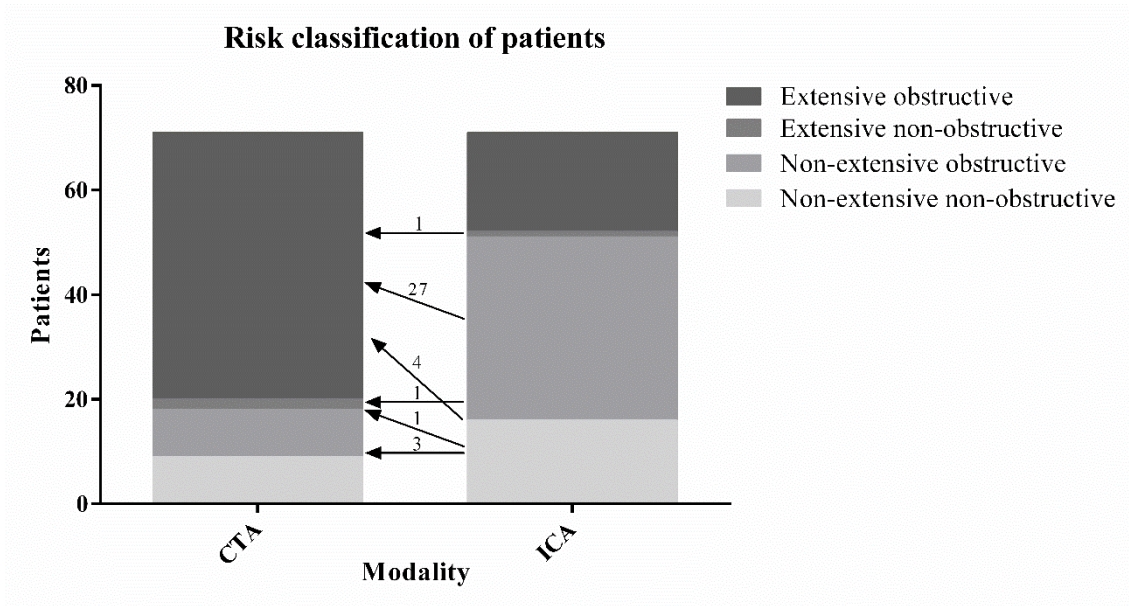


**Figure 11.** Risk classification of patients based on coronary computed tomography angiography and invasive coronary angiography (167).

Overall, 52% of patients moved to a higher risk category. The number of patients switching to higher risk groups are represented by arrows. Only 1% of patients moved to a lower risk category using CTA-based measurements as compared to ICA-based measurements (not shown in Figure).

CTA: CT angiography; ICA: invasive coronary angiography

## 4.2. Identification of napkin-ring sign plaques using radiomics

There was no significant difference between the NRS and non-NRS groups regarding patient characteristics and scan parameters (*table 3*). Furthermore, we did not observe any significant difference in qualitative plaque characteristics and image quality parameters (*table 4*) implying successful matching of the two groups. Median number of voxels contributing to the NRS coronary plaques (1928 [IQR: 1413;2560]) did not show statistical difference as compared to the number of voxels in the non-NRS group (1286 [IQR: 1001;1768]),  $p=0.0041$ . Among conventional quantitative imaging parameters, there was no significant difference between NRS and non-NRS plaques (*table 4*). Furthermore, none of the conventional parameters had an AUC value above 0.8 (*table 5*).

**Table 3.** Patient characteristics and scan parameters (135).

	NRS group (n=30)		non-NRS group (n=30)		p
<b>Demographics</b>					
Age (years)	63.07	[56.54; 68.36]	63.96	[54.73; 72.13]	0.86
Male gender, n (%)	24	(80%)	20	(67%)	0.16
BMI (kg/m <sup>2</sup> )	28.06	[25.06; 29.91]	26.93	[23.91; 29.32]	0.34
<b>Cardiovascular risk factors</b>					
Hypertension n (%)	19	(63%)	18	(60%)	0.78
Diabetes mellitus n (%)	25	(83%)	26	(87%)	0.65
Dyslipidemia n (%)	16	(53%)	18	(60%)	0.62
Current smoker n (%)	20	(67%)	21	(70%)	0.80
<b>Scan parameters</b>					
Total dose length product (mGy x cm)	362.00	[356.00; 367.00]	358.20	[253.20; 367.00]	0.42
Pixel spacing (mm)	0.41	[0.39; 0.43]	0.43	[0.39; 0.45]	0.30

**Table 4. Plaque and image quality characteristics (135).**

	Napkin-ring sign group (n=30)		Non-napkin ring sign group (n=30)		p
<b>Plaque composition</b>					1.00
Non-calcified, n (%)	19	(63%)	19	(63%)	
Partially calcified, n (%)	11	(37%)	11	(37%)	
Calcified, n (%)	0	(0%)	0	(0%)	
<b>Luminal stenosis</b>					1.00
Minimal (1-24%)	11	(37%)	11	(37%)	
Mild (25-49%)	11	(37%)	11	(37%)	
Moderate (50-69%)	6	(20%)	6	(20%)	
Severe (70-99%)	2	(7%)	2	(7%)	
<b>Stenosis localization</b>					1.00
Left main	2	(7%)	2	(7%)	
Left anterior descending	20	(66%)	20	(66%)	
Left circumflex	2	(7%)	2	(7%)	
Right coronary	6	(20%)	6	(20%)	
<b>Image quality</b>					
Contrast-to-noise ratio	21.94	[18.61; 28.80]	23.42	[18.64; 26.57]	0.70
Signal-to-noise ratio	18.69	[15.84; 24.13]	20.52	[16.33; 22.53]	0.59
<b>High-risk plaque features</b>					
Napkin-ring sign, n (%)	30	(100%)	0	(0%)	<0.0001
Low attenuation, n (%)	26	(87%)	19	(63%)	0.06
Spotty calcification, n (%)	10	(33%)	9	(30%)	0.99
<b>Conventional quantitative metrics</b>					
Lesion length (mm)	13.62	[10.42; 17.02]	13.48	[10.99; 17.71]	0.70
Lesion volume (mm <sup>3</sup> )	134.88	[105.68; 190.76]	88.88	[70.02; 143.98]	0.02
Mean plaque burden	0.59	[0.52; 0.66]	0.51	[0.44; 0.59]	0.003

Lumen area stenosis	0.41	[0.15; 0.53]	0.28	[0.19; 0.49]	0.38
Vessel wall remodeling index	1.03	[0.92; 1.46]	1.09	[0.97; 1.20]	0.55
Mean plaque attenuation (HU)	114.67	[85.54; 148.99]	156.75	[138.46; 208.37]	0.002
Minimal plaque attenuation (HU)	-83.00	[-101.75; -58.00]	-60.00	[-84.75; -47.00]	0.10
Maximal plaque attenuation (HU)	523.00	[451.00; 794.50]	634.50	[454.00; 898.00]	0.63

---

**Table 5.** *Diagnostic performance of conventional quantitative parameters and novel radiomic parameters to identify plaques with the napkin-ring sign (135).*

	Area under the curve	CI	Sensitivity	Specificity	PPV	NPV
<b>Conventional</b>						
<b>quantitative</b>						
<b>metrics</b>						
Mean plaque attenuation	0.770	[0.643; 0.880]	0.533	0.933	0.889	0.667
Mean plaque burden	0.702	[0.563; 0.826]	0.700	0.667	0.677	0.690
Lesion volume	0.683	[0.543; 0.817]	0.700	0.700	0.700	0.700
Minimal plaque attenuation	0.647	[0.498; 0.788]	0.700	0.700	0.700	0.700
Maximal plaque attenuation	0.553	[0.408; 0.696]	0.700	0.500	0.583	0.625
Remodeling index	0.547	[0.398; 0.700]	0.633	0.633	0.633	0.633
Lumen area stenosis	0.539	[0.389; 0.687]	0.567	0.667	0.630	0.606
Lesion length	0.508	[0.359; 0.654]	0.933	0.133	0.519	0.667
<b>First-order</b>						
<b>statistics</b>						
30 <sup>th</sup> decile	0.827	[0.716; 0.921]	0.833	0.733	0.758	0.815
First quartile	0.826	[0.712; 0.922]	0.767	0.800	0.793	0.774
Harmonic mean	0.823	[0.708; 0.922]	0.767	0.800	0.793	0.774
Trimean	0.812	[0.696; 0.910]	0.867	0.667	0.722	0.833
Geometric mean	0.803	[0.684; 0.902]	0.633	0.900	0.864	0.711
<b>Gray level co- occurrence</b>						

**matrix****parameters**

Interquartile range	0.867	[0.769; 0.948]	0.700	0.900	0.875	0.750
Lower notch	0.866	[0.763; 0.948]	0.967	0.633	0.725	0.950
Gauss right focus	0.859	[0.759; 0.940]	0.767	0.867	0.852	0.788
Median						
absolute deviation from the mean	0.856	[0.744; 0.946]	0.867	0.767	0.788	0.852
Sum energy	0.848	[0.740; 0.937]	0.967	0.633	0.725	0.950

**Gray level****run length****matrix****features**

Short run low gray level emphasis	0.918	[0.822; 0.996]	1.000	0.867	0.882	1.000
Long run low gray level emphasis	0.894	[0.799; 0.970]	1.000	0.733	0.789	1.000
Long run emphasis	0.888	[0.791; 0.962]	0.933	0.767	0.800	0.920
Run percentage	0.871	[0.771; 0.951]	1.000	0.667	0.750	1.000
Short run emphasis	0.853	[0.747; 0.942]	1.000	0.633	0.732	1.000

**Geometry****based****parameters**

Surface ratio of component 2 to total surface	0.890	[0.801; 0.960]	0.833	0.833	0.833	0.833
---	-------	----------------	-------	-------	-------	-------

Surface ratio of component 7 to total surface	0.888	[0.796; 0.958]	0.933	0.733	0.778	0.917
Surface ratio of component 22 to total surface	0.883	[0.787; 0.959]	0.767	0.900	0.885	0.794
Surface ratio of component 14 to total surface	0.882	[0.790; 0.954]	0.833	0.833	0.833	0.833
Surface ratio of component 3 to total surface	0.864	[0.767; 0.943]	0.867	0.767	0.788	0.852

---

Overall, 4440 radiomic parameters were calculated for each atherosclerotic lesion. Out of all calculated radiomic parameters, 20.6% (916/4440) showed a significant difference between plaques with or without NRS (all  $p < 0.0012$ ). Of the 44 calculated first-order statistics 25.0% (11/44) was significant. Out of the 3585 calculated GLCM statistics 20.7% (742/3585) showed a significant difference between the two groups. Among the 55 GLRLM parameters 54.5% (30/55) were significant, while 17.6% (133/756) of the calculated 756 geometry-based parameters had a  $p < 0.0012$ . A Manhattan plot of the p values of the calculated radiomic parameters is shown in *figure 12*. Detailed statistics of the assessed radiomic parameters have been published (135).

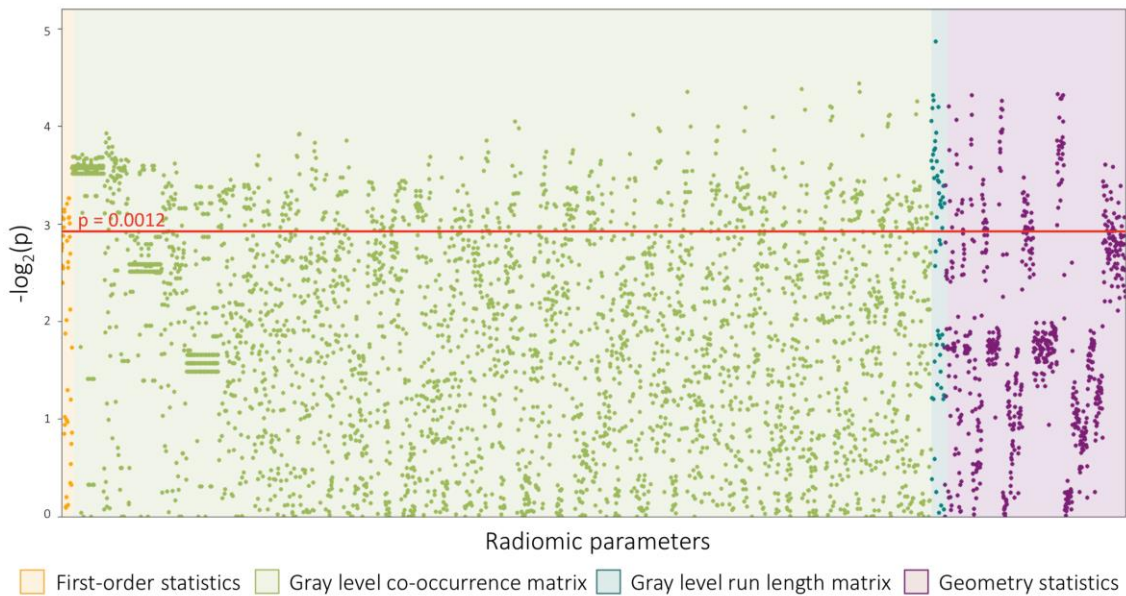


**Figure 12.** Manhattan plot of all 4440 calculated p values. (135).

The Manhattan plot shows all 4440 calculated p values comparing napkin-ring sign (NRS) vs. non-NRS plaques and their distribution among the different classes of radiomic parameters. Radiomic features are lined up on the x axis, while the  $-\log_2(p)$  values are plotted on the y axis. The red horizontal line indicates the Bonferroni corrected p value of 0.0012. Radiomic parameters above the red line were considered statistically significant.

Among all 4440 radiomic parameters 9.9% (440/4440) had an AUC value greater than 0.80. Out of the 44 calculated first-order statistics 18.2% (8/44) had an AUC value larger than 0.80. Of the 3585 calculated GLCM parameters 9.7% (348/3585) of the AUC values was above 0.80. Among the 55 GLRLM parameters 54.5% (30/55) had an AUC value above 0.80, while out of the calculated 756 geometry-based parameters 7.1% (54/756)

had an AUC value above 0.80. Of all radiomic parameters short run low gray level emphasis, long run low gray level emphasis, surface ratio of component 2 to total surface, long run emphasis and surface ratio of component 7 to total surface had the five highest AUC values (0.918; 0.894; 0.890; 0.888 and 0.888, respectively). Detailed diagnostic accuracy statistics of conventional quantitative features and of the five best radiomic features for each group are shown in *table 5*, while detailed diagnostic accuracy results of radiomic parameters have been published previously (135).

Results of the linear regression analysis conducted between all pairs of the calculated 4440 radiomic metrics are summarized using a heatmap (*figure 13*). Hierarchical clustering showed several different clusters where parameters are highly correlated with each other (represented by the red areas in *figure 13*), but only have minimal relationship with other radiomic features (represented by the black areas in *figure 13*). Cluster analysis revealed that the optimal number of clusters among radiomic features in our dataset is 44. 5-fold cross-validation using 10,000 repeats was used to simulate the discriminatory power of the three best radiomic and conventional parameter. Average ROC curves of the cross-validated results are shown in *figure 14*. Radiomic parameters had higher AUC values as compared to conventional quantitative features and identified lesions showing the NRS significantly better as compared to conventional metrics. Detailed results are shown in *table 6*.

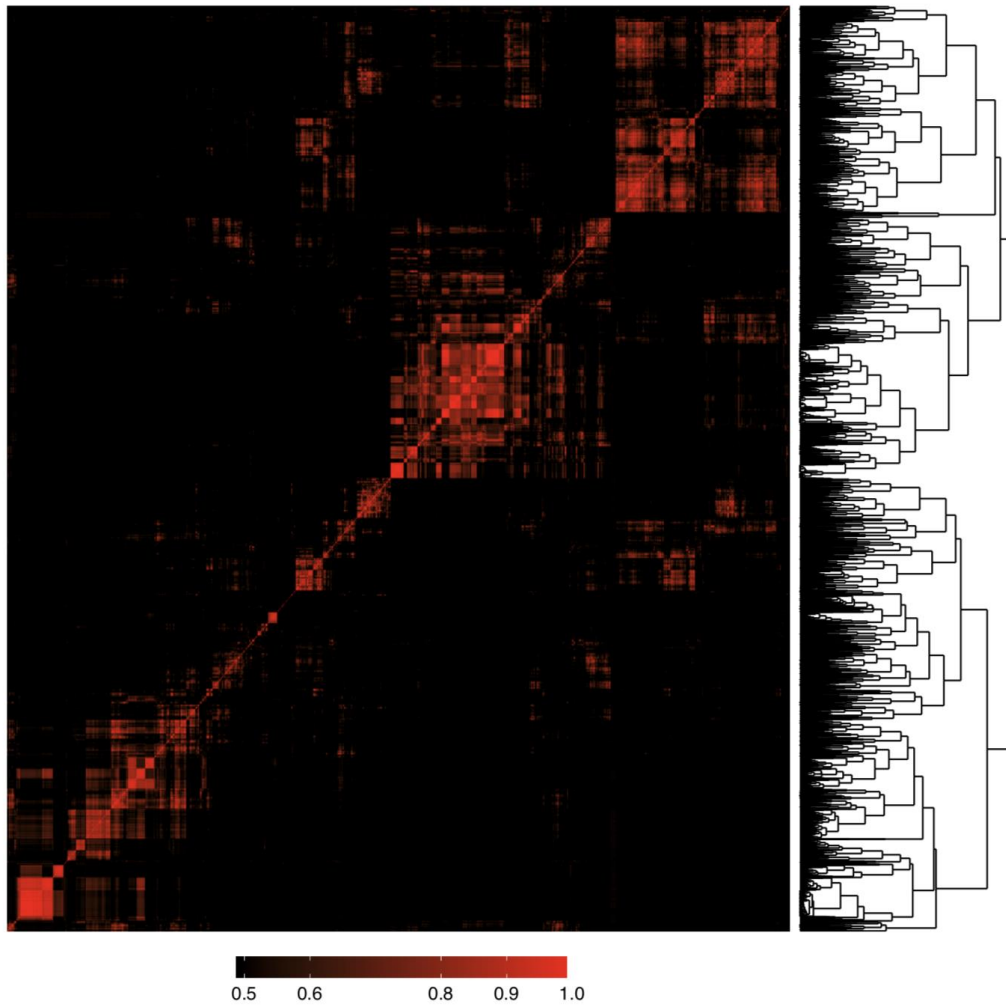


**Figure 13.** Heatmap and clustering dendrogram of all 4440 calculated radiomic parameters. (135).

Heatmap of the covariance matrix of all 4440 radiomic features. Each parameter was compared to all other parameters using linear regression analysis. Features were clustered based on  $R^2$  values of the corresponding regression models and plotted along both axes.  $R^2$  values below 0.5 are black, while greater values are shown in red with increasing intensity. The  $1-R^2$  values was used as a distance measure between parameters and used for hierarchical clustering. The resulting clustering dendrogram can be seen on the right of the image. Cluster analysis indicated that the optimal number of clusters is 44 based on our radiomics dataset.

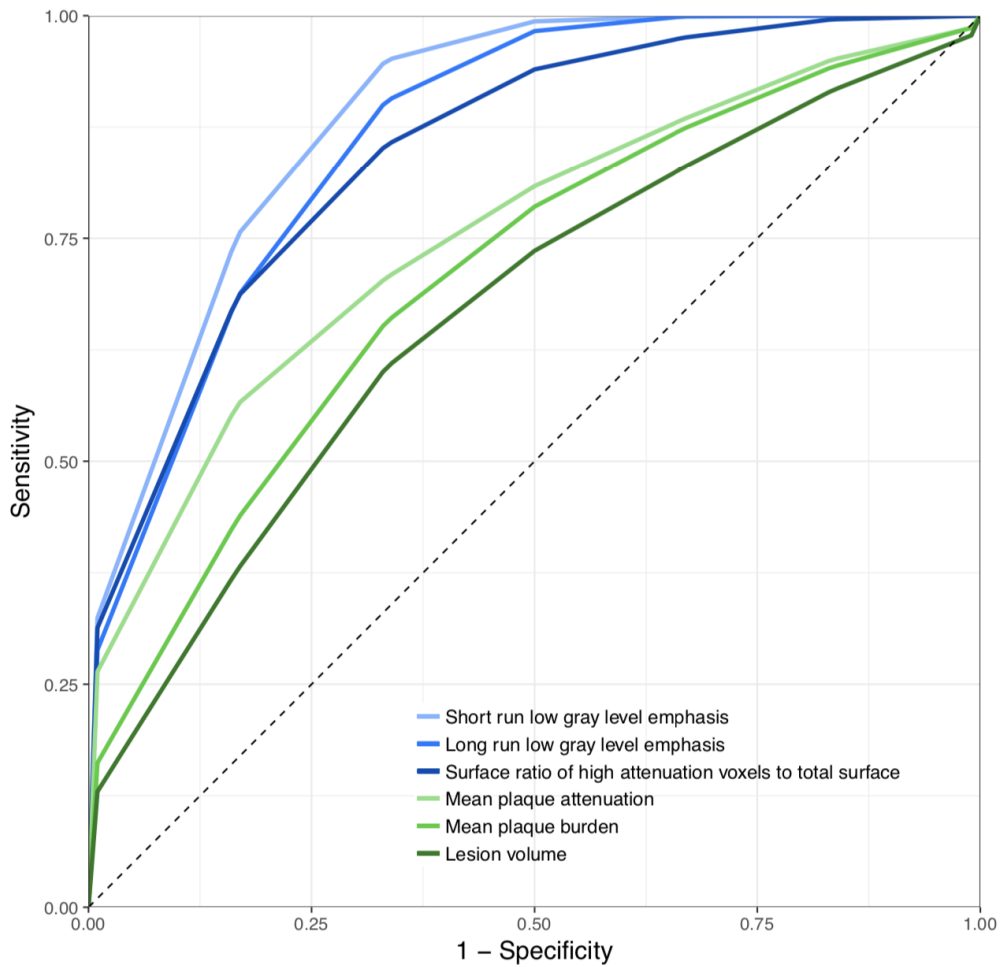


**Figure 14.** Stratified five-fold cross-validated receiver operating characteristic curves of the best radiomic and conventional quantitative parameters. (135).

Stratified five-fold cross-validated receiver operating characteristic curves using 10,000 repeats. Radiomic parameters (blue) have higher discriminatory power to identify plaques with napkin-ring sign as compared to conventional quantitative metrics (green). Detailed performance measures can be found in *table 6*.

**Table 6.** Area under the curve values of stratified five-fold cross-validated receiver operating characteristic curves of the best radiomic and conventional quantitative parameters to identify plaques with napkin-ring sign.

	Area under the curve	Additional cases classified correctly as compared to lesion volume	p
Short run low gray level emphasis	0. 889	30.6%	<0.0001
Long run low gray level emphasis	0. 866	23.3%	<0.0001
Surface ratio of high attenuation voxels to total surface	0. 848	16.7%	<0.0001
Mean plaque attenuation	0. 754	5.1%	0.0002
Mean plaque burden	0. 709	4.6%	0.0009
Lesion volume	0. 668	-	-

### 4.3. Identification of invasive and radionuclide imaging markers of vulnerable plaques using radiomic analysis of coronary CTA

Overall, 44 plaques were analysed (*table 7*); 30/44 (68.2%) plaques showed attenuation on IVUS, 7/44 (15.9%) showed TCFA on OCT and in 11/44 (25.0%) cases >25% NaF<sup>18</sup> uptake was present. All plaques which were TCFA by OCT also showed attenuation on IVUS. Out of the 30 attenuated plaques 8/30 (26.7%) showed radionuclide uptake on NaF<sup>18</sup>-PET, however none of the TCFA plaques showed >25% NaF<sup>18</sup> uptake.

**Table 7.** *Patient and lesion characteristics.*

<b>Patients</b>	
Age (year)	62 [IQR: 59-69]
Male (n, %)	23 (92)
Body mass index (kg/m <sup>2</sup> )	25 [IQR: 22-27]
Cardiovascular risk factors	
Hypertension (n, %)	12 (48.0)
Diabetes mellitus (n, %)	8 (32.0)
Hypercholesterolemia (n, %)	18 (72.0)
Current smoker (n, %)	6 (24.0)
<b>Lesion Characteristics</b>	
Lesion locations	
Left main to left anterior descending (n, %)	34 (77.3)
Left circumflex (n, %)	3 (6.8)
Right coronary artery (n, %)	7 (15.9)
Quantitative coronary angiography	
Reference vessel diameter (mm)	3.3 [IQR: 2.9-3.6]
Minimal lumen diameter (mm)	1.7 [IQR: 1.4-2.3]
Diameter stenosis (%)	45 [IQR: 33-52]
Lesion length (mm)	11.2 [IQR: 7.9-14.5]

Among radiomic metrics, 35/935 (3.7%) had AUC values between 0.70 and 0.79 and 311/935 (33.3%) had values between 0.60-0.69 to identify IVUS-attenuated plaque. Among radiomic metrics fractal box counting dimension of high attenuation (component 30 when discretizing to 32 equally sized bins) voxels showed the best diagnostic accuracy to identify attenuated plaques on IVUS (AUC: 0.72; CI: 0.65-0.78), whereas among the conventional CT metrics, non-calcified plaque volume showed the best discriminatory value (AUC: 0.59; CI: 0.57-0.62),  $p < 0.001$  (figure 15).

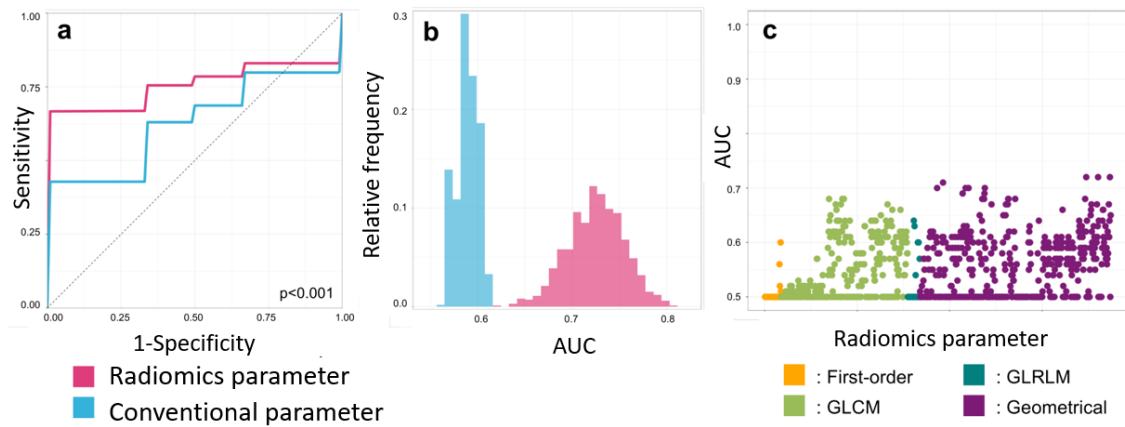


**Figure 15.** Diagnostic evaluation of radiomics and conventional CT parameters to identify attenuated plaques on IVUS (168).

Panel a: shows average ROC curves of the best radiomic (pink): fractal box counting dimension of high attenuation voxels (component 30 when discretizing to 32 equally sized bins); and the best conventional (blue) parameter: non-calcified plaque volume, which were calculated by averaging the ROC curves after 1000 repeats of the 5-fold cross validation process. Panel b: distribution of the AUC values calculated during the 5-fold cross validation process repeated 1000 times. Dashed lines indicate the means of the AUC distributions. Results are based on the analysis of 44 plaques of 25 patients. Panel c: Manhattan-plot of radiomic features' AUC values. Radiomic parameters are situated in consecutive order on the x axis, while their corresponding AUC values to identify attenuated plaques on IVUS are shown on the y axis.

AUC: area under the curve; IVUS: intravascular ultrasound; GLCM: grey level co-occurrence matrix; GLRLM: grey level run length matrix; ROC: receiver operating characteristics

Overall, 1/935 (0.1%) of all radiomic parameters had AUC values between 0.80-0.89, 44/935 (4.7%) between 0.70-0.79 and 219/935 (23.4%) had values between 0.60 and 0.69 to identify OCT-TCFA. Fractal box counting dimension of high attenuation (component 8 when discretizing to 8 equally sized bins) voxels had the best diagnostic accuracy to identify OCT-TCFA (AUC: 0.80; CI: 0.72-0.88), while the presence of low attenuation plaque showed the best discriminatory power among conventional metrics (AUC: 0.66; CI: 0.58-0.73),  $p < 0.001$  (figure 16).

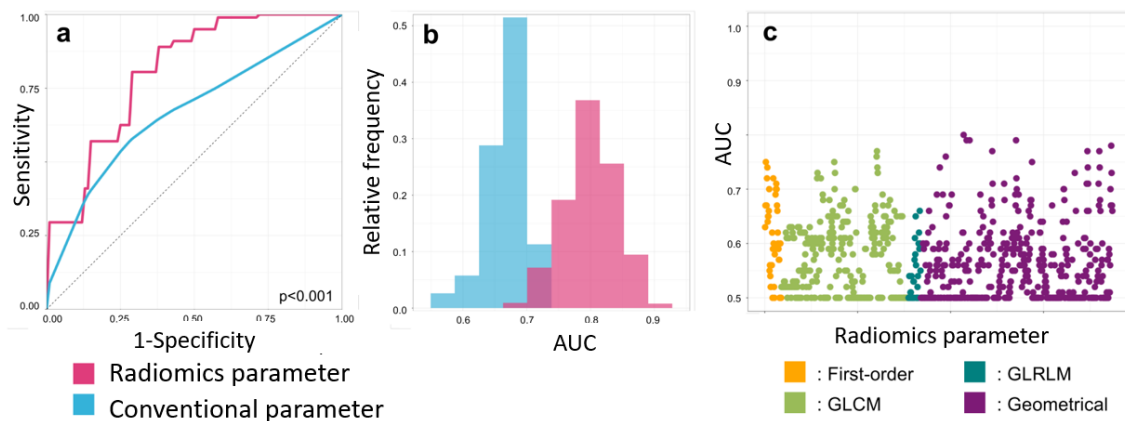


**Figure 16.** Diagnostic evaluation of radiomics and conventional CT parameters to identify OCT-TCFA (168).

Panel a: shows average ROC curves of the best radiomic (pink): fractal box counting dimension of high attenuation voxels (component 8 when discretizing to 8 equally sized bins); and the best conventional (blue) parameter: presence of low attenuation, which were calculated by averaging the ROC curves after 1000 repeats of the 5-fold cross validation process. Panel b: distribution of the AUC values calculated during the 5-fold cross validation process repeated 1000 times. Dashed lines indicate the means of the AUC distributions. Results are based on the analysis of 44 plaques of 25 patients. Panel c: Manhattan-plot of radiomic features' AUC values. Radiomic parameters are situated in consecutive order on the x axis, while their corresponding AUC values to identify OCT-TCFA are shown on the y axis.

AUC: area under the curve; GLCM: grey level co-occurrence matrix; GLRLM: grey level run length matrix; OCT: optical coherence tomography; ROC: receiver operating characteristics; TCFA: thin-cap fibroatheroma

Overall, 30/935 (3.2%) of the radiomic parameters had AUC values between 0.80 and 0.89, 331/935 (35.4%) had values between 0.70-0.79 and 232/935 (24.8%) had values between 0.60-0.69 to identify NaF<sup>18</sup>-positivity. Out of the radiomic parameters the surface of high attenuation (component 8 when discretizing to 8 equally sized bins) voxels had the best diagnostic accuracy (AUC: 0.87; CI: 0.82-0.91), while the presence of two high risk features on CTA had the best discriminatory power (AUC: 0.65; CI: 0.64-0.66) among conventional parameters to identify marked radionuclide uptake using NaF<sup>18</sup>-PET,  $p < 0.001$  (figure 17).

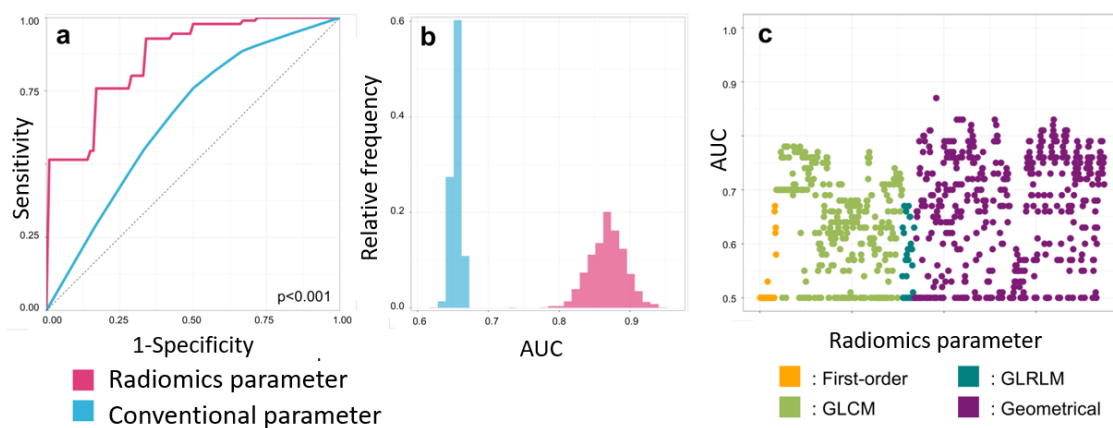


**Figure 17.** Diagnostic evaluation of radiomics and conventional CT parameters to identify radionuclide activity on NaF<sup>18</sup>-PET.(168).

Panel a: shows ROC curves of the best radiomic (pink): surface of high attenuation voxels (component 8 when discretizing to 8 equally sized bins); and the best conventional (blue) parameter: presence of two high risk features, which were calculated by averaging the ROC curves after 1000 repeats of the 5-fold cross validation process. Panel b: distribution of the AUC values calculated during the 5-fold cross validation process repeated 1000 times. Dashed lines indicate the means of the AUC distributions. Results are based on the analysis of 44 plaques of 25 patients. Panel c: Manhattan-plot of radiomic features' AUC values. Radiomic parameters are situated in consecutive order on the x axis, while their corresponding AUC values to identify radionuclide activity on NaF<sup>18</sup>-PET are shown on the y axis.

AUC: area under the curve; GLCM: grey level co-occurrence matrix; GLRLM: grey level run length matrix; NaF<sup>18</sup>-PET: Sodium-fluoride positron emission tomography; ROC: receiver operating characteristics

Representative volume rendered CT images of coronary plaques showing attenuation on IVUS, TCFA on OCT and positivity on NaF<sup>18</sup>-PET can be found in *figure 18*.

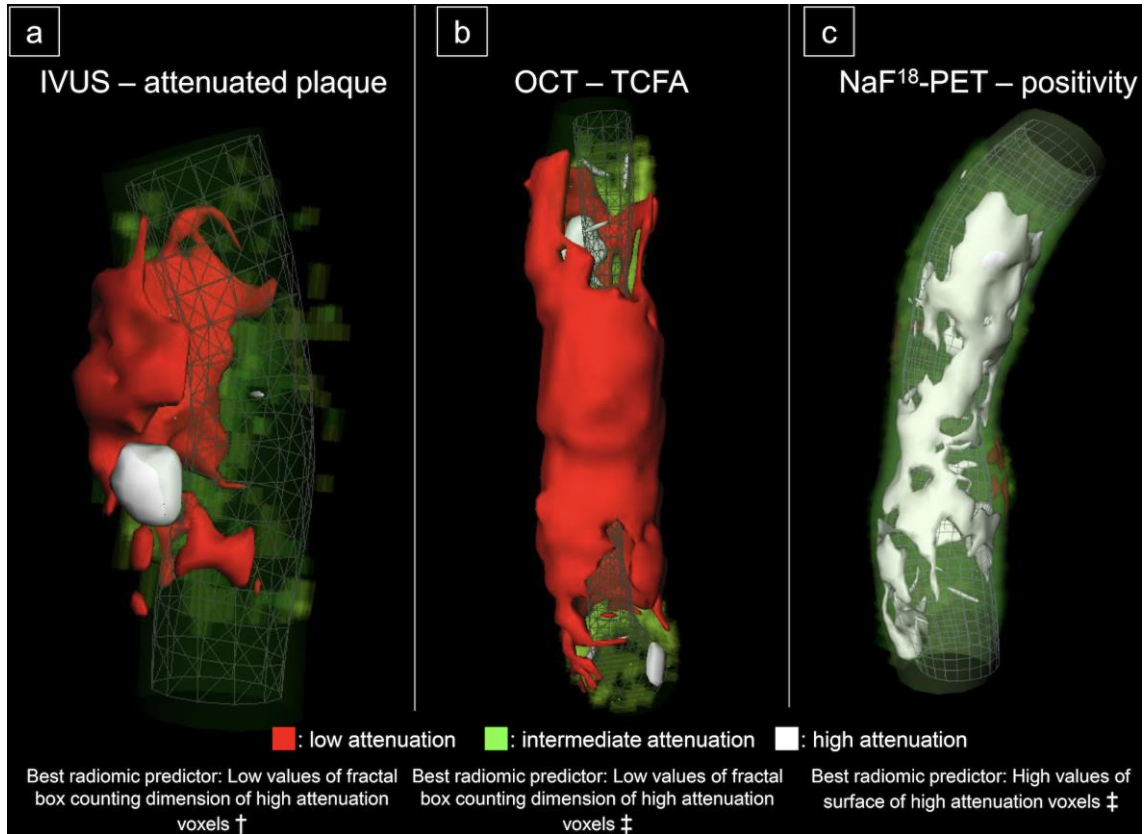


**Figure 18.** Representative curved multiplanar and volume rendered CT images of three coronary plaques corresponding to specific invasive and radionuclide imaging markers of plaque vulnerability(168).

Panel a: shows a coronary lesion which scored the lowest on fractal box counting dimension of high attenuation voxels (component 30 when discretizing to 32 equally sized bins) which was indicative of attenuated plaque on IVUS (AUC: 0.72 [0.65-0.78]). Panel b: depicts a coronary plaque which scored the lowest on fractal box counting dimension of high attenuation voxels (component 8 when discretizing to 8 equally sized bins) which was suggestive of OCT-TCFA (AUC: 0.80 [0.72-0.88]). Panel c: shows a coronary lesion which had a high surface of high attenuation voxels (component 8 when discretizing to 8 equally sized bins) which was the best parameter to identify NaF<sup>18</sup>-PET positivity (AUC: 0.87 [0.82-0.91]).

AUC: area under the curve; IVUS: intravascular ultrasound; NaF<sup>18</sup>-PET: NaF<sup>18</sup>-Positron Emission Tomography; OCT-TCFA: optical coherence tomography identified thin-cap fibroatheroma;

†: component 30 when discretizing to 32 equally sized bins; ‡: component 8 when discretizing to 8 equally sized bins

#### 4.4. Effect of image reconstruction algorithms on volumetric and radiomics features derived from coronary CTA

Aorta SD, CNR and SNR had low ICC values between image reconstructions (0.46, 0.60, 0.63; respectively), while lumen and pericoronary fat mean HU had excellent and good reproducibility (0.99, 0.83; respectively). Image reconstruction had a significant effect on aorta SD, CNR and SNR values with large  $\Delta R^2$ , while lumen or pericoronary fat mean HU values were unaffected by the different algorithms. Detailed results of image quality reproducibility can be found in *table 8*.

**Table 8.** *Reproducibility of image quality parameters.* ICC and linear regression models were calculated to assess the degree to which reconstruction algorithms might affect image quality parameters.  $\Delta R^2$  represents  $R^2$  change if image reconstruction is added to the model considering plaque composition.  $R^2$  total represents  $R^2$  values for models considering both plaque composition and image reconstruction. FBP: filter back projection; ICC: intraclass correlation coefficient; MIR: Model-based iterative reconstruction (164).

Parameter	ICC	FBP $\beta$	FBP p	MIR $\beta$	MIR p	$\Delta R^2$	$R^2$ total
Aorta SD	0.46	19.04	<0.0001	-11.98	<0.0001	0.63	0.63
Lumen mean Hounsfield unit	0.99	-0.19	0.99	-4.20	0.81	0.00	0.02
Pericoronary fat mean Hounsfield unit	0.83	-1.85	0.74	6.40	0.25	0.01	0.04
Contrast to noise ratio	0.60	-7.32	<0.0001	12.85	<0.0001	0.62	0.63
Signal to noise ratio	0.63	-6.26	<0.0001	11.21	<0.0001	0.60	0.60

All volumetric plaque parameters showed excellent reproducibility (ICC>0.97; all). None were affected by the type of image reconstruction. Detailed results of plaque volume reproducibility can be found in *table 9*.

**Table 9.** *Reproducibility of plaque volumes.* ICC and linear regression models were calculated to assess the degree to which reconstruction algorithms might affect plaque volumes.  $\Delta R^2$  represents  $R^2$  change if image reconstruction is added to the model considering plaque composition.  $R^2$  total represents  $R^2$  values for models considering both plaque composition and image reconstruction. ICC: intraclass correlation coefficient; MIR: Model-based iterative reconstruction (164).

Parameter	ICC	FBP $\beta$	FBP $p$	MIR $\beta$	MIR $p$	$\Delta R^2$	$R^2$ total
Low attenuation non-calcified plaque	0.98	-0.31	0.90	-2.43	0.31	0.01	0.28
Intermediate attenuation non-calcified plaque	0.98	-1.37	0.68	1.24	0.70	0.00	0.24
High attenuation non-calcified plaque	0.98	0.05	0.97	0.32	0.84	0.00	0.24
Calcified plaque	1.00	1.63	0.87	0.86	0.93	0.00	0.26

Regarding radiomic parameters, all had excellent reproducibility ( $ICC > 0.90$ ) except for: first-order parameters: mode, harmonic mean and minimum ( $ICC$ : 0.45, 0.76; 0.84, respectively), and GLCM parameters: inverse difference sum and sum variance ( $ICC$ : 0.01, 0.04; respectively). Manhattan plot of  $ICC$  values can be found in *figure 19*.

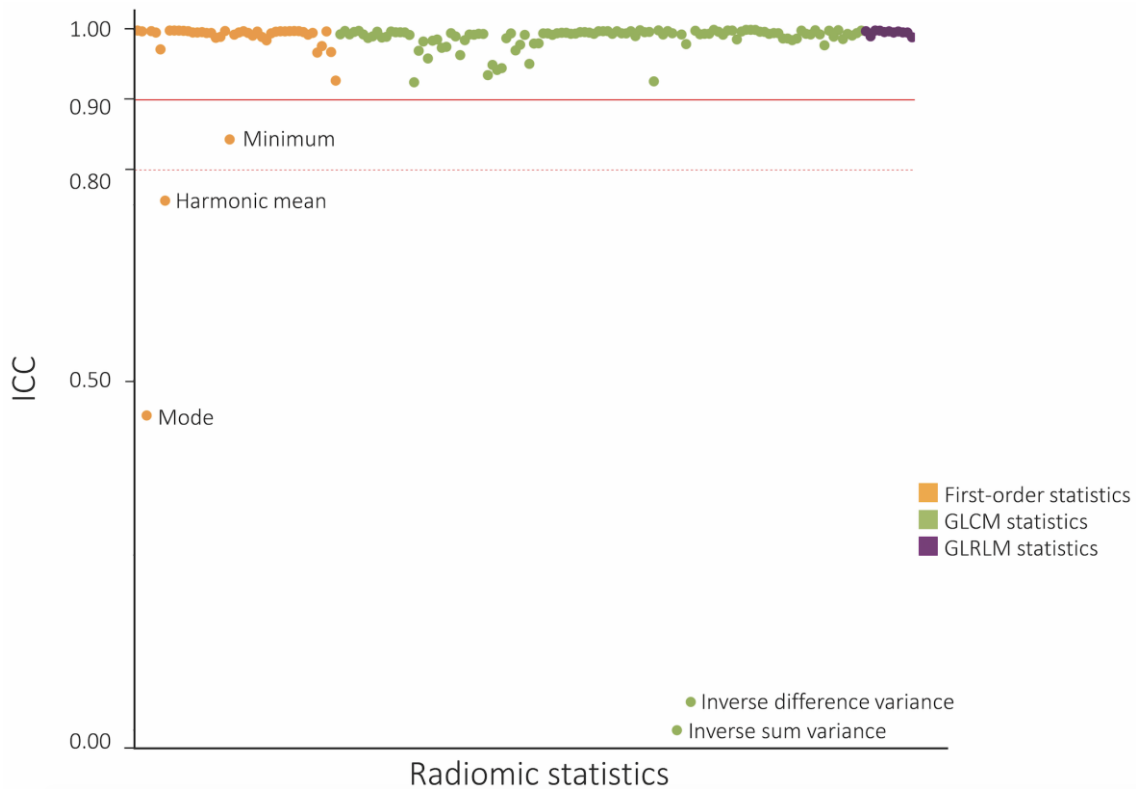


**Figure 19.** Manhattan plot of ICC values of radiomic parameters (164).

Radiomic parameters are lined up on the x axis, while their corresponding ICC value is plotted on the y axis.

GLCM: grey level co-occurrence matrix; GLRLM: grey level run length matrix; ICC: intraclass correlation coefficient

Linear regression analysis showed that the type of binning i.e equal sized or equally probable binning, was a significant predictor of radiomic values for 90% (103/114) of all GLCM parameters. Among GLCM parameters  $\Delta R^2$  values attributable to the type of binning were smaller than 0.25 in 87% (99/114) of the radiomic parameters. 3% (3/114) had  $\Delta R^2$  changes between 0.25 and 0.49, and 2% (2/114) had changes between 0.50 and 0.75. Even though all GLRLM parameters were significantly affected by binning type ( $p < 0.05$ , all), the  $\Delta R^2$  attributable to adding binning type to the regression model only minimally changed the  $R^2$  values ( $\Delta R^2 < 0.04$  for all). Results are summarized in figure 20.

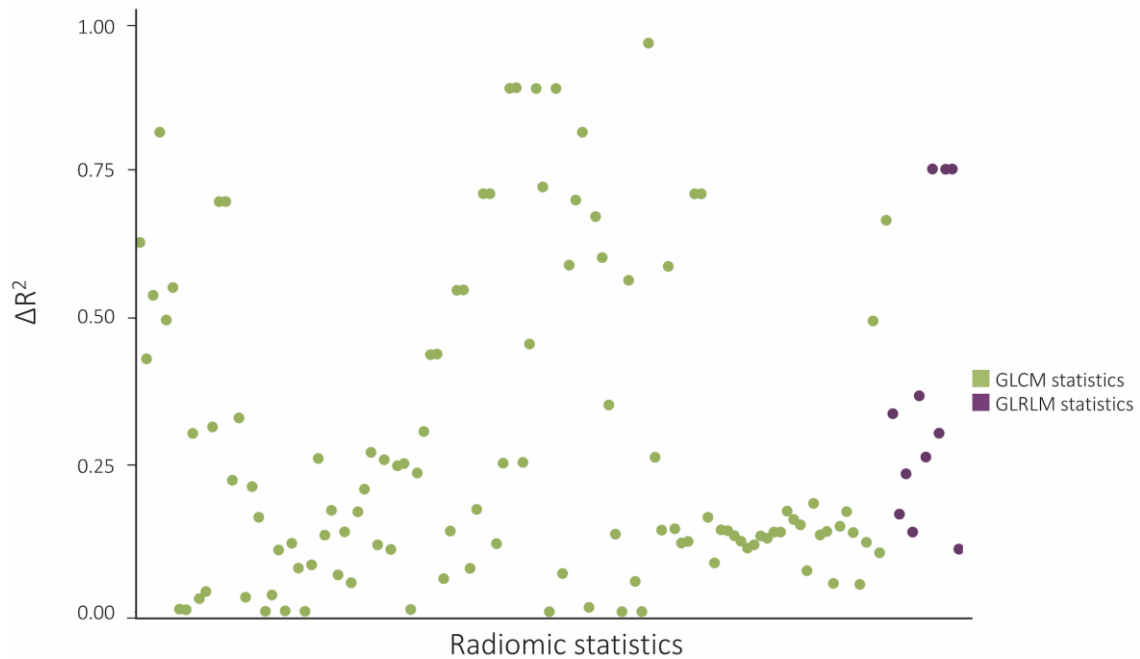


**Figure 20.** Manhattan plot of  $\Delta R^2$  values when the type of binning was added to the regression model (164).

Radiomic parameters are lined up on the x axis, while the corresponding  $\Delta R^2$  values are plotted on the y axis.

GLCM: grey level co-occurrence matrix; GLRLM: grey level run length matrix

The number of bins to which HU values were discretized before the calculation of radiomic parameters, significantly affected the values for all GLCM and GLRLM parameters. Among GLCM, 61% (70/114) of the parameters had a  $\Delta R^2 < 0.25$  if the number of bins was added to the model. 16% (18/114) produced  $\Delta R^2$  between 0.25 and 0.49, 17% (19/114) between 0.50-0.74 and 6% (7/114) of all parameters had  $R^2$  change values greater than 0.75. Regarding GLRLM parameters, 4 parameters'  $\Delta R^2$  was less than 0.25 when the number of bins was added to the regression model. 4 statistics produced  $R^2$  changes between 0.25 and 0.49, while in case of 3 parameters the  $\Delta R^2$  was more than 0.75. Results are summarized in *figure 21*.

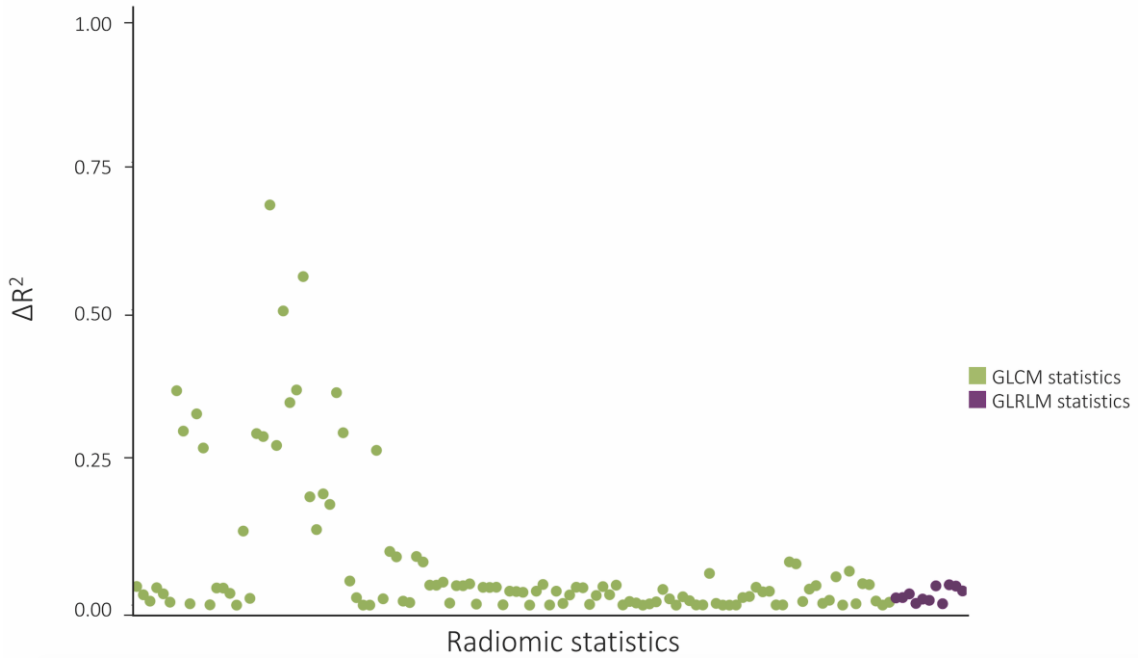


**Figure 21.** *Manhattan plot of  $\Delta R^2$  changes when the number of bins used for discretization was added to the regression model (164).* Radiomic parameters are lined up on the x axis, while the corresponding  $\Delta R^2$  values are plotted on the y axis. GLCM: grey level co-occurrence matrix; GLRLM: grey level run length matrix

#### **4.5. Identification of advanced atherosclerotic images using radiomics-based machine learning validated using histology**

The demographic characteristics of donor patients (mean age  $52\pm 5.3$  years, 7/7 [100%] male gender), are summarized in *table 10*.

Overall, 611 histological sections from 21 coronary arteries of 7 donor hearts were investigated. Average studied vessel length was 67 mm (range 25 to 110 mm). Of the 611 sections, 71/611 (11.6%) were identified as adaptive intimal thickening, 222/611 (36.3%) as pathological intimal thickening, 179/611 (29.3%) as fibrous plaque, 59/611 (9.7%) as early fibroatheroma, 60/611 (9.8%) as late fibroatheroma, and 20/611 (3.3%) contained TCFA. Out of all cross-sections 477/611 (78.1%) contained plaque that was detectable on CTA. Of these, non-calcified plaque was present in 254/477 (53.2%), partially calcified in 191/477 (40.0%), and calcified plaque in 32/477 (6.8%) cross-sections. Since plaque attenuation pattern-based classification is based on non-calcified plaque components, all analyses were performed by excluding cross-sections containing purely calcified lesions. Therefore, overall 445 cross-sections were analyzed.

The dataset was randomly split into a training-set (75%, 333/445) and a validation-set (25%, 112/445). There was no difference between the training-set and validation-set regarding the distribution of early or advanced atherosclerotic lesion categories, and plaque types based either on traditional CTA classification scheme or plaque attenuation classification scheme (early atherosclerotic lesions:  $p=0.90$ ; advanced atherosclerotic lesions  $p=0.71$ ; traditional plaque classification  $p=0.26$ ; plaque attenuation pattern  $p=0.41$ ). Detailed distribution of histological and CTA categories of analyzed plaques can be found in *table 11*.

**Table 10.** Patient characteristics. BMI: body mass index; HLP: hyperlipidemia; HTN: hypertension; MI: myocardial infarction (169).

Case #	Variables											
	Age	Gender	BMI	Previous MI	Stent	HTN	HLP	Diabetes	Tobacco	Drug use	Cause of Death	Race/Ethnicity
1	53	Male	21.6	No	No	No	No	No	Yes	No	ICH/Stroke	Caucasian
2	53	Male	29.2	No	No	Yes	No	Yes	Yes	No	Gunshot	Caucasian
3	53	Male	24.0	No	No	Yes	Yes	Yes	No	No	ICH/Stroke	African American
4	44	Male	32.4	No	No	Yes	Yes	No	Yes	Yes	ICH/Stroke	African American
5	54	Male	25.4	No	No	Yes	Yes	No	Yes	Yes	ICH/Stroke	Caucasian
6	61	Male	26.3	Yes	Yes	Yes	No	No	Yes	No	ICH/Stroke	Caucasian
7	48	Male	28.2	Yes	Yes	Yes	No	No	Yes	No	ICH/Stroke	Caucasian

**Table 11.** Distribution of histological, traditional and plaque attenuation-based CTA categories of analyzed cross-sections (169).

<b>Classification categories</b>	All cross-sections N=445	Training-set N=333	Validation-set N=112	p
<b>Histological categories</b>				
<i>Early atherosclerotic lesions n (%)</i>	311 (69.9)	230 (69.1)	81 (72.3)	0.90
Adaptive intimal thickening n (%)	12 (2.7)	9 (2.7)	3 (2.7)	
Pathological intimal thickening n (%)	194 (43.6)	145 (43.5)	49 (43.7)	
Fibrous plaque n (%)	105 (23.6)	76 (22.8)	29 (25.9)	
<i>Advanced atherosclerotic lesions n (%)</i>	134 (30.1)	103 (30.9)	31 (27.7)	0.71
Early fibroatheroma n (%)	58 (13.0)	45 (13.5)	13 (11.6)	
Late fibroatheroma n (%)	58 (13.0)	43 (13.0)	15 (13.4)	
Thin-cap fibroatheroma n (%)	18 (4.1)	15 (4.5)	3 (2.7)	
<b>CT angiography categories</b>				
<i>Traditional scheme</i>				0.26
Non-calcified plaque n (%)	254 (57.1)	185 (55.6)	69 (61.6)	
Partially calcified plaque n (%)	191 (42.9)	148 (44.4)	43 (38.4)	
<i>Plaque attenuation scheme</i>				0.41
Homogeneous n (%)	207 (46.5)	152 (45.6)	55 (49.1)	
Heterogeneous n (%)	200 (44.9)	155 (46.5)	45 (40.2)	
Napkin-ring sign n (%)	38 (8.6)	26 (7.9)	12 (10.7)	

Non-calcified and partially calcified plaques showed similar frequencies between early and advanced atherosclerotic lesions in case of all cross-sections ( $p=0.08$ ). On the other hand, the distribution of CTA cross-sections showing homogeneous, heterogeneous and napkin-ring sign attenuation patterns differed between early and advanced atherosclerotic lesions ( $p<0.001$ ). Detailed results can be found in *table 12*.

**Table 12.** Frequency of traditional and plaque attenuation-based CTA categories for early and advanced atherosclerotic lesions for all cross-sections (169).

CTangiography classification categories	Early	Advanced	P value
	atherosclerotic lesions N=331	atherosclerotic lesions N=134	
<b>Traditional scheme</b>			
Non-calcified plaque n (%)	186 (56.2)	68 (50.7)	0.08
Partially calcified plaque n (%)	125 (43.8)	66 (49.3)	
<b>Plaque attenuation scheme</b>			
Homogeneous n (%)	166 (53.4)	41 (30.6)	<0.001
Heterogeneous n (%)	140 (45.0)	60 (44.8)	
Napkin-ring sign n (%)	5 (1.6)	33 (24.6)	

Among radiomics-based ML models, the least angles regression model provided the best discriminatory power on the training-set. Diagnostic accuracies of the radiomics-based ML models on the training-set can be found in *table 13*. The following hyperparameters for the processing pipeline produced the best results on the training-set using the least angles regression model. First, we excluded all zero variance parameters and scaled the parameters based on median and interquartile ranges. Next the best predictors based on the training-set were selected using significance levels alpha of 0.05 and 0.0007 for the family-wise error rate and false positive rate test, respectively. Then we conducted principal component analysis to construct derived parameters explaining the 95% of the variation in the data. Afterwards, 13 parameters were selected to be inputs to the least angle regression model. This fitted model was then applied to the validation-set to evaluate the unbiased discriminatory power of the model.

**Table 13.** Discriminatory power of radiomics-based ML models on the training-set to identify advanced atherosclerotic lesions (169).

<b>Radiomics-based machine learning models</b>	<b>Area Under the Curve</b>
Least angles regression	0.673
Logistic regression	0.669
Random Forests	0.666
Naïve Bayes	0.645
Gaussian processes classifier	0.640
K-nearest neighbors	0.635
Deep neural network	0.631
Decision trees	0.500

The radiomics-based ML model achieved good diagnostic accuracy (AUC=0.73, CI: 0.63-0.84) on the validation-set. The plaque attenuation pattern scheme achieved moderate diagnostic accuracy, AUC=0.65, CI: 0.56-0.73, while histogram-based measurements: area of low attenuation (<30 HU) and the average HU values of the plaque cross-sections produced poor diagnostic accuracy (AUC=0.55, CI: 0.42-0.68, AUC=0.53, CI: 0.42-0.65; respectively) on the validation-set. The radiomics-based ML model outperformed expert visual assessment (AUC=0.73 vs. 0.65; p=0.04) and also histogram-based measurements, such as area of low attenuation (<30 HU) (AUC=0.73 vs. 0.55, p=0.01) and the average HU values of the plaque cross-sections (AUC=0.73 vs. 0.53, p=0.004). ROC curves of the corresponding models evaluated on the validation-set are shown in *figure 22*.

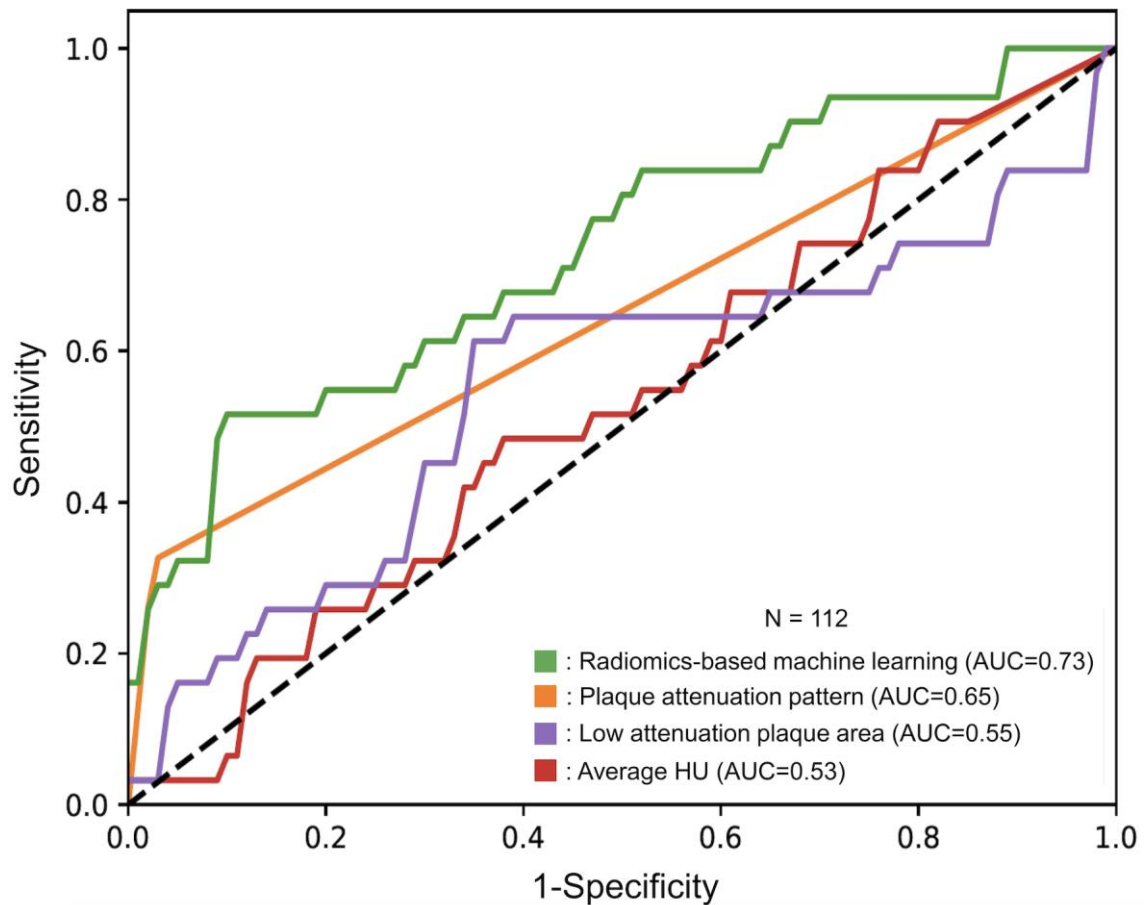


**Figure 22.** Receiver operating characteristics curves of radiomics-based machine learning model, plaque attenuation pattern, area of low attenuation and average HU value to identify advanced atherosclerotic lesions (169).

Area under the ROC curve showed the best discriminatory power for radiomics-based machine learning method (AUC=0.73, CI: 0.63-0.84) to identify advanced atherosclerotic lesions. Visual assessment using plaque attenuation pattern was worse (AUC=0.65, CI: 0.56-0.73;  $p = 0.04$ ), while histogram-based methods: area of low attenuation and average HU value showed poor diagnostic accuracy and were lower as compared to the radiomics-based machine learning model (AUC=0.55, CI: 0.42-0.68; AUC=0.53, CI: 0.42-0.65;  $p=0.01$  and  $p=0.004$ ).

AUC: area under the curve; HU: Hounsfield unit

## 5. DISCUSSION

### 5.1. Coronary CTA for the characterization of plaque burden

Butler et al. reported even larger differences when analyzing the results of 37 patients who underwent both imaging modalities (16). In their patient population, even larger differences were observed between modalities (CTA: 67%; ICA: 24%), which resulted in higher percentage of segments only seen stenotic on CTA (57%). To assess the clinical significance of discrepancy in the number of stenotic segments seen by CTA and ICA, we classified patients as proposed by Bittencourt et al (133). In 78% of reclassified individuals, reclassification was solely caused by CTA classifying the patients as extensive as compared to ICA, which classified them as non-extensive, while in 22% it was caused by CTA overrating the degree of obstruction. One patient who changed to lower risk category was due to the fact that CTA underestimated the degree of stenosis. Bittencourt et al. calculated hazard ratios associated with the patient categories: extensive obstructive: 3.9, extensive non-obstructive: 3.1, non-extensive obstructive: 3.0, whereas non-extensive non-obstructive did not show any association with any increase in rate of cardiovascular death or myocardial infarction. Using hazard ratio values of the risk groups, average hazard ratio of ICA-based measurements was lower than CTA-based calculations (2.7 vs. 3.3, respectively).

Current identification of patients prone to MACE is based on anthropometric and blood test information. In recent years with the development of imaging modalities, significant efforts have been channeled into finding morphological features unique to vulnerable plaques. This paradigm shift from risk factors to lesion-based phenotypic risk assessment showed promising results, but longitudinal studies question the predictive value of a single high-risk plaque at a given time point (57). Kubo et al. demonstrated using intravascular ultrasound-virtual histology that 75% of vulnerable plaques lost high-risk characteristics by thickening of the fibrous cap, or by transforming to fibrotic plaques (170). Only 25% showed vulnerable characteristics after 12-month follow-up. It seems identification of vulnerable patients is more than identifying high-risk plaques.

ICA is accepted as the reference standard of stenosis quantification in daily clinical practice. While the coronary lumen is depicted with high temporal and spatial resolution, the coronary wall is imperceptible with ICA, therefore the identification plaques that

cause minimal and mild stenosis is challenging. On the other hand, coronary CTA is capable of visualizing not only the lumen but also the coronary wall and atherosclerotic plaques. It has a high diagnostic accuracy to identify obstructive lesions, however it has a tendency to overestimate stenosis severity (14). Due to the high CT attenuation values of calcium, coronary CTA shows a superior sensitivity to identify calcified plaques. The identification of non-calcified plaque is more challenging, and it requires excellent image quality.

The COronary CT Angiography EvaluationN For Clinical Outcomes: An InteRnational Multicenter registry demonstrated the importance of the presence of mild and minor plaques, as the hazard ratio increases by 1.22 for each segment with any plaque (48). Thus, differences in the number of diseased segments observed by different imaging techniques can have a major impact on risk assessment. Hence, ICA and coronary CTA are not interchangeable. ICA is superb at detecting obstructive coronary disease but is inferior to CTA in plaque detection. Therefore, ICA might underestimate patient risk due to the insufficient recognition of non-obstructive plaques.

Generalization of our results has limitations. Our study population was fairly small, though larger than recent publications. Obstructive and extensive CAD was overrepresented in our study compared to the general population, which might overestimate the number of reclassified patients.

## **5.2. Potential of radiomics to identify napkin-ring sign plaques**

Radiomics utilizes voxel values and their relationship to each other to quantify image characteristics. Based on our results it seems not only do radiomic features outperform conventional quantitative imaging markers, but parameters incorporating the spatial distribution of voxels (GLCM, GLRLM and geometry-based parameters) have a better predictive value than first-order statistics, which describe the statistical distribution of the intensity values. Among GCLM parameters the interquartile range, the lower notch, the median absolute deviation from the mean of the GLCM probability distribution, Gauss right focus and sum energy had the five highest AUC values. NRS plaques have many low value voxels next to each other in a group surrounded by higher density voxels. This heterogeneous morphology results in an unbalanced GLCM and therefore higher interquartile rank values, which also means smaller lower notch values and bigger deviations from the mean. Gauss right focus and sum energy both give higher weights to elements in the lower right of the GLCM, which represents the probability of high-density voxels occurring next to each other. Since NRS plaques do not have many high value voxels next to each other, they received smaller values, while non-NRS plaques have higher values, which resulted in excellent diagnostic accuracy.

Among GLRLM statistics, long and short run low gray level emphasis, long and short run emphasis and run percentage had the best predictive value. Run percentage and long run emphasis gives high values to lesions, where there are many similar value voxels in one direction, while long run low gray level emphasis adds a weight to the previous parameter by giving higher weights when these voxel runs contain low HU values. NRS plaques' low-density core has many low CT number voxels next to each other in one direction, therefore NRS plaques have higher values as compared to non-NRS plaques, which results in excellent diagnostic accuracy. In case of short run emphasis and short run low gray level emphasis the contrary is true, which results in NRS plaques receiving low values, while non-NRS plaque have higher values also leading to high AUC values. Among geometry-based parameters, the first five with the best diagnostic accuracy all represent the surface ratio of a specific subcomponent to the whole surface of the plaque. In all cases the ratio of high-density subcomponents (for example: subcomponent 2 when the plaque was divided into two components) to the whole surface had excellent diagnostic accuracy. Since each subcomponent is composed of equal number of voxels

due to the equally probable binning, the difference in surfaces is a result of how the high intensity voxels are situated to each other. In case of NRS plaques extraction of low attenuation voxels leaves a hollow cylindrical shape of high CT number voxels which has a relatively large surface. Non-NRS plaques on the other hand do not have such voxel complexes, therefore the surface of the high attenuation voxels is smaller and therefore the ratio compared to the whole surface is also smaller.

This kind of transition from qualitative to quantitative image assessment was initiated by oncoradiology. As studies showed that morphological descriptors correlate with later outcomes, reporting guidelines such as the Breast Imaging Reporting and Data System (BI-RADS) started implementing qualitative morphological characteristics into clinical practice (171, 172). However, despite all the efforts of standardization, the variability of image assessment based on human interpretation is still substantial (173). Radiomics, the process of extracting thousands of different morphological descriptors from medical images, has been shown to reach the diagnostic accuracy of clinical experts in identifying malignant lesions (28). Furthermore, radiomics can not only classify abnormalities to proper clinical categories, but can also discriminate between responders and non-responders to clinical therapy and can predict long-term outcomes (31, 34). However, there are major concerns on the generalizability of radiomics. Several studies have shown, that imaging parameters, reconstruction settings, segmentation algorithms, etc. all effect the radiomic signature of lesions (174-177). Furthermore, it has been shown that the variability caused by these changeable parameters is in the range or even greater than the variability of radiomic features of tumor lesions (178). Very little is known about cardiovascular radiomics. Several studies will be needed to replicate these results in the cardiovascular domain. The potential of radiomics is extensive, however the problem of standardized imaging protocols and radiomic analysis need to be solved to achieve robust and generalizable results.

Despite our encouraging results, our study has some limitations which should be acknowledged. All of our examinations were done using the same scanner and reconstruction settings. It is yet unknown how these settings might affect radiomic parameters and therefore influence the applicability of radiomics in daily clinical care. Furthermore, our results are based on a case-control study design. The true prevalence of the NRS is considerably smaller as compared to non-NRS plaques in a real population.

Therefore, our observed positive predictive values might be higher, while our negative predictive values might be smaller than expected in a real-world setting. Moreover, our limited sample sizes might not allow the accurate assessment of the diagnostic accuracy of the different parameters. However, we performed Monte Carlo simulations and cross-validated our results to achieve robust estimates.

### **5.3. Possibility to identify radionuclide and invasive imaging markers using non-invasive coronary CTA**

It seems that by utilizing radiomics, the amount of information accessible in CT images can be greatly increased. Radiological examinations are evaluated mostly by visual inspection in current clinical care. As opposed to this practice, in the current project we treated radiological images as 3-dimensional datasets and extracted hundreds of quantitative parameters from coronary plaques. This strategy resulted in significantly better discriminatory power to identify invasive and radionuclide markers of plaque vulnerability. Radiomics utilizes texture and geometrical analysis to derive novel imaging biomarkers. By measuring how many times a given value voxel pairs occur next to each other, or how many times similar values occur next to each other in a given direction, probability matrices can be calculated which resemble the spatial distribution of the voxel values. The analysis of these matrices leads to new imaging biomarkers, such as heterogeneity, contrast or spatial fragmentation. Based on our results it seems that these parameters have a better discriminative capability to identify invasive and radionuclide markers of plaque vulnerability than visual inspection and conventional quantitative assessment.

Coronary CTA for many years was regarded as a rule-out test for obstructive coronary artery disease due to its excellent negative predictive value (179, 180). However, its unique ability to noninvasively image atherosclerotic lesions holds great potential to identify high-risk plaques. With the newest guidelines promoting coronary CTA as the first-line test in the management of patients with stable chest pain, the number of examinations will further increase. Therefore, the next challenge will be to correctly identify high-risk lesions to improve patient risk assessment. Invasive and radionuclide imaging techniques can identify high-risk lesions; however, their invasive nature and their costs preclude the use of these techniques in daily routine. While CT might not have sufficient spatial resolution, its capability to acquire isotropic 3-dimensional data non-invasively creates a unique opportunity to analyse complex spatial image patterns using radiomics.

Invasive imaging modalities with sub-millimetre spatial resolution allow the morphological assessment of coronary plaques. Specific IVUS and OCT imaging markers

have been linked to histology and patient outcomes. Our results are in line with previous findings that conventional assessment of coronary CTA only allows identification of invasive imaging markers of plaque vulnerability with moderate accuracy (158). However, in the current study we showed that radiomic features significantly outperformed conventional metrics, therefore potentially allowing the non-invasive identification of invasive imaging markers plaque vulnerability.

For both IVUS-attenuated plaque and OCT-TCFA fractal box counting dimension of high attenuation voxels had the highest AUC values. Attenuated plaques based on IVUS are resembled by a hypoechoic plaque area with low ultrasound attenuation indicating the presence of lipids. TCFA-s identified using OCT have a similar spatial pattern, however the superior spatial resolution of OCT allows the assessment of fibrous-cap thickness, therefore allowing the identification of TCFA. While the spatial resolution of state-of-the-art coronary CTA-s preclude the identification of the fibrous-cap, the large lipid pools of these lesions have low CT attenuation. As the low attenuation voxels of the lipid pools are situated in the central portion of the plaque, next to each other, the remaining higher attenuation voxels (relative to other voxel values in the plaque, but not necessarily representing calcification) are limited in number and occupy limited space. On the other hand, plaques that do not exhibit large lipid pools have more high attenuation voxels, which can occupy any position inside the plaque in a complex spatial pattern, which can be described using fractal dimensions. Fractal dimensions quantify the spatial complexity of structures. Fractal dimensions are calculated by magnifying the image and assessing how many voxels the given abnormality occupies in relation to the degree of zoom (24). In case of plaques with large lipid pool, the high attenuation voxels are relatively few in number and have limited space to occupy. Therefore, these plaques have low value of fractal box counting dimension of high attenuation voxels. On the other hand, stable plaques, which do not restrict the spatial distribution of high attenuation voxels have higher values for this radiomic parameter. These characteristics might explain that the fractal box counting dimension of high attenuation voxels resulted a good discriminatory power to identify invasive markers of plaque vulnerability.

Even though coronary CTA is an anatomical imaging modality, it seems that radiomics can identify plaques with inflammation and micro-calcifications identified using NaF<sup>18</sup>-PET (AUC=0.87), both of which are currently regarded as undetectable using coronary

CTA. Visual assessment might not be sufficient to distinguish these features. However, it was recently demonstrated that by using simple quantitative metrics it is indeed possible to quantify vascular inflammation using CT, which previously was thought impossible (181). Importantly microscopic calcium formations are too small to be identified using conventional CTA techniques. However, it seems that radiomics can identify unique spatial patterns specific for sodium-fluoride uptake. Among the calculated radiomics parameters the surface of high attenuation voxels (relative to other voxel values in the plaque, but not necessarily voxel values above the calcification threshold) had the highest AUC value to identify increased radionuclide uptake. Even though the spatial resolution of CTA images precludes the identification of microcalcifications, voxels containing microcalcifications may have higher HU values. Furthermore, these high CT number voxels have large surfaces, since they are not grouped in one cluster as opposed to calcified plaques, which also contain high attenuation voxels but overall have smaller surfaces since the voxels are next to each other. These characteristics may have resulted in the excellent diagnostic accuracy of surface of high attenuation voxels to identify increased radionuclide uptake. As there are no plaques showing both invasive and radionuclide imaging markers of plaque vulnerability, the capability of coronary CTA radiomics to identify NaF<sup>18</sup>-positiv is independent of its ability to identify morphologic vulnerability.

A limitation of our study is the relatively small sample size, which might lead to overly optimistic diagnostic results. However, considering that four different imaging techniques were utilized in all patients, we believe that our patient cohort is unique, and the sample size is reasonable. To compensate for the limited sample size, we calculated all diagnostic scores using a 5-fold cross validation with 1000 repeats. This technique explicitly simulates the population's AUC value of each parameter and provides a robust estimate of diagnostic accuracy. Furthermore, our results are based on a single centre study setting where the results were analysed in a core-lab. Therefore, the application of our results to general populations is limited as studies have shown that image acquisition, reconstruction and analysis may have a significant effect on the reproducibility of radiomic features (174, 182, 164, 183). However, further investigations are necessary for radiomics to be applicable to clinical care. Larger sample size prospective studies are needed, where the number of patients would allow to build multi-parametric machine

learning models, which could robustly identify imaging markers of plaque vulnerability. Furthermore, multi-centre longitudinal studies are warranted to assess the prognostic value of radiomic image markers.

#### **5.4. Robustness of volumetric and radiomic features to image reconstruction algorithms**

Applicability of a new diagnostic technique not only depends on its potential to identify pathologies, but also on its robustness to different clinical and technical settings. In recent years iterative reconstruction algorithms became standard in clinical care as they allow significant reduction of radiation dose without significant compromise in image quality (184). While the quality of radiological images has improved through the reduction of noise, concerns have been raised as to whether the novel reconstruction techniques have any effect on quantitative image analysis. Calcium-score, one of the earliest quantitative CT metrics has been shown to significantly change with new iterative reconstruction techniques, which also has impact on patients' cardiovascular risk assessment (185-187). However interestingly, quantitative plaque volumes seem to be less affected (188, 189). Differences can be more attributable to the accuracy of automatic segmentation algorithms rather than the voxel values themselves (146). Our research methodology of using one segmentation on all three image reconstructions ensures that only the effect of the reconstruction algorithms is investigated regardless of the image segmentation. Our results confirm that volumetric plaque analysis has excellent reproducibility with respect to the different image reconstructions. However, there is little information as to whether radiomic parameters are affected by image reconstruction.

As radiomics has proven to help grade malignancies, classify lesions into histological categories and predict patient outcomes, more and more attention is drawn to the reproducibility of such findings (190-193). Altazi and colleagues has shown, that positron emission tomography (PET) based radiomic features using different reconstructions show variation regarding reproducibility (174). Among 79 investigated features only inverse difference and inverse difference momentum showed ICC values  $>0.90$ . Similarly, Shiri et al. investigated the effect of different PET reconstruction settings (177). Among 100 different radiomic parameters, only 47 had very small variation. Interestingly, in our dataset only 3% of parameters had values below 0.90. Based on our results, CT based radiomic parameters seem to be more robust to different reconstructions as compared to PET. Our findings imply that new iterative reconstruction techniques can be used interchangeably, as they have minimal effect on calculated metrics. Therefore, new

knowledge gained from radiomic studies can be applied across different reconstruction algorithms. Furthermore, previous images can also be used to increase radiological registries, as inferences gained from previous images reconstructed using FBP will result in similar results as if they would have been reconstructed using novel HIR or MIR techniques.

Even though radiomic statistics seem to be robust to reconstruction algorithms, the type of voxel binning and the number of bins used for discretization have a significant effect on the statistical values. Similar results have been reported when assessing the impact of different number of gray level discretizations on PET images (174, 183). Only two GLCM and GLRLM parameters were found to be highly reproducible. In our dataset all parameters were significantly affected by the number of bins. Furthermore, in 41% (51/125) of the examined parameters, more than 25% of the radiomic metrics' variation could be attributed to changes in the number of bins used for calculation of the parameters. In addition, we found that 90% of GLCM parameters and 100% of GLRLM parameters were also affected by the way the binning was performed. However, only in case of 5 parameters could the type of binning explain more than 25% of the parameters' variation. Our results emphasize the need for standardization of radiomic analysis, as differences in calculation of the metrics can cause significant changes in the radiomic statistics. Furthermore, precise reporting of all parameter setting used for radiomic calculations is needed to achieve reproducible results. However, these findings do not mean, that radiomic statistics are unreliable due to the significant influence of parameter settings used for calculations. Rather they highlight the fact that each radiomic statistic can be calculated in many different ways which can lead to very different results, which urges standardization of radiomics.

Our study has some limitations. There were only a limited number of plaques analyzed (n=60) and only excellent image quality scans were selected retrospectively, which might cause a selection bias and decrease the generalizability of our results. The reconstruction algorithms used are specific to the vendor, therefore using other manufacture's algorithms might lead to different results. Furthermore, both HIR and MIR have different levels of possible iterations. We limited our analysis to mid-range levels in both cases (iDOSE<sup>4</sup> level 4; IMR level 2), as they are most commonly used in everyday practice. However, using different iteration levels would might lead to different results.

## **5.5. Potential of radiomics-based machine learning to classify coronary lesions to corresponding histology categories**

Large necrotic cores of advanced atherosclerotic lesions carry an inherently higher risk of plaque rupture, therefore the identification of these lesions is of utmost importance (38). Coronary CTA would be an ideal imaging modality to identify these advanced lesions, due to its non-invasive nature and wide-spread availability. Previously, it has been shown that the plaque attenuation pattern-based scheme outperforms conventional classification to identify advanced atherosclerotic lesions (AUC: 0.76 vs. 0.68;  $p=0.001$ ) (54). However, the previous investigation assessed the diagnostic accuracy on the whole dataset, therefore, those results were overly optimistic and preclude the generalization of the results to other populations. In addition, the reproducibility of qualitative imaging markers is poor even among experienced readers, therefore the generalizability of results based on visual assessment is limited (112). More objective methods with less reliance on reader experience are warranted.

To overcome the limitations of visual assessment and to provide a more objective method to characterize atherosclerotic plaques, quantitative histogram-based methods based on HU measurements have been proposed (79, 194, 195). Previous results show a good correlation between quantified low-attenuation plaque volume or area and the presence of large lipid cores (67, 196, 195). However, it is not only the presence of lipid rich plaque components that defines advanced atherosclerotic lesions but also the spatial distribution of various tissue components (54). In addition, these methods are limited by the fact that different tissue components may have overlapping HU values (67).

Radiomics has been shown to identify napkin-ring sign plaques with excellent diagnostic accuracy (135). Furthermore, ML has proven to be a valuable tool in medical data analysis (197, 198), identifying insights from big data databases using alternative statistical techniques. Instead of using probability theory as conventional statistical methods, these procedures are based on methods originating from how we learn and perceive our surroundings (199). It seems that ML is helpful in medical image analysis too as our results indicate that applying ML to radiomic features from coronary CTA images outperforms current methods. While our AUC values may appear to some as limited, would like to emphasize that based on recent data demonstrating that local plaque

composition has low positive predictive value to identify locations of future plaque rupture leading to myocardial infarction (200), our radiomics marker may be used as an additional tool to refine risk stratification and to tailor medical therapy. For this purpose, our AUC values appear to acceptable and useful.

Our study has limitations. Our results are based on coronary CTA images acquired from a motion-free ideal environment, therefore the translation of our results to in vivo environments might be limited. Furthermore, despite the relatively large number of cross-sections, our analysis is based on only seven hearts. Furthermore, the training-set and validation-set consisted of cross-sections from the same individuals, which might have biased our results. However, we choose to randomly select our validation dataset on a per cross-section basis, rather than at an individual level, since selecting only one or two cases hearts for validation might not well represent the general population. Furthermore, to overcome overfitting of our models, we evaluated diagnostic performance on a separate validation-set. Moreover, the overall number of advanced atherosclerotic lesions and especially TDFAs was small in our dataset, but this is representative of general populations. In addition, we did not analyze purely calcified plaques since the partial volume effect of the calcium prohibits analysis of soft tissue components and therefore our results are not generalizable to all plaque types. Furthermore, our radiomics results are based on images from one scanner, reconstruction and filter setting, therefore generalizability of the results beyond these setting is unknown. Finally, manual segmentation was a prerequisite for the generation of regions of interests which served as the input for histogram and radiomics models.

## 6. CONCLUSIONS

Based on our study, ICA sees only half as many segments with plaque and underestimates plaque sizes compared with CTA in patients with moderate, mild and minimal plaques. These differences might have a significance in patient risk stratification and patient management.

We demonstrated that coronary plaques consist of sufficient number of voxels to conduct radiomic analysis, and a substantial portion of radiomic parameters showed a significant difference between plaques with or without NRS, while conventional parameters did not show any difference. Furthermore, several radiomic parameters had a higher diagnostic accuracy in identifying NRS plaques than conventional quantitative measures. Cluster analysis revealed that many of these parameters are correlated with each other, however there are several distinct clusters, which imply the presence of various features that hold unique information regarding plaque morphology. Cross-validation simulations indicate, that our results are robust when assessing the discriminatory value of radiomic parameters, implying the generalizability of our results. Radiomics is a promising new tool to identify qualitative plaque features such as the NRS. As the number of CT examinations increases, we are in dire need of new techniques which increase the accuracy of our examinations without increasing the workload of imaging specialists. Our findings indicate that radiomics can quantitatively describe qualitative plaque morphologies and therefore has the potential to decrease intra- and inter-observer variability by objectifying plaque assessment. In addition, we observed several different clusters of information present in our dataset, implying that radiomics might be able to identify new image markers that are currently unknown. These new radiomic characteristics might provide a more accurate plaque risk-stratification than the currently used high-risk plaque features. Radiomics could easily be implemented into currently used standard clinical workstations and become a computer-aided diagnostic tool, which seamlessly integrates into the clinical workflow and could increase the reproducibility and the accuracy of diagnostic image interpretation in the future.

We demonstrated that radiomics can increase the diagnostic accuracy of coronary CTA to identify specific invasive and radionuclide imaging markers of plaque vulnerability. Coronary CTA radiomics showed a good diagnostic accuracy to identify IVUS-

attenuated plaques and excellent diagnostic accuracy to identify OCT-TCFA and NaF<sup>18</sup>-positivity. Furthermore, radiomics outperformed conventional CT metrics to identify these invasive and radionuclide imaging markers. Our results suggest that radiomics may be able to identify invasive and radionuclide imaging markers of plaque vulnerability with good to excellent diagnostic accuracy. It seems that there is minimal overlap between anatomical vulnerability features of invasive imaging modalities and NaF<sup>18</sup>-positivity, which is also reflected by our findings that different radiomic parameters were predictive for these features. Advanced texture analysis of CT images holds magnitudes more information than currently perceivable by clinical visual assessment. These CT radiomic information may allow to identify invasive and radionuclide imaging markers from conventional CT images. Identification of these vulnerability markers by a single, widely available non-invasive technique may provide an opportunity to identify vulnerable plaques and vulnerable patients in broad populations without invasive procedures or costly radionuclide tests. Further studies are warranted to assess the true potential of radiomics to aid precision phenotyping of coronary disease.

Our results show that both volumetric and radiomic parameters have excellent reproducibility with regards to different image reconstructions indicating that quantitative plaque analysis can be confidently performed on any kind of image reconstruction. However, the type of binning and the number of bins used significantly affects radiomic parameters, therefore reporting the type of binning and number of bins used for radiomic analysis is needed. Furthermore, this emphasizes the need for standardization of radiomic analyses to achieve reproducible results and for radiomics to translate into everyday clinical practice. All volumetric and the majority of radiomic parameters are unchanged using different image reconstruction algorithms. However, radiomic features are significantly affected by how the discretization of HU values was done before calculation and therefore, precise reporting of used methods is needed. Our results emphasize the need of standardization of radiomic analysis to achieve robust reproducible results which can be implemented into everyday clinical practice.

From seven ex vivo hearts we trained a radiomics-based machine learning on a separate training-set of coronary CTA images to identify advanced atherosclerotic lesions. Evaluating our results on a separate validation-set our results indicate radiomics-based machine learning can better differentiate between early vs. advanced atherosclerotic

lesions as compared to the plaque attenuation pattern scheme in CTA cross-sections, histogram-based measurements: area of low attenuation and average Hounsfield unit values of the plaque cross-sections. Our results show that radiomics-based machine learning was able to outperform expert visual assessment and histogram-based methods to identify advanced atherosclerotic lesions. Despite the limited spatial resolution of coronary CT angiography, implementing machine learning to radiomic features can improve the diagnostic accuracy of coronary CTA to identify high-risk atherosclerotic lesions and therefore could help risk stratification of patients.

## 7. SUMMARY

Coronary CTA has emerged as the first line of choice for the evaluation of CAD in stable patients. Based-on our results it seems, coronary CTA is superior to ICA to describe the overall amount of CAD in these patients, and therefore may provide a more accurate method for risk stratification. Furthermore, coronary CTA provides imaging of not only the luminal stenosis, but the atherosclerotic disease itself. This provides a unique opportunity to apply advanced image analysis such as radiomics to precision phenotype CAD.

Radiomic analysis of coronary plaques showed that we can identify NRS plaques with good diagnostic accuracy, showing that imaging markers currently only identifiable visually by radiologists may be identified objectively using mathematical formulas. We have also showed that radiomic analysis has the potential not only to identify imaging markers of CT, but also to identify metabolic activity currently only detectable using PET imaging. Furthermore, our results indicate that radiomics may have the potential to overcome the spatial resolution limitations of CT, as it may be able to identify invasive imaging markers currently only identifiable using IVUS and OCT. Also, using radiomic parameters as inputs to machine learning models we were able to classify coronary CTA cross-sections as being advanced lesions based-on histology. This may allow the exact pathological classification of diseases rather than indirect classifications with differing accuracies currently used in radiology. As with all emerging technologies, reproducibility and robustness are always a question. Our results indicate, that different image reconstruction techniques have little effect on radiomic parameters values indicating that radiomics may be robust to different scanner settings.

New image analytic techniques such as radiomics, will reshape the field of cardiac imaging. This has the potential to increase our understanding of CAD and provide more precise diagnostics and prognostication. However, these techniques are still in their infancy. Nevertheless, as fast as AI is transforming our everyday lives, these changes may come sooner than later.

## 8. ÖSSZEFOGLALÁS

A koronária CT az elmúlt években a stabil mellkasi fájdalommal rendelkező betegek első választandó vizsgálatává nőtte ki magát. Eredményeink alapján a koronária CT pontosabban képes a koszorúérbetegség kiterjedtségének megítélésére, mint az invazív angiográfia, így pontosabb rizikóstratifikációt tehet lehetővé. Továbbá a koronária CT nem csak a szűkületek leképzésére alkalmas, hanem képes magát az ateroszklerózist is megjeleníteni. Ezen egyedi tulajdonsága teszi a koronária CT-t alkalmassá a koszorúérbetegség precíziós fenotipizálásra például radiomika segítségével.

Koszorúér plakkok radiomikai elemzésével, objektív módon sikerült úgynevezett „napkin-ring” jellel rendelkező plakkokat jó diagnosztikus pontossággal azonosítani, amelyre jelenleg csak radiológusok képesek vizuális kiértékeléssel. Továbbá eredményeinkkel megmutattuk, hogy sima CT felvételek radiomikai elemzésével akár metabolikus aktivitást is tudunk azonosítani, amelyre jelenleg csak a pozitron emissziós tomográfia képes. Eredményeink arra is rámutattak, hogy a CT képek radiomikai elemzésével akár invazív képalkotó modalitások eredményeit is reprodukálni tudjuk CT felvételek segítségével. Továbbá gépi tanulós módszereket alkalmazva a radiomikai paramétereken lehetővé válhat, hogy a pontos hisztológiai kategóriáját megmondjuk az adott ateroszklerotikus elváltozásnak. Ezekon felül, különböző képi rekonstrukciókkal készült felvételek elemzéséből rámutattunk, hogy a radiomikai paraméterek esetén kismértékű változás észlelhető csak a paraméterek értékeiben különböző rekonstrukciók közt, így ezen paraméterek robosztusak lehetnek különböző képi beállításoknak.

Újszerű képi elemzési technikák, mint a radiomika nagymértékben átalakíthatják a kardiovaszkuláris képalkotást. Segítségével jobban megérthetjük a koronária betegség patológiáját és lehetőséget teremthet pontosabb diagnózisoknak és rizikóstratifikációnak. Ezen technikák még gyermekcipőben járnak. Azonban amilyen gyorsan a mesterséges intelligencia alakítja életünket, előfordulhat, hogy ezen változások hamarabb fognak bekövetkezni, mint számítanánk rá.

## 9. BIBLIOGRAPHY

1. Benjamin EJ, Muntner P, Alonso A, Bittencourt MS, Callaway CW, Carson AP, Chamberlain AM, Chang AR, Cheng S, Das SR, Delling FN, Djousse L, Elkind MSV, Ferguson JF, Fornage M, Jordan LC, Khan SS, Kissela BM, Knutson KL, Kwan TW, Lackland DT, Lewis TT, Lichtman JH, Longenecker CT, Loop MS, Lutsey PL, Martin SS, Matsushita K, Moran AE, Mussolino ME, O'Flaherty M, Pandey A, Perak AM, Rosamond WD, Roth GA, Sampson UKA, Satou GM, Schroeder EB, Shah SH, Spartano NL, Stokes A, Tirschwell DL, Tsao CW, Turakhia MP, VanWagner LB, Wilkins JT, Wong SS, Virani SS, American Heart Association Council on E, Prevention Statistics C, Stroke Statistics S. (2019) Heart Disease and Stroke Statistics-2019 Update: A Report From the American Heart Association. *Circulation*, 139: e56-e528.
2. Townsend N, Wilson L, Bhatnagar P, Wickramasinghe K, Rayner M, Nichols M. (2016) Cardiovascular disease in Europe: epidemiological update 2016. *Eur Heart J*, 37: 3232-3245.
3. D'Agostino RB, Sr., Vasan RS, Pencina MJ, Wolf PA, Cobain M, Massaro JM, Kannel WB. (2008) General cardiovascular risk profile for use in primary care: the Framingham Heart Study. *Circulation*, 117: 743-753.
4. Goff DC, Jr., Lloyd-Jones DM, Bennett G, Coady S, D'Agostino RB, Gibbons R, Greenland P, Lackland DT, Levy D, O'Donnell CJ, Robinson JG, Schwartz JS, Shero ST, Smith SC, Jr., Sorlie P, Stone NJ, Wilson PW, Jordan HS, Nevo L, Wnek J, Anderson JL, Halperin JL, Albert NM, Bozkurt B, Brindis RG, Curtis LH, DeMets D, Hochman JS, Kovacs RJ, Ohman EM, Pressler SJ, Sellke FW, Shen WK, Smith SC, Jr., Tomaselli GF, American College of Cardiology/American Heart Association Task Force on Practice G. (2014) 2013 ACC/AHA guideline on the assessment of cardiovascular risk: a report of the American College of Cardiology/American Heart Association Task Force on Practice Guidelines. *Circulation*, 129: S49-73.
5. National Cholesterol Education Program Expert Panel on Detection E, Treatment of High Blood Cholesterol in A. (2002) Third Report of the National Cholesterol Education Program (NCEP) Expert Panel on Detection, Evaluation, and

- Treatment of High Blood Cholesterol in Adults (Adult Treatment Panel III) final report. *Circulation*, 106: 3143-3421.
6. Ridker PM, Paynter NP, Rifai N, Gaziano JM, Cook NR. (2008) C-reactive protein and parental history improve global cardiovascular risk prediction: the Reynolds Risk Score for men. *Circulation*, 118: 2243-2251, 2244p following 2251.
  7. Bastuji-Garin S, Deverly A, Moyse D, Castaigne A, Mancina G, de Leeuw PW, Ruilope LM, Rosenthal T, Chatellier G, Intervention as a Goal in Hypertension Treatment Study G. (2002) The Framingham prediction rule is not valid in a European population of treated hypertensive patients. *J Hypertens*, 20: 1973-1980.
  8. DeFilippis AP, Young R, Carrubba CJ, McEvoy JW, Budoff MJ, Blumenthal RS, Kronmal RA, McClelland RL, Nasir K, Blaha MJ. (2015) An analysis of calibration and discrimination among multiple cardiovascular risk scores in a modern multiethnic cohort. *Ann Intern Med*, 162: 266-275.
  9. Fox KAA, Metra M, Morais J, Atar D. (2020) The myth of 'stable' coronary artery disease. *Nat Rev Cardiol*, 17: 9-21.
  10. Dweck MR, Doris MK, Motwani M, Adamson PD, Slomka P, Dey D, Fayad ZA, Newby DE, Berman D. (2016) Imaging of coronary atherosclerosis - evolution towards new treatment strategies. *Nat Rev Cardiol*, 13: 533-548.
  11. Pagali SR, Madaj P, Gupta M, Nair S, Hamirani YS, Min JK, Lin F, Budoff MJ. (2010) Interobserver variations of plaque severity score and segment stenosis score in coronary arteries using 64 slice multidetector computed tomography: a substudy of the ACCURACY trial. *J Cardiovasc Comput Tomogr*, 4: 312-318.
  12. Budoff MJ, Dowe D, Jollis JG, Gitter M, Sutherland J, Halamert E, Scherer M, Bellinger R, Martin A, Benton R, Delago A, Min JK. (2008) Diagnostic performance of 64-multidetector row coronary computed tomographic angiography for evaluation of coronary artery stenosis in individuals without known coronary artery disease: results from the prospective multicenter ACCURACY (Assessment by Coronary Computed Tomographic Angiography of Individuals Undergoing Invasive Coronary Angiography) trial. *J Am Coll Cardiol*, 52: 1724-1732.

13. de Graaf FR, van Velzen JE, de Boer SM, van Werkhoven JM, Kroft LJ, de Roos A, Sieders A, de Grooth GJ, Jukema JW, Schuijf JD, Bax JJ, Schalij MJ, van der Wall EE. (2013) Non-invasive computed tomography coronary angiography as a gatekeeper for invasive coronary angiography. *Int J Cardiovasc Imaging*, 29: 221-228.
14. Hu XH, Zheng WL, Wang D, Xie SS, Wu R, Zhang SZ. (2012) Accuracy of high-pitch prospectively ECG-triggering CT coronary angiography for assessment of stenosis in 103 patients: comparison with invasive coronary angiography. *Clin Radiol*, 67: 1083-1088.
15. Shaw LJ, Hausleiter J, Achenbach S, Al-Mallah M, Berman DS, Budoff MJ, Cademartiri F, Callister TQ, Chang HJ, Kim YJ, Cheng VY, Chow BJ, Cury RC, Delago AJ, Dunning AL, Feuchtner GM, Hadamitzky M, Karlsberg RP, Kaufmann PA, Leipsic J, Lin FY, Chinnaiyan KM, Maffei E, Raff GL, Villines TC, Labounty T, Gomez MJ, Min JK, Investigators CR. (2012) Coronary computed tomographic angiography as a gatekeeper to invasive diagnostic and surgical procedures: results from the multicenter CONFIRM (Coronary CT Angiography Evaluation for Clinical Outcomes: an International Multicenter) registry. *J Am Coll Cardiol*, 60: 2103-2114.
16. Butler J, Shapiro M, Reiber J, Sheth T, Ferencik M, Kurtz EG, Nichols J, Pena A, Cury RC, Brady TJ, Hoffmann U. (2007) Extent and distribution of coronary artery disease: a comparative study of invasive versus noninvasive angiography with computed angiography. *Am Heart J*, 153: 378-384.
17. Yin WH, Lu B, Hou ZH, Li N, Han L, Wu YJ, Niu HX, Silverman JR, Nicola De Cecco C, Schoepf UJ. (2013) Detection of coronary artery stenosis with sub-milliSievert radiation dose by prospectively ECG-triggered high-pitch spiral CT angiography and iterative reconstruction. *Eur Radiol*, 23: 2927-2933.
18. Maurovich-Horvat P, Ferencik M, Voros S, Merkely B, Hoffmann U. (2014) Comprehensive plaque assessment by coronary CT angiography. *Nat Rev Cardiol*, 11: 390-402.
19. Ambrose JA, Tannenbaum MA, Alexopoulos D, Hjemdahl-Monsen CE, Leavy J, Weiss M, Borrico S, Gorlin R, Fuster V. (1988) Angiographic progression of

- coronary artery disease and the development of myocardial infarction. *J Am Coll Cardiol*, 12: 56-62.
20. Farb A, Burke AP, Tang AL, Liang TY, Mannan P, Smialek J, Virmani R. (1996) Coronary plaque erosion without rupture into a lipid core. A frequent cause of coronary thrombosis in sudden coronary death. *Circulation*, 93: 1354-1363.
  21. Glaser R, Selzer F, Faxon DP, Laskey WK, Cohen HA, Slater J, Detre KM, Wilensky RL. (2005) Clinical progression of incidental, asymptomatic lesions discovered during culprit vessel coronary intervention. *Circulation*, 111: 143-149.
  22. Maurovich-Horvat P, Hoffmann U, Vorpahl M, Nakano M, Virmani R, Alkadhi H. (2010) The napkin-ring sign: CT signature of high-risk coronary plaques? *JACC Cardiovasc Imaging*, 3: 440-444.
  23. Puchner SB, Liu T, Mayrhofer T, Truong QA, Lee H, Fleg JL, Nagurney JT, Udelson JE, Hoffmann U, Ferencik M. (2014) High-risk plaque detected on coronary CT angiography predicts acute coronary syndromes independent of significant stenosis in acute chest pain: results from the ROMICAT-II trial. *J Am Coll Cardiol*, 64: 684-692.
  24. Kolossvary M, Kellermayer M, Merkely B, Maurovich-Horvat P. (2018) Cardiac Computed Tomography Radiomics: A Comprehensive Review on Radiomic Techniques. *J Thorac Imaging*, 33: 26-34.
  25. Gillies RJ, Kinahan PE, Hricak H. (2016) Radiomics: Images Are More than Pictures, They Are Data. *Radiology*, 278: 563-577.
  26. Davnall F, Yip CS, Ljungqvist G, Selmi M, Ng F, Sanghera B, Ganeshan B, Miles KA, Cook GJ, Goh V. (2012) Assessment of tumor heterogeneity: an emerging imaging tool for clinical practice? *Insights Imaging*, 3: 573-589.
  27. O'Connor JP, Rose CJ, Waterton JC, Carano RA, Parker GJ, Jackson A. (2015) Imaging intratumor heterogeneity: role in therapy response, resistance, and clinical outcome. *Clin Cancer Res*, 21: 249-257.
  28. Bickelhaupt S, Paech D, Kickingereder P, Steudle F, Lederer W, Daniel H, Gotz M, Gahlert N, Tichy D, Wiesenfarth M, Laun FB, Maier-Hein KH, Schlemmer HP, Bonekamp D. (2017) Prediction of malignancy by a radiomic signature from contrast agent-free diffusion MRI in suspicious breast lesions found on screening mammography. *J Magn Reson Imaging*, 46: 604-616.

29. Yu J, Shi Z, Lian Y, Li Z, Liu T, Gao Y, Wang Y, Chen L, Mao Y. (2017) Noninvasive IDH1 mutation estimation based on a quantitative radiomics approach for grade II glioma. *Eur Radiol*, 27: 3509-3522.
30. Zhang X, Xu X, Tian Q, Li B, Wu Y, Yang Z, Liang Z, Liu Y, Cui G, Lu H. (2017) Radiomics assessment of bladder cancer grade using texture features from diffusion-weighted imaging. *J Magn Reson Imaging*, 46: 1281-1288.
31. Coroller TP, Agrawal V, Huynh E, Narayan V, Lee SW, Mak RH, Aerts H. (2017) Radiomic-Based Pathological Response Prediction from Primary Tumors and Lymph Nodes in NSCLC. *J Thorac Oncol*, 12: 467-476.
32. Kickingereder P, Gotz M, Muschelli J, Wick A, Neuberger U, Shinohara RT, Sill M, Nowosielski M, Schlemmer HP, Radbruch A, Wick W, Bendszus M, Maier-Hein KH, Bonekamp D. (2016) Large-scale Radiomic Profiling of Recurrent Glioblastoma Identifies an Imaging Predictor for Stratifying Anti-Angiogenic Treatment Response. *Clin Cancer Res*, 22: 5765-5771.
33. Li H, Zhu Y, Burnside ES, Drukker K, Hoadley KA, Fan C, Conzen SD, Whitman GJ, Sutton EJ, Net JM, Ganott M, Huang E, Morris EA, Perou CM, Ji Y, Giger ML. (2016) MR Imaging Radiomics Signatures for Predicting the Risk of Breast Cancer Recurrence as Given by Research Versions of MammaPrint, Oncotype DX, and PAM50 Gene Assays. *Radiology*, 281: 382-391.
34. Huang Y, Liu Z, He L, Chen X, Pan D, Ma Z, Liang C, Tian J, Liang C. (2016) Radiomics Signature: A Potential Biomarker for the Prediction of Disease-Free Survival in Early-Stage (I or II) Non-Small Cell Lung Cancer. *Radiology*, 281: 947-957.
35. Prasanna P, Patel J, Partovi S, Madabhushi A, Tiwari P. (2017) Radiomic features from the peritumoral brain parenchyma on treatment-naïve multi-parametric MR imaging predict long versus short-term survival in glioblastoma multiforme: Preliminary findings. *Eur Radiol*, 27: 4188-4197.
36. Lusis AJ. (2000) Atherosclerosis. *Nature*, 407: 233-241.
37. Stary HC, Chandler AB, Dinsmore RE, Fuster V, Glagov S, Insull W, Jr., Rosenfeld ME, Schwartz CJ, Wagner WD, Wissler RW. (1995) A definition of advanced types of atherosclerotic lesions and a histological classification of

- atherosclerosis. A report from the Committee on Vascular Lesions of the Council on Arteriosclerosis, American Heart Association. *Circulation*, 92: 1355-1374.
38. Virmani R, Burke AP, Farb A, Kolodgie FD. (2006) Pathology of the vulnerable plaque. *J Am Coll Cardiol*, 47: C13-18.
  39. Napel S, Marks MP, Rubin GD, Dake MD, McDonnell CH, Song SM, Enzmann DR, Jeffrey RB, Jr. (1992) CT angiography with spiral CT and maximum intensity projection. *Radiology*, 185: 607-610.
  40. Schwartz RB, Jones KM, Chernoff DM, Mukherji SK, Khorasani R, Tice HM, Kikinis R, Hooton SM, Stieg PE, Polak JF. (1992) Common carotid artery bifurcation: evaluation with spiral CT. Work in progress. *Radiology*, 185: 513-519.
  41. Rubin GD, Shiau MC, Leung AN, Kee ST, Logan LJ, Sofilos MC. (2000) Aorta and iliac arteries: single versus multiple detector-row helical CT angiography. *Radiology*, 215: 670-676.
  42. Rubin GD, Shiau MC, Schmidt AJ, Fleischmann D, Logan L, Leung AN, Jeffrey RB, Napel S. (1999) Computed tomographic angiography: historical perspective and new state-of-the-art using multi detector-row helical computed tomography. *J Comput Assist Tomogr*, 23 Suppl 1: S83-90.
  43. Achenbach S, Ulzheimer S, Baum U, Kachelriess M, Ropers D, Giesler T, Bautz W, Daniel WG, Kalender WA, Moshage W. (2000) Noninvasive coronary angiography by retrospectively ECG-gated multislice spiral CT. *Circulation*, 102: 2823-2828.
  44. Knuuti J, Wijns W, Saraste A, Capodanno D, Barbato E, Funck-Brentano C, Prescott E, Storey RF, Deaton C, Cuisset T, Agewall S, Dickstein K, Edvardsen T, Escaned J, Gersh BJ, Svitil P, Gilard M, Hasdai D, Hatala R, Mahfoud F, Masip J, Muneretto C, Valgimigli M, Achenbach S, Bax JJ, Group ESCSD. (2019) 2019 ESC Guidelines for the diagnosis and management of chronic coronary syndromes. *Eur Heart J*.
  45. Leipsic J, Abbara S, Achenbach S, Cury R, Earls JP, Mancini GJ, Nieman K, Pontone G, Raff GL. (2014) SCCT guidelines for the interpretation and reporting of coronary CT angiography: a report of the Society of Cardiovascular Computed Tomography Guidelines Committee. *J Cardiovasc Comput Tomogr*, 8: 342-358.

46. Kolossvary M, Szilveszter B, Merkely B, Maurovich-Horvat P. (2017) Plaque imaging with CT-a comprehensive review on coronary CT angiography based risk assessment. *Cardiovasc Diagn Ther*, 7: 489-506.
47. Min JK, Dunning A, Lin FY, Achenbach S, Al-Mallah MH, Berman DS, Budoff MJ, Cademartiri F, Callister TQ, Chang HJ, Cheng V, Chinnaiyan KM, Chow B, Delago A, Hadamitzky M, Hausleiter J, Karlsberg RP, Kaufmann P, Maffei E, Nasir K, Pencina MJ, Raff GL, Shaw LJ, Villines TC. (2011) Rationale and design of the CONFIRM (COronary CT Angiography EvaluationN For Clinical Outcomes: An InteRnational Multicenter) Registry. *J Cardiovasc Comput Tomogr*, 5: 84-92.
48. Hadamitzky M, Achenbach S, Al-Mallah M, Berman D, Budoff M, Cademartiri F, Callister T, Chang HJ, Cheng V, Chinnaiyan K, Chow BJ, Cury R, Delago A, Dunning A, Feuchtner G, Gomez M, Kaufmann P, Kim YJ, Leipsic J, Lin FY, Maffei E, Min JK, Raff G, Shaw LJ, Villines TC, Hausleiter J, Investigators C. (2013) Optimized prognostic score for coronary computed tomographic angiography: results from the CONFIRM registry (COronary CT Angiography EvaluationN For Clinical Outcomes: An InteRnational Multicenter Registry). *J Am Coll Cardiol*, 62: 468-476.
49. Morise AP, Jalisi F. (2003) Evaluation of pretest and exercise test scores to assess all-cause mortality in unselected patients presenting for exercise testing with symptoms of suspected coronary artery disease. *J Am Coll Cardiol*, 42: 842-850.
50. Hadamitzky M, Taubert S, Deseive S, Byrne RA, Martinoff S, Schomig A, Hausleiter J. (2013) Prognostic value of coronary computed tomography angiography during 5 years of follow-up in patients with suspected coronary artery disease. *Eur Heart J*, 34: 3277-3285.
51. Dedic A, Kurata A, Lubbers M, Meijboom WB, van Dalen BM, Snelder S, Korbee R, Moelker A, Ouhlous M, van Domburg R, de Feijter PJ, Nieman K. (2014) Prognostic implications of non-culprit plaques in acute coronary syndrome: non-invasive assessment with coronary CT angiography. *Eur Heart J Cardiovasc Imaging*, 15: 1231-1237.
52. Nance JW, Jr., Schlett CL, Schoepf UJ, Oberoi S, Leisy HB, Barraza JM, Jr., Headden GF, Nikolaou K, Bamberg F. (2012) Incremental prognostic value of

- different components of coronary atherosclerotic plaque at cardiac CT angiography beyond coronary calcification in patients with acute chest pain. *Radiology*, 264: 679-690.
53. Virmani R, Burke AP, Kolodgie FD, Farb A. (2003) Pathology of the thin-cap fibroatheroma: a type of vulnerable plaque. *J Interv Cardiol*, 16: 267-272.
  54. Maurovich-Horvat P, Schlett CL, Alkadhi H, Nakano M, Otsuka F, Stolzmann P, Scheffel H, Ferencik M, Kriegel MF, Seifarth H, Virmani R, Hoffmann U. (2012) The napkin-ring sign indicates advanced atherosclerotic lesions in coronary CT angiography. *JACC Cardiovasc Imaging*, 5: 1243-1252.
  55. Seifarth H, Schlett CL, Nakano M, Otsuka F, Karolyi M, Liew G, Maurovich-Horvat P, Alkadhi H, Virmani R, Hoffmann U. (2012) Histopathological correlates of the napkin-ring sign plaque in coronary CT angiography. *Atherosclerosis*, 224: 90-96.
  56. Kashiwagi M, Tanaka A, Shimada K, Kitabata H, Komukai K, Nishiguchi T, Ozaki Y, Tanimoto T, Kubo T, Hirata K, Mizukoshi M, Akasaka T. (2013) Distribution, frequency and clinical implications of napkin-ring sign assessed by multidetector computed tomography. *J Cardiol*, 61: 399-403.
  57. Otsuka K, Fukuda S, Tanaka A, Nakanishi K, Taguchi H, Yoshikawa J, Shimada K, Yoshiyama M. (2013) Napkin-ring sign on coronary CT angiography for the prediction of acute coronary syndrome. *JACC Cardiovasc Imaging*, 6: 448-457.
  58. Feuchtner G, Kerber J, Burghard P, Dichtl W, Friedrich G, Bonaros N, Plank F. (2017) The high-risk criteria low-attenuation plaque <60 HU and the napkin-ring sign are the most powerful predictors of MACE: a long-term follow-up study. *Eur Heart J Cardiovasc Imaging*, 18: 772-779.
  59. Leber AW, Becker A, Knez A, von Ziegler F, Sirol M, Nikolaou K, Ohnesorge B, Fayad ZA, Becker CR, Reiser M, Steinbeck G, Boekstegers P. (2006) Accuracy of 64-slice computed tomography to classify and quantify plaque volumes in the proximal coronary system: a comparative study using intravascular ultrasound. *J Am Coll Cardiol*, 47: 672-677.
  60. Pohle K, Achenbach S, Macneill B, Ropers D, Ferencik M, Moselewski F, Hoffmann U, Brady TJ, Jang IK, Daniel WG. (2007) Characterization of non-

- calcified coronary atherosclerotic plaque by multi-detector row CT: comparison to IVUS. *Atherosclerosis*, 190: 174-180.
61. Sun J, Zhang Z, Lu B, Yu W, Yang Y, Zhou Y, Wang Y, Fan Z. (2008) Identification and quantification of coronary atherosclerotic plaques: a comparison of 64-MDCT and intravascular ultrasound. *AJR Am J Roentgenol*, 190: 748-754.
  62. Voros S, Rinehart S, Qian Z, Vazquez G, Anderson H, Murrieta L, Wilmer C, Carlson H, Taylor K, Ballard W, Karpaliotis D, Kalynych A, Brown C, 3rd. (2011) Prospective validation of standardized, 3-dimensional, quantitative coronary computed tomographic plaque measurements using radiofrequency backscatter intravascular ultrasound as reference standard in intermediate coronary arterial lesions: results from the ATLANTA (assessment of tissue characteristics, lesion morphology, and hemodynamics by angiography with fractional flow reserve, intravascular ultrasound and virtual histology, and noninvasive computed tomography in atherosclerotic plaques) I study. *JACC Cardiovasc Interv*, 4: 198-208.
  63. Kitagawa T, Yamamoto H, Horiguchi J, Ohhashi N, Tadehara F, Shokawa T, Dohi Y, Kunita E, Utsunomiya H, Kohno N, Kihara Y. (2009) Characterization of noncalcified coronary plaques and identification of culprit lesions in patients with acute coronary syndrome by 64-slice computed tomography. *JACC Cardiovasc Imaging*, 2: 153-160.
  64. Pflederer T, Marwan M, Schepis T, Ropers D, Seltmann M, Muschiol G, Daniel WG, Achenbach S. (2010) Characterization of culprit lesions in acute coronary syndromes using coronary dual-source CT angiography. *Atherosclerosis*, 211: 437-444.
  65. Yang X, Gai L, Dong W, Liu H, Sun Z, Tian F, Chen Y. (2013) Characterization of culprit lesions in acute coronary syndromes compared with stable angina pectoris by dual-source computed tomography. *Int J Cardiovasc Imaging*, 29: 945-953.
  66. Motoyama S, Kondo T, Sarai M, Sugiura A, Harigaya H, Sato T, Inoue K, Okumura M, Ishii J, Anno H, Virmani R, Ozaki Y, Hishida H, Narula J. (2007)

- Multislice computed tomographic characteristics of coronary lesions in acute coronary syndromes. *J Am Coll Cardiol*, 50: 319-326.
67. Marwan M, Taher MA, El Meniawy K, Awadallah H, Pflederer T, Schuhback A, Ropers D, Daniel WG, Achenbach S. (2011) In vivo CT detection of lipid-rich coronary artery atherosclerotic plaques using quantitative histogram analysis: a head to head comparison with IVUS. *Atherosclerosis*, 215: 110-115.
  68. Achenbach S, Boehmer K, Pflederer T, Ropers D, Seltmann M, Lell M, Anders K, Kuettner A, Uder M, Daniel WG, Marwan M. (2010) Influence of slice thickness and reconstruction kernel on the computed tomographic attenuation of coronary atherosclerotic plaque. *J Cardiovasc Comput Tomogr*, 4: 110-115.
  69. Dalager MG, Bottcher M, Dalager S, Andersen G, Thygesen J, Pedersen EM, Botker HE. (2011) Imaging atherosclerotic plaques by cardiac computed tomography in vitro: impact of contrast type and acquisition protocol. *Invest Radiol*, 46: 790-795.
  70. Tanami Y, Ikeda E, Jinzaki M, Satoh K, Nishiwaki Y, Yamada M, Okada Y, Kuribayashi S. (2010) Computed tomographic attenuation value of coronary atherosclerotic plaques with different tube voltage: an ex vivo study. *J Comput Assist Tomogr*, 34: 58-63.
  71. Cademartiri F, Mollet NR, Runza G, Bruining N, Hamers R, Somers P, Knaapen M, Verheye S, Midiri M, Krestin GP, de Feyter PJ. (2005) Influence of intracoronary attenuation on coronary plaque measurements using multislice computed tomography: observations in an ex vivo model of coronary computed tomography angiography. *Eur Radiol*, 15: 1426-1431.
  72. Cademartiri F, La Grutta L, Runza G, Palumbo A, Maffei E, Mollet NR, Bartolotta TV, Somers P, Knaapen M, Verheye S, Midiri M, Hamers R, Bruining N. (2007) Influence of convolution filtering on coronary plaque attenuation values: observations in an ex vivo model of multislice computed tomography coronary angiography. *Eur Radiol*, 17: 1842-1849.
  73. Karanasos A, Ligthart JM, Witberg KT, Regar E. (2012) Calcified nodules: an underrated mechanism of coronary thrombosis? *JACC Cardiovasc Imaging*, 5: 1071-1072.

74. Burke AP, Farb A, Malcom GT, Liang YH, Smialek J, Virmani R. (1997) Coronary risk factors and plaque morphology in men with coronary disease who died suddenly. *N Engl J Med*, 336: 1276-1282.
75. Burke AP, Weber DK, Kolodgie FD, Farb A, Taylor AJ, Virmani R. (2001) Pathophysiology of calcium deposition in coronary arteries. *Herz*, 26: 239-244.
76. Farb A, Tang AL, Burke AP, Sessums L, Liang Y, Virmani R. (1995) Sudden coronary death. Frequency of active coronary lesions, inactive coronary lesions, and myocardial infarction. *Circulation*, 92: 1701-1709.
77. Huang H, Virmani R, Younis H, Burke AP, Kamm RD, Lee RT. (2001) The impact of calcification on the biomechanical stability of atherosclerotic plaques. *Circulation*, 103: 1051-1056.
78. Maldonado N, Kelly-Arnold A, Vengrenyuk Y, Laudier D, Fallon JT, Virmani R, Cardoso L, Weinbaum S. (2012) A mechanistic analysis of the role of microcalcifications in atherosclerotic plaque stability: potential implications for plaque rupture. *Am J Physiol Heart Circ Physiol*, 303: H619-628.
79. Motoyama S, Sarai M, Harigaya H, Anno H, Inoue K, Hara T, Naruse H, Ishii J, Hishida H, Wong ND, Virmani R, Kondo T, Ozaki Y, Narula J. (2009) Computed tomographic angiography characteristics of atherosclerotic plaques subsequently resulting in acute coronary syndrome. *J Am Coll Cardiol*, 54: 49-57.
80. van Velzen JE, de Graaf FR, de Graaf MA, Schuijf JD, Kroft LJ, de Roos A, Reiber JH, Bax JJ, Jukema JW, Boersma E, Schalij MJ, van der Wall EE. (2011) Comprehensive assessment of spotty calcifications on computed tomography angiography: comparison to plaque characteristics on intravascular ultrasound with radiofrequency backscatter analysis. *J Nucl Cardiol*, 18: 893-903.
81. Kim SY, Kim KS, Seung MJ, Chung JW, Kim JH, Mun SH, Lee YS, Lee JB, Ryu JK, Choi JY, Chang SG. (2010) The culprit lesion score on multi-detector computed tomography can detect vulnerable coronary artery plaque. *Int J Cardiovasc Imaging*, 26: 245-252.
82. Otsuka F, Finn AV, Virmani R. (2013) Do vulnerable and ruptured plaques hide in heavily calcified arteries? *Atherosclerosis*, 229: 34-37.
83. Dweck MR, Chow MW, Joshi NV, Williams MC, Jones C, Fletcher AM, Richardson H, White A, McKillop G, van Beek EJ, Boon NA, Rudd JH, Newby

- DE. (2012) Coronary arterial <sup>18</sup>F-sodium fluoride uptake: a novel marker of plaque biology. *J Am Coll Cardiol*, 59: 1539-1548.
84. Glagov S, Weisenberg E, Zarins CK, Stankunavicius R, Kolettis GJ. (1987) Compensatory enlargement of human atherosclerotic coronary arteries. *N Engl J Med*, 316: 1371-1375.
85. Varnava AM, Mills PG, Davies MJ. (2002) Relationship between coronary artery remodeling and plaque vulnerability. *Circulation*, 105: 939-943.
86. Achenbach S, Ropers D, Hoffmann U, MacNeill B, Baum U, Pohle K, Brady TJ, Pomerantsev E, Ludwig J, Flachskampf FA, Wicky S, Jang IK, Daniel WG. (2004) Assessment of coronary remodeling in stenotic and nonstenotic coronary atherosclerotic lesions by multidetector spiral computed tomography. *J Am Coll Cardiol*, 43: 842-847.
87. Gauss S, Achenbach S, Pflederer T, Schuhback A, Daniel WG, Marwan M. (2011) Assessment of coronary artery remodelling by dual-source CT: a head-to-head comparison with intravascular ultrasound. *Heart*, 97: 991-997.
88. Motoyama S, Sarai M, Narula J, Ozaki Y. (2013) Coronary CT angiography and high-risk plaque morphology. *Cardiovasc Interv Ther*, 28: 1-8.
89. Min JK, Shaw LJ, Devereux RB, Okin PM, Weinsaft JW, Russo DJ, Lippolis NJ, Berman DS, Callister TQ. (2007) Prognostic value of multidetector coronary computed tomographic angiography for prediction of all-cause mortality. *J Am Coll Cardiol*, 50: 1161-1170.
90. Andreini D, Pontone G, Mushtaq S, Bartorelli AL, Bertella E, Antonioli L, Formenti A, Cortinovia S, Veglia F, Annoni A, Agostoni P, Montorsi P, Ballerini G, Fiorentini C, Pepi M. (2012) A long-term prognostic value of coronary CT angiography in suspected coronary artery disease. *JACC Cardiovasc Imaging*, 5: 690-701.
91. Cho I, Shim J, Chang HJ, Sung JM, Hong Y, Shim H, Kim YJ, Choi BW, Min JK, Kim JY, Shim CY, Hong GR, Chung N. (2012) Prognostic value of multidetector coronary computed tomography angiography in relation to exercise electrocardiogram in patients with suspected coronary artery disease. *J Am Coll Cardiol*, 60: 2205-2215.

92. Dedic A, Genders TS, Ferket BS, Galema TW, Mollet NR, Moelker A, Hunink MG, de Feyter PJ, Nieman K. (2011) Stable angina pectoris: head-to-head comparison of prognostic value of cardiac CT and exercise testing. *Radiology*, 261: 428-436.
93. Nakazato R, Arsanjani R, Achenbach S, Gransar H, Cheng VY, Dunning A, Lin FY, Al-Mallah M, Budoff MJ, Callister TQ, Chang HJ, Cademartiri F, Chinnaiyan K, Chow BJ, Delago A, Hadamitzky M, Hausleiter J, Kaufmann P, Raff G, Shaw LJ, Villines T, Cury RC, Feuchtner G, Kim YJ, Leipsic J, Berman DS, Min JK. (2014) Age-related risk of major adverse cardiac event risk and coronary artery disease extent and severity by coronary CT angiography: results from 15 187 patients from the International Multisite CONFIRM Study. *Eur Heart J Cardiovasc Imaging*, 15: 586-594.
94. Pontone G, Andreini D, Bartorelli AL, Bertella E, Cortinovis S, Mushtaq S, Foti C, Annoni A, Formenti A, Baggiano A, Conte E, Bovis F, Veglia F, Ballerini G, Fiorentini C, Agostoni P, Pepi M. (2013) A long-term prognostic value of CT angiography and exercise ECG in patients with suspected CAD. *JACC Cardiovasc Imaging*, 6: 641-650.
95. Min JK, Koo BK, Erglis A, Doh JH, Daniels DV, Jegere S, Kim HS, Dunning A, Defrance T, Leipsic J. (2012) Effect of image quality on diagnostic accuracy of noninvasive fractional flow reserve: results from the prospective multicenter international DISCOVER-FLOW study. *J Cardiovasc Comput Tomogr*, 6: 191-199.
96. Kobayashi Y, Nam CW, Tonino PA, Kimura T, De Bruyne B, Pijls NH, Fearon WF, Investigators FS. (2016) The Prognostic Value of Residual Coronary Stenoses After Functionally Complete Revascularization. *J Am Coll Cardiol*, 67: 1701-1711.
97. Pijls NH, Fearon WF, Tonino PA, Siebert U, Ikeno F, Bornschein B, van't Veer M, Klauss V, Manoharan G, Engstrom T, Oldroyd KG, Ver Lee PN, MacCarthy PA, De Bruyne B, Investigators FS. (2010) Fractional flow reserve versus angiography for guiding percutaneous coronary intervention in patients with multivessel coronary artery disease: 2-year follow-up of the FAME (Fractional

- Flow Reserve Versus Angiography for Multivessel Evaluation) study. *J Am Coll Cardiol*, 56: 177-184.
98. Tonino PA, Fearon WF, De Bruyne B, Oldroyd KG, Leeser MA, Ver Lee PN, Maccarthy PA, Van't Veer M, Pijls NH. (2010) Angiographic versus functional severity of coronary artery stenoses in the FAME study fractional flow reserve versus angiography in multivessel evaluation. *J Am Coll Cardiol*, 55: 2816-2821.
  99. Norgaard BL, Leipsic J, Gaur S, Seneviratne S, Ko BS, Ito H, Jensen JM, Mauri L, De Bruyne B, Bezerra H, Osawa K, Marwan M, Naber C, Erglis A, Park SJ, Christiansen EH, Kaltoft A, Lassen JF, Botker HE, Achenbach S, Group NXTTS. (2014) Diagnostic performance of noninvasive fractional flow reserve derived from coronary computed tomography angiography in suspected coronary artery disease: the NXT trial (Analysis of Coronary Blood Flow Using CT Angiography: Next Steps). *J Am Coll Cardiol*, 63: 1145-1155.
  100. Taylor CA, Fonte TA, Min JK. (2013) Computational fluid dynamics applied to cardiac computed tomography for noninvasive quantification of fractional flow reserve: scientific basis. *J Am Coll Cardiol*, 61: 2233-2241.
  101. Douglas PS, De Bruyne B, Pontone G, Patel MR, Norgaard BL, Byrne RA, Curzen N, Purcell I, Gutberlet M, Rioufol G, Hink U, Schuchlenz HW, Feuchtner G, Gilard M, Andreini D, Jensen JM, Hadamitzky M, Chiswell K, Cyr D, Wilk A, Wang F, Rogers C, Hlatky MA, Investigators P. (2016) 1-Year Outcomes of FFRCT-Guided Care in Patients With Suspected Coronary Disease: The PLATFORM Study. *J Am Coll Cardiol*, 68: 435-445.
  102. Douglas PS, Pontone G, Hlatky MA, Patel MR, Norgaard BL, Byrne RA, Curzen N, Purcell I, Gutberlet M, Rioufol G, Hink U, Schuchlenz HW, Feuchtner G, Gilard M, Andreini D, Jensen JM, Hadamitzky M, Chiswell K, Cyr D, Wilk A, Wang F, Rogers C, De Bruyne B, Investigators P. (2015) Clinical outcomes of fractional flow reserve by computed tomographic angiography-guided diagnostic strategies vs. usual care in patients with suspected coronary artery disease: the prospective longitudinal trial of FFR(CT): outcome and resource impacts study. *Eur Heart J*, 36: 3359-3367.
  103. Hlatky MA, De Bruyne B, Pontone G, Patel MR, Norgaard BL, Byrne RA, Curzen N, Purcell I, Gutberlet M, Rioufol G, Hink U, Schuchlenz HW, Feuchtner G,

- Gilard M, Andreini D, Jensen JM, Hadamitzky M, Wilk A, Wang F, Rogers C, Douglas PS, Investigators P. (2015) Quality-of-Life and Economic Outcomes of Assessing Fractional Flow Reserve With Computed Tomography Angiography: PLATFORM. *J Am Coll Cardiol*, 66: 2315-2323.
104. Coenen A, Lubbers MM, Kurata A, Kono A, Dedic A, Chelu RG, Dijkshoorn ML, Gijzen FJ, Ouhlous M, van Geuns RJ, Nieman K. (2015) Fractional flow reserve computed from noninvasive CT angiography data: diagnostic performance of an on-site clinician-operated computational fluid dynamics algorithm. *Radiology*, 274: 674-683.
105. Coenen A, Lubbers MM, Kurata A, Kono A, Dedic A, Chelu RG, Dijkshoorn ML, van Geuns RJ, Schoebinger M, Itu L, Sharma P, Nieman K. (2016) Coronary CT angiography derived fractional flow reserve: Methodology and evaluation of a point of care algorithm. *J Cardiovasc Comput Tomogr*, 10: 105-113.
106. De Geer J, Sandstedt M, Bjorkholm A, Alfredsson J, Janzon M, Engvall J, Persson A. (2016) Software-based on-site estimation of fractional flow reserve using standard coronary CT angiography data. *Acta Radiol*, 57: 1186-1192.
107. Donnelly PM, Kolossvary M, Karady J, Ball PA, Kelly S, Fitzsimons D, Spence MS, Celeng C, Horvath T, Szilveszter B, van Es HW, Swaans MJ, Merkely B, Maurovich-Horvat P. (2018) Experience With an On-Site Coronary Computed Tomography-Derived Fractional Flow Reserve Algorithm for the Assessment of Intermediate Coronary Stenoses. *Am J Cardiol*, 121: 9-13.
108. Yang DH, Kim YH, Roh JH, Kang JW, Ahn JM, Kweon J, Lee JB, Choi SH, Shin ES, Park DW, Kang SJ, Lee SW, Lee CW, Park SW, Park SJ, Lim TH. (2017) Diagnostic performance of on-site CT-derived fractional flow reserve versus CT perfusion. *Eur Heart J Cardiovasc Imaging*, 18: 432-440.
109. Thomas A, Banerjee AK, Gardner-Thorpe C. *The history of radiology*. Oxford University Press, Oxford, United Kingdom, 2013.
110. Skeletal Lesions Interobserver Correlation among Expert Diagnosticians Study G. (2007) Reliability of histopathologic and radiologic grading of cartilaginous neoplasms in long bones. *J Bone Joint Surg Am*, 89: 2113-2123.
111. Barabasi AL, Gulbahce N, Loscalzo J. (2011) Network medicine: a network-based approach to human disease. *Nat Rev Genet*, 12: 56-68.

112. Maroules CD, Hamilton-Craig C, Branch K, Lee J, Cury RC, Maurovich-Horvat P, Rubinshtein R, Thomas D, Williams M, Guo Y, Cury RC. (2018) Coronary artery disease reporting and data system (CAD-RADS(TM)): Inter-observer agreement for assessment categories and modifiers. *J Cardiovasc Comput Tomogr*, 12: 125-130.
113. Shannon CE. (1948) A Mathematical Theory of Communication. *Bell System Technical Journal*, 27: 379-423.
114. Galloway MM. (1975) Texture analysis using gray level run lengths. *Computer Graphics and Image Processing*, 4: 172-179.
115. Xinli W, Albregtsen F, Foyen B. (1995) Texture analysis using gray level gap length matrix. *Selected papers from the 9th Scandinavian conference on Image analysis : theory and applications of image analysis II: theory and applications of image analysis II*; Uppsala, Sweden. 242845: World Scientific Publishing Co., Inc.; 1995: 65-78.
116. Thibault G, Fertil B, Navarro C, Pereira S, Cau P, Levy N, Sequeira J, Mari J-L. (2013) Shape and Texture Indexes Application to Cell Nuclei Classification. *International Journal of Pattern Recognition and Artificial Intelligence*, 27: 1357002.
117. Amadasun M, King R. (1989) Textural features corresponding to textural properties. *IEEE Transactions on Systems, Man, and Cybernetics*, 19: 1264-1274.
118. Thibault G, Angulo J, Meyer F. (2014) Advanced statistical matrices for texture characterization: application to cell classification. *IEEE Trans Biomed Eng*, 61: 630-637.
119. Laws KI. (1980) *Textured Image Segmentation*. University of Southern California.
120. Minkowski H. (1903) Volumen und Oberfläche. *Mathematische Annalen*, 57: 447.
121. Larkin TJ, Canuto HC, Kettunen MI, Booth TC, Hu DE, Krishnan AS, Bohndiek SE, Neves AA, McLachlan C, Hobson MP, Brindle KM. (2014) Analysis of image heterogeneity using 2D Minkowski functionals detects tumor responses to treatment. *Magn Reson Med*, 71: 402-410.

122. Mandelbrot B. (1967) How Long Is the Coast of Britain? Statistical Self-Similarity and Fractional Dimension. *Science*, 156: 636-638.
123. Lopes R, Betrouni N. (2009) Fractal and multifractal analysis: a review. *Med Image Anal*, 13: 634-649.
124. Rose CJ, Mills SJ, O'Connor JP, Buonaccorsi GA, Roberts C, Watson Y, Cheung S, Zhao S, Witcher B, Jackson A, Parker GJ. (2009) Quantifying spatial heterogeneity in dynamic contrast-enhanced MRI parameter maps. *Magn Reson Med*, 62: 488-499.
125. Dettori L, Semler L. (2007) A comparison of wavelet, ridgelet, and curvelet-based texture classification algorithms in computed tomography. *Comput Biol Med*, 37: 486-498.
126. Kolosvary M, De Cecco CN, Feuchtner G, Maurovich-Horvat P. (2019) Advanced atherosclerosis imaging by CT: Radiomics, machine learning and deep learning. *J Cardiovasc Comput Tomogr*, 13: 274-280.
127. Rumsfeld JS, Joynt KE, Maddox TM. (2016) Big data analytics to improve cardiovascular care: promise and challenges. *Nat Rev Cardiol*, 13: 350-359.
128. Russell SJ, Norvig P. *Artificial intelligence : a modern approach*. Pearson, Upper Saddle River, N.J., 2010.
129. Samuel AL. (1959) Some Studies in Machine Learning Using the Game of Checkers. *IBM Journal of Research and Development*, 3: 210-229.
130. Singh G, Al'Aref SJ, Van Assen M, Kim TS, van Rosendaal A, Kolli KK, Dwivedi A, Maliakal G, Pandey M, Wang J, Do V, Gummalla M, De Cecco CN, Min JK. (2018) Machine learning in cardiac CT: Basic concepts and contemporary data. *J Cardiovasc Comput Tomogr*, 12: 192-201.
131. Voros S, Maurovich-Horvat P, Marvasty IB, Bansal AT, Barnes MR, Vazquez G, Murray SS, Voros V, Merkely B, Brown BO, Warnick GR. (2014) Precision phenotyping, panomics, and system-level bioinformatics to delineate complex biologies of atherosclerosis: rationale and design of the "Genetic Loci and the Burden of Atherosclerotic Lesions" study. *J Cardiovasc Comput Tomogr*, 8: 442-451.
132. Wu FZ, Wu MT. (2015) 2014 SCCT guidelines for the interpretation and reporting of coronary CT angiography: a report of the Society of Cardiovascular

- Computed Tomography Guidelines Committee. *J Cardiovasc Comput Tomogr*, 9: e3.
133. Bittencourt MS, Hulten E, Ghoshhajra B, O'Leary D, Christman MP, Montana P, Truong QA, Steigner M, Murthy VL, Rybicki FJ, Nasir K, Gowdak LH, Hainer J, Brady TJ, Di Carli MF, Hoffmann U, Abbara S, Blankstein R. (2014) Prognostic value of nonobstructive and obstructive coronary artery disease detected by coronary computed tomography angiography to identify cardiovascular events. *Circ Cardiovasc Imaging*, 7: 282-291.
  134. Boogers MJ, Schuijf JD, Kitslaar PH, van Werkhoven JM, de Graaf FR, Boersma E, van Velzen JE, Dijkstra J, Adame IM, Kroft LJ, de Roos A, Schreur JH, Heijnenbroek MW, Jukema JW, Reiber JH, Bax JJ. (2010) Automated quantification of stenosis severity on 64-slice CT: a comparison with quantitative coronary angiography. *JACC Cardiovasc Imaging*, 3: 699-709.
  135. Kolossvary M, Karady J, Szilveszter B, Kitslaar P, Hoffmann U, Merkely B, Maurovich-Horvat P. (2017) Radiomic Features Are Superior to Conventional Quantitative Computed Tomographic Metrics to Identify Coronary Plaques With Napkin-Ring Sign. *Circ Cardiovasc Imaging*, 10.
  136. Kolossvary M. (2020) RIA: Radiomics Image Analysis Toolbox for Grayscale Images (computer program), Budapest, Hungary, <https://CRAN.R-project.org/package=RIA>, [accessed: 2020-01-08].
  137. Hothorn T, Hornik K, Wiel MAvd, Zeileis A. (2008) Implementing a Class of Permutation Tests: ThecoinPackage. *Journal of Statistical Software*, 28: 1-23.
  138. Robin X, Turck N, Hainard A, Tiberti N, Lisacek F, Sanchez JC, Muller M. (2011) pROC: an open-source package for R and S+ to analyze and compare ROC curves. *BMC Bioinformatics*, 12: 77.
  139. Rousseeuw PJ. (1987) Silhouettes: A graphical aid to the interpretation and validation of cluster analysis. *Journal of Computational and Applied Mathematics*, 20: 53-65.
  140. Dietterich TG. (1998) Approximate Statistical Tests for Comparing Supervised Classification Learning Algorithms. *Neural Comput*, 10: 1895-1923.

141. Gao X, Starmer J, Martin ER. (2008) A multiple testing correction method for genetic association studies using correlated single nucleotide polymorphisms. *Genet Epidemiol*, 32: 361-369.
142. Johnson RC, Nelson GW, Troyer JL, Lautenberger JA, Kessing BD, Winkler CA, O'Brien SJ. (2010) Accounting for multiple comparisons in a genome-wide association study (GWAS). *BMC Genomics*, 11: 724.
143. R Core Team (2020) R: A language and environment for statistical computing. R Foundation for Statistical Computing (computer program), Vienna, Austria, <https://www.r-project.org/>, [accessed: 2020-01-08].
144. Lee JM, Bang JI, Koo BK, Hwang D, Park J, Zhang J, Yaliang T, Suh M, Paeng JC, Shiono Y, Kubo T, Akasaka T. (2017) Clinical Relevance of (18)F-Sodium Fluoride Positron-Emission Tomography in Noninvasive Identification of High-Risk Plaque in Patients With Coronary Artery Disease. *Circ Cardiovasc Imaging*, 10.
145. Hoffmann U, Moselewski F, Nieman K, Jang IK, Ferencik M, Rahman AM, Cury RC, Abbara S, Joneidi-Jafari H, Achenbach S, Brady TJ. (2006) Noninvasive assessment of plaque morphology and composition in culprit and stable lesions in acute coronary syndrome and stable lesions in stable angina by multidetector computed tomography. *J Am Coll Cardiol*, 47: 1655-1662.
146. Karolyi M, Szilveszter B, Kolossvary M, Takx RA, Celeng C, Bartykowszki A, Jermendy AL, Panajotu A, Karady J, Raaijmakers R, Giepmans W, Merkely B, Maurovich-Horvat P. (2017) Iterative model reconstruction reduces calcified plaque volume in coronary CT angiography. *Eur J Radiol*, 87: 83-89.
147. Galloway MM. (1975) Texture analysis using gray level run lengths. *Computer Graphics and Image Processing*, 4: 172-179.
148. Haralick RM, Shanmugam K, Dinstein IH. (1973) Textural Features for Image Classification. *IEEE Transactions on Systems, Man, and Cybernetics*, SMC-3: 610-621.
149. Joshi NV, Vesey AT, Williams MC, Shah AS, Calvert PA, Craighead FH, Yeoh SE, Wallace W, Salter D, Fletcher AM, van Beek EJ, Flapan AD, Uren NG, Behan MW, Cruden NL, Mills NL, Fox KA, Rudd JH, Dweck MR, Newby DE. (2014) 18F-fluoride positron emission tomography for identification of ruptured and

- high-risk coronary atherosclerotic plaques: a prospective clinical trial. *Lancet*, 383: 705-713.
150. Maehara A, Mintz GS, Bui AB, Walter OR, Castagna MT, Canos D, Pichard AD, Satler LF, Waksman R, Suddath WO, Laird JR, Jr., Kent KM, Weissman NJ. (2002) Morphologic and angiographic features of coronary plaque rupture detected by intravascular ultrasound. *J Am Coll Cardiol*, 40: 904-910.
  151. Mintz GS, Nissen SE, Anderson WD, Bailey SR, Erbel R, Fitzgerald PJ, Pinto FJ, Rosenfield K, Siegel RJ, Tuzcu EM, Yock PG. (2001) American College of Cardiology Clinical Expert Consensus Document on Standards for Acquisition, Measurement and Reporting of Intravascular Ultrasound Studies (IVUS). A report of the American College of Cardiology Task Force on Clinical Expert Consensus Documents. *J Am Coll Cardiol*, 37: 1478-1492.
  152. Kim J-H. (2009) Estimating classification error rate: Repeated cross-validation, repeated hold-out and bootstrap. *Computational Statistics & Data Analysis*, 53: 3735-3745.
  153. Pedregosa F, Varoquaux G, Gramfort A, Michel V, Thirion B, Grisel O, Blondel M, Prettenhofer P, Weiss R, Dubourg V, Vanderplas J, Passos A, Cournapeau D, Brucher M, Perrot M, Duchesnay E. (2011) Scikit-learn: Machine Learning in Python. *Journal of Machine Learning Research*, 12: 2825-2830.
  154. Karady J, Panajotu A, Kolossvary M, Szilveszter B, Jermendy AL, Bartykowszki A, Karolyi M, Celeng C, Merkely B, Maurovich-Horvat P. (2017) The effect of four-phasic versus three-phasic contrast media injection protocols on extravasation rate in coronary CT angiography: a randomized controlled trial. *Eur Radiol*, 27: 4538-4543.
  155. Symons R, Morris JZ, Wu CO, Pourmorteza A, Ahlman MA, Lima JA, Chen MY, Mallek M, Sandfort V, Bluemke DA. (2016) Coronary CT Angiography: Variability of CT Scanners and Readers in Measurement of Plaque Volume. *Radiology*, 281: 737-748.
  156. Ferencik M, Liu T, Mayrhofer T, Puchner SB, Lu MT, Maurovich-Horvat P, Pope JH, Truong QA, Udelson JE, Peacock WF, White CS, Woodard PK, Fleg JL, Nagurney JT, Januzzi JL, Hoffmann U. (2015) hs-Troponin I Followed by CT Angiography Improves Acute Coronary Syndrome Risk Stratification Accuracy

- and Work-Up in Acute Chest Pain Patients: Results From ROMICAT II Trial. *JACC Cardiovasc Imaging*, 8: 1272-1281.
157. Sigurdsson S, Alexandersson KF, Sulem P, Feenstra B, Gudmundsdottir S, Halldorsson GH, Olafsson S, Sigurdsson A, Rafnar T, Thorgeirsson T, Sorensen E, Nordholm-Carstensen A, Burcharth J, Andersen J, Jorgensen HS, Possfelt-Moller E, Ullum H, Thorleifsson G, Masson G, Thorsteinsdottir U, Melbye M, Gudbjartsson DF, Stefansson T, Jonsdottir I, Stefansson K. (2017) Sequence variants in ARHGAP15, COLQ and FAM155A associate with diverticular disease and diverticulitis. *Nat Commun*, 8: 15789.
  158. Maurovich-Horvat P, Schlett CL, Alkadhi H, Nakano M, Stolzmann P, Vorpahl M, Scheffel H, Tanaka A, Warger WC, 2nd, Maehara A, Ma S, Kriegel MF, Kaple RK, Seifarth H, Bamberg F, Mintz GS, Tearney GJ, Virmani R, Hoffmann U. (2012) Differentiation of early from advanced coronary atherosclerotic lesions: systematic comparison of CT, intravascular US, and optical frequency domain imaging with histopathologic examination in ex vivo human hearts. *Radiology*, 265: 393-401.
  159. Movat HZ. (1955) Demonstration of all connective tissue elements in a single section; pentachrome stains. *AMA Arch Pathol*, 60: 289-295.
  160. Donnelly P, Maurovich-Horvat P, Vorpahl M, Nakano M, Kaple RK, Warger W, Tanaka A, Tearney G, Virmani R, Hoffmann U. (2010) Multimodality imaging atlas of coronary atherosclerosis. *JACC Cardiovasc Imaging*, 3: 876-880.
  161. Virmani R, Kolodgie FD, Burke AP, Farb A, Schwartz SM. (2000) Lessons from sudden coronary death: a comprehensive morphological classification scheme for atherosclerotic lesions. *Arterioscler Thromb Vasc Biol*, 20: 1262-1275.
  162. Fedorov A, Beichel R, Kalpathy-Cramer J, Finet J, Fillion-Robin JC, Pujol S, Bauer C, Jennings D, Fennessy F, Sonka M, Buatti J, Aylward S, Miller JV, Pieper S, Kikinis R. (2012) 3D Slicer as an image computing platform for the Quantitative Imaging Network. *Magn Reson Imaging*, 30: 1323-1341.
  163. Schlett CL, Ferencik M, Celeng C, Maurovich-Horvat P, Scheffel H, Stolzmann P, Do S, Kauczor HU, Alkadhi H, Bamberg F, Hoffmann U. (2013) How to assess non-calcified plaque in CT angiography: delineation methods affect diagnostic

- accuracy of low-attenuation plaque by CT for lipid-core plaque in histology. *Eur Heart J Cardiovasc Imaging*, 14: 1099-1105.
164. Kolossvary M, Szilveszter B, Karady J, Drobni ZD, Merkely B, Maurovich-Horvat P. (2019) Effect of image reconstruction algorithms on volumetric and radiomic parameters of coronary plaques. *J Cardiovasc Comput Tomogr*, 13: 325-330.
  165. Géron A. (2017) *Hands-on machine learning with Scikit-Learn and TensorFlow : concepts, tools, and techniques to build intelligent systems*. O'Reilly Media, Inc., Sebastopol, California.
  166. DeLong ER, DeLong DM, Clarke-Pearson DL. (1988) Comparing the areas under two or more correlated receiver operating characteristic curves: a nonparametric approach. *Biometrics*, 44: 837-845.
  167. Kolossvary M, Szilveszter B, Edes IF, Nardai S, Voros V, Hartyanszky I, Merkely B, Voros S, Maurovich-Horvat P. (2016) Comparison of Quantity of Coronary Atherosclerotic Plaques Detected by Computed Tomography Versus Angiography. *Am J Cardiol*, 117: 1863-1867.
  168. Kolossvary M, Park J, Bang JI, Zhang J, Lee JM, Paeng JC, Merkely B, Narula J, Kubo T, Akasaka T, Koo BK, Maurovich-Horvat P. (2019) Identification of invasive and radionuclide imaging markers of coronary plaque vulnerability using radiomic analysis of coronary computed tomography angiography. *Eur Heart J Cardiovasc Imaging*, 20: 1250-1258.
  169. Kolossvary M, Karady J, Kikuchi Y, Ivanov A, Schlett CL, Lu MT, Foldyna B, Merkely B, Aerts HJ, Hoffmann U, Maurovich-Horvat P. (2019) Radiomics versus Visual and Histogram-based Assessment to Identify Atheromatous Lesions at Coronary CT Angiography: An ex Vivo Study. *Radiology*, 293: 89-96.
  170. Kubo T, Maehara A, Mintz GS, Doi H, Tsujita K, Choi SY, Katoh O, Nasu K, Koenig A, Pieper M, Rogers JH, Wijns W, Bose D, Margolis MP, Moses JW, Stone GW, Leon MB. (2010) The dynamic nature of coronary artery lesion morphology assessed by serial virtual histology intravascular ultrasound tissue characterization. *J Am Coll Cardiol*, 55: 1590-1597.

171. Burrell HC, Pinder SE, Wilson AR, Evans AJ, Yeoman LJ, Elston CW, Ellis IO. (1996) The positive predictive value of mammographic signs: a review of 425 non-palpable breast lesions. *Clin Radiol*, 51: 277-281.
172. Orel SG, Kay N, Reynolds C, Sullivan DC. (1999) BI-RADS categorization as a predictor of malignancy. *Radiology*, 211: 845-850.
173. Grimm LJ, Anderson AL, Baker JA, Johnson KS, Walsh R, Yoon SC, Ghate SV. (2015) Interobserver Variability Between Breast Imagers Using the Fifth Edition of the BI-RADS MRI Lexicon. *AJR Am J Roentgenol*, 204: 1120-1124.
174. Altazi BA, Zhang GG, Fernandez DC, Montejo ME, Hunt D, Werner J, Biagioli MC, Moros EG. (2017) Reproducibility of F18-FDG PET radiomic features for different cervical tumor segmentation methods, gray-level discretization, and reconstruction algorithms. *J Appl Clin Med Phys*, 18: 32-48.
175. Cortes-Rodicio J, Sanchez-Merino G, Garcia-Fidalgo MA, Tobalina-Larrea I. (2016) Identification of low variability textural features for heterogeneity quantification of (18)F-FDG PET/CT imaging. *Rev Esp Med Nucl Imagen Mol*, 35: 379-384.
176. Hu P, Wang J, Zhong H, Zhou Z, Shen L, Hu W, Zhang Z. (2016) Reproducibility with repeat CT in radiomics study for rectal cancer. *Oncotarget*, 7: 71440-71446.
177. Shiri I, Rahmim A, Ghaffarian P, Geramifar P, Abdollahi H, Bitarafan-Rajabi A. (2017) The impact of image reconstruction settings on 18F-FDG PET radiomic features: multi-scanner phantom and patient studies. *Eur Radiol*, 27: 4498-4509.
178. Mackin D, Fave X, Zhang L, Fried D, Yang J, Taylor B, Rodriguez-Rivera E, Dodge C, Jones AK, Court L. (2015) Measuring Computed Tomography Scanner Variability of Radiomics Features. *Invest Radiol*, 50: 757-765.
179. Marwick TH, Cho I, B OH, Min JK. (2015) Finding the Gatekeeper to the Cardiac Catheterization Laboratory: Coronary CT Angiography or Stress Testing? *J Am Coll Cardiol*, 65: 2747-2756.
180. Yang L, Zhou T, Zhang R, Xu L, Peng Z, Ding J, Wang S, Li M, Sun G. (2014) Meta-analysis: diagnostic accuracy of coronary CT angiography with prospective ECG gating based on step-and-shoot, Flash and volume modes for detection of coronary artery disease. *Eur Radiol*, 24: 2345-2352.

181. Antonopoulos AS, Sanna F, Sabharwal N, Thomas S, Oikonomou EK, Herdman L, Margaritis M, Shirodaria C, Kampoli AM, Akoumianakis I, Petrou M, Sayeed R, Krasopoulos G, Psarros C, Ciccone P, Brophy CM, Digby J, Kelion A, Uberoi R, Anthony S, Alexopoulos N, Tousoulis D, Achenbach S, Neubauer S, Channon KM, Antoniades C. (2017) Detecting human coronary inflammation by imaging perivascular fat. *Sci Transl Med*, 9.
182. Berenguer R, Pastor-Juan MDR, Canales-Vazquez J, Castro-Garcia M, Villas MV, Mansilla Legorburo F, Sabater S. (2018) Radiomics of CT Features May Be Nonreproducible and Redundant: Influence of CT Acquisition Parameters. *Radiology*, 288: 407-415.
183. Shafiq-Ul-Hassan M, Zhang GG, Latifi K, Ullah G, Hunt DC, Balagurunathan Y, Abdalah MA, Schabath MB, Goldgof DG, Mackin D, Court LE, Gillies RJ, Moros EG. (2017) Intrinsic dependencies of CT radiomic features on voxel size and number of gray levels. *Med Phys*, 44: 1050-1062.
184. Deseive S, Chen MY, Korosoglou G, Leipsic J, Martuscelli E, Carrascosa P, Mirsadraee S, White C, Hadamitzky M, Martinoff S, Menges AL, Bischoff B, Massberg S, Hausleiter J. (2015) Prospective Randomized Trial on Radiation Dose Estimates of CT Angiography Applying Iterative Image Reconstruction: The PROTECTION V Study. *JACC Cardiovasc Imaging*, 8: 888-896.
185. Schindler A, Vliegenthart R, Schoepf UJ, Blanke P, Ebersberger U, Cho YJ, Allmendinger T, Vogt S, Raupach R, Fink C, Saam T, Bamberg F, Nikolaou K, Apfaltrer P. (2014) Iterative image reconstruction techniques for CT coronary artery calcium quantification: comparison with traditional filtered back projection in vitro and in vivo. *Radiology*, 270: 387-393.
186. Szilveszter B, Elzomor H, Karolyi M, Kolossvary M, Raaijmakers R, Benke K, Celeng C, Bartykowszki A, Bagyura Z, Lux A, Merkely B, Maurovich-Horvat P. (2016) The effect of iterative model reconstruction on coronary artery calcium quantification. *Int J Cardiovasc Imaging*, 32: 153-160.
187. Willemink MJ, den Harder AM, Foppen W, Schilham AM, Rienks R, Laufer EM, Nieman K, de Jong PA, Budde RP, Nathoe HM, Leiner T. (2016) Finding the optimal dose reduction and iterative reconstruction level for coronary calcium scoring. *J Cardiovasc Comput Tomogr*, 10: 69-75.

188. Precht H, Kitslaar PH, Broersen A, Dijkstra J, Gerke O, Thygesen J, Egstrup K, Lambrechtsen J. (2016) Influence of Adaptive Statistical Iterative Reconstruction on coronary plaque analysis in coronary computed tomography angiography. *J Cardiovasc Comput Tomogr*, 10: 507-516.
189. Takx RA, Willeminck MJ, Nathoe HM, Schilham AM, Budde RP, de Jong PA, Leiner T. (2014) The effect of iterative reconstruction on quantitative computed tomography assessment of coronary plaque composition. *Int J Cardiovasc Imaging*, 30: 155-163.
190. Altazi BA, Fernandez DC, Zhang GG, Hawkins S, Naqvi SM, Kim Y, Hunt D, Latifi K, Biagioli M, Venkat P, Moros EG. (2018) Investigating multi-radiomic models for enhancing prediction power of cervical cancer treatment outcomes. *Phys Med*, 46: 180-188.
191. Corino VDA, Montin E, Messina A, Casali PG, Gronchi A, Marchiano A, Mainardi LT. (2018) Radiomic analysis of soft tissues sarcomas can distinguish intermediate from high-grade lesions. *J Magn Reson Imaging*, 47: 829-840.
192. Lovinfosse P, Polus M, Van Daele D, Martinive P, Daenen F, Hatt M, Visvikis D, Koopmansch B, Lambert F, Coimbra C, Seidel L, Albert A, Delvenne P, Hustinx R. (2018) FDG PET/CT radiomics for predicting the outcome of locally advanced rectal cancer. *Eur J Nucl Med Mol Imaging*, 45: 365-375.
193. Zhu X, Dong D, Chen Z, Fang M, Zhang L, Song J, Yu D, Zang Y, Liu Z, Shi J, Tian J. (2018) Radiomic signature as a diagnostic factor for histologic subtype classification of non-small cell lung cancer. *Eur Radiol*, 28: 2772-2778.
194. Nadjiri J, Hausleiter J, Jahnichen C, Will A, Hendrich E, Martinoff S, Hadamitzky M. (2016) Incremental prognostic value of quantitative plaque assessment in coronary CT angiography during 5 years of follow up. *J Cardiovasc Comput Tomogr*, 10: 97-104.
195. Schlett CL, Maurovich-Horvat P, Ferencik M, Alkadhi H, Stolzmann P, Scheffel H, Seifarth H, Nakano M, Do S, Vorpahl M, Kauczor HU, Bamberg F, Tearney GJ, Virmani R, Hoffmann U. (2013) Histogram analysis of lipid-core plaques in coronary computed tomographic angiography: ex vivo validation against histology. *Invest Radiol*, 48: 646-653.

196. Puchner SB, Ferencik M, Maurovich-Horvat P, Nakano M, Otsuka F, Kauczor HU, Virmani R, Hoffmann U, Schlett CL. (2015) Iterative image reconstruction algorithms in coronary CT angiography improve the detection of lipid-core plaque--a comparison with histology. *Eur Radiol*, 25: 15-23.
197. Henglin M, Stein G, Hushcha PV, Snoek J, Wiltschko AB, Cheng S. (2017) Machine Learning Approaches in Cardiovascular Imaging. *Circ Cardiovasc Imaging*, 10.
198. Motwani M, Dey D, Berman DS, Germano G, Achenbach S, Al-Mallah MH, Andreini D, Budoff MJ, Cademartiri F, Callister TQ, Chang HJ, Chinnaiyan K, Chow BJ, Cury RC, Delago A, Gomez M, Gransar H, Hadamitzky M, Hausleiter J, Hindoyan N, Feuchtner G, Kaufmann PA, Kim YJ, Leipsic J, Lin FY, Maffei E, Marques H, Pontone G, Raff G, Rubinshtein R, Shaw LJ, Stehli J, Villines TC, Dunning A, Min JK, Slomka PJ. (2017) Machine learning for prediction of all-cause mortality in patients with suspected coronary artery disease: a 5-year multicentre prospective registry analysis. *Eur Heart J*, 38: 500-507.
199. Kolossvary M, De Cecco CN, Feuchtner G, Maurovich-Horvat P. (2019) Advanced atherosclerosis imaging by CT: Radiomics, machine learning and deep learning. *J Cardiovasc Comput Tomogr*.
200. Ferencik M, Mayrhofer T, Bittner DO, Emami H, Puchner SB, Lu MT, Meyersohn NM, Ivanov AV, Adami EC, Patel MR, Mark DB, Udelson JE, Lee KL, Douglas PS, Hoffmann U. (2018) Use of High-Risk Coronary Atherosclerotic Plaque Detection for Risk Stratification of Patients With Stable Chest Pain: A Secondary Analysis of the PROMISE Randomized Clinical Trial. *JAMA Cardiol*, 3: 144-152.

## 10. CANDIDATE'S PUBLICATIONS

### 10.1. Publications discussed in the present thesis

1. **Kolossvary M**, Szilveszter B, Edes IF, Nardai S, Voros V, Hartyanszky I, Merkely B, Voros S, Maurovich-Horvat P. (2016) Comparison of Quantity of Coronary Atherosclerotic Plaques Detected by Computed Tomography Versus Angiography. *Am J Cardiol*, 117: 1863-1867. **IF: 3.398**
2. **Kolossvary M**, Karady J, Szilveszter B, Kitslaar P, Hoffmann U, Merkely B, Maurovich-Horvat P. (2017) Radiomic Features Are Superior to Conventional Quantitative Computed Tomographic Metrics to Identify Coronary Plaques With Napkin-Ring Sign. *Circ Cardiovasc Imaging*, 10. **IF: 6.221**
3. **Kolossvary M**, Park J, Bang JI, Zhang J, Lee JM, Paeng JC, Merkely B, Narula J, Kubo T, Akasaka T, Koo BK, Maurovich-Horvat P. (2019) Identification of invasive and radionuclide imaging markers of coronary plaque vulnerability using radiomic analysis of coronary computed tomography angiography. *Eur Heart J Cardiovasc Imaging*, 20: 1250-1258. **IF: 5.260**
4. **Kolossvary M**, Szilveszter B, Karady J, Drobni ZD, Merkely B, Maurovich-Horvat P. (2019) Effect of image reconstruction algorithms on volumetric and radiomic parameters of coronary plaques. *J Cardiovasc Comput Tomogr*, 13: 325-330. **IF: 3.316**
5. **Kolossvary M**, Karady J, Kikuchi Y, Ivanov A, Schlett CL, Lu MT, Foldyna B, Merkely B, Aerts HJ, Hoffmann U, Maurovich-Horvat P. (2019) Radiomics versus Visual and Histogram-based Assessment to Identify Atheromatous Lesions at Coronary CT Angiography: An ex Vivo Study. *Radiology*, 293: 89-96. **IF: 7.608**

### 10.2. Publications not related to the present thesis

1. Bagyura Z, **Kolossvary M**, Merkely B, Maurovich-Horvat P. (2017) [Computer tomography examination of the coronary system - National Plaque Registry and Database, Hungary]. *Orv Hetil*, 158: 106-110. **IF: 0.322**
2. Bagyura Z, **Kolossváry M**, Merkely BP, Maurovich-Horvat P. (2015) Személyre szabott kardiovaszkuláris rizikóbecslés koronária CT-vel Strukturált leletezés és az OPeRA (Országos Plaque Regiszter és Adatbázis) Projekt. *IME: INTERDISZCIPLINÁRIS MAGYAR EGÉSZSÉGÜGY / INFORMATIKA ÉS MENEDZSMENT AZ EGÉSZSÉGÜGYBEN*, 14: 19-23. **IF: 0.000**
3. Banga PV, Varga A, Csobay-Novak C, **Kolossvary M**, Szanto E, Oderich GS, Entz L, Sotonyi P. (2018) Incomplete circle of Willis is associated with a higher incidence of neurologic events during carotid eversion endarterectomy without shunting. *J Vasc Surg*, 68: 1764-1771. **IF: 3.243**
4. Barta H, Jermendy A, **Kolossvary M**, Kozak LR, Lakatos A, Meder U, Szabo M, Rudas G. (2018) Prognostic value of early, conventional proton magnetic resonance spectroscopy in cooled asphyxiated infants. *BMC Pediatr*, 18: 302. **IF: 1.983**
5. Bartykowszki A, **Kolossvary M**, Jermendy AL, Karady J, Szilveszter B, Karolyi M, Balogh O, Sax B, Merkely B, Maurovich-Horvat P. (2018) Image Quality of Prospectively ECG-Triggered Coronary CT Angiography in Heart Transplant Recipients. *AJR Am J Roentgenol*, 210: 314-319. **IF: 3.161**
6. Bencsik P, Sasi V, Kiss K, Kupai K, **Kolossvary M**, Maurovich-Horvat P, Csont T, Ungi I, Merkely B, Ferdinandy P. (2015) Serum lipids and cardiac function correlate with nitrotyrosine and MMP activity in coronary artery disease patients. *Eur J Clin Invest*, 45: 692-701. **IF: 2.687**
7. Bikov A, **Kolossvary M**, Jermendy AL, Drobni ZD, Tarnoki AD, Tarnoki DL, Forgo B, Kovacs DT, Losonczy G, Kunos L, Voros S, Merkely B, Maurovich-Horvat P. (2019) Comprehensive coronary plaque assessment in patients with obstructive sleep apnea. *J Sleep Res*, 28: e12828. **IF: 3.432**
8. Celeng C, **Kolossvary M**, Kovacs A, Molnar AA, Szilveszter B, Horvath T, Karolyi M, Jermendy AL, Tarnoki AD, Tarnoki DL, Karady J, Voros S, Jermendy G, Merkely B, Maurovich-Horvat P. (2017) Aortic root dimensions are

- predominantly determined by genetic factors: a classical twin study. *Eur Radiol*, 27: 2419-2425. **IF: 4.027**
9. Csobay-Novak C, Fontanini DM, Szilagyí B, Szeberin Z, **Kolossvary M**, Maurovich-Horvat P, Huttli K, Sotonyi P. (2017) Thoracic Aortic Strain is Irrelevant Regarding Endograft Sizing in Most Young Patients. *Ann Vasc Surg*, 38: 227-232. **IF: 1.363**
  10. Donnelly PM, **Kolossvary M**, Karady J, Ball PA, Kelly S, Fitzsimons D, Spence MS, Celeng C, Horvath T, Szilveszter B, van Es HW, Swaans MJ, Merkely B, Maurovich-Horvat P. (2018) Experience With an On-Site Coronary Computed Tomography-Derived Fractional Flow Reserve Algorithm for the Assessment of Intermediate Coronary Stenoses. *Am J Cardiol*, 121: 9-13. **IF: 2.843**
  11. Drobni ZD, **Kolossvary M**, Karády J, Jermendy Á, Littvay L, Tárnoki ÁD, Tárnoki DL, Voros S, Jermendy G, Merkely B, Maurovich-Horvat P. (2017) Van-e összefüggés az epikardiális zsírszövet és a koszorúér-betegség között? *Cardiologia Hungarica*, 47: 25-29. **IF: 0.000**
  12. Drobni ZD, **Kolossvary M**, Szilveszter B, Merkely B, Maurovich-Horvat P. (2018) A koronária-CT-angiográfia jelentősége a mindennapi gyakorlatban stabil anginás betegek körében. *Cardiologia Hungarica*, 48: 52-57. **IF: 0.000**
  13. Fontanini DM, Fazekas G, Vallus G, Juhasz G, Varadi R, Kovesi Z, **Kolossvary M**, Szeberin Z. (2018) [Thoracic aortic stentgraft implantations in Hungary from 2012 to 2016]. *Orv Hetil*, 159: 53-57. **IF: 0.564**
  14. Jermendy AL, **Kolossvary M**, Drobni ZD, Tarnoki AD, Tarnoki DL, Karady J, Voros S, Lamb HJ, Merkely B, Jermendy G, Maurovich-Horvat P. (2018) Assessing genetic and environmental influences on epicardial and abdominal adipose tissue quantities: a classical twin study. *Int J Obes (Lond)*, 42: 163-168. **IF: 4.514**
  15. Karády J, Drobni ZD, **Kolossvary M**, Maurovich-Horvat P. (2015) Non-invasive Assessment of Coronary Plaque Morphology. *Current Radiology Reports*, 3. **IF: 0.000**
  16. Karady J, Panajotu A, **Kolossvary M**, Szilveszter B, Jermendy AL, Bartykowszki A, Karolyi M, Celeng C, Merkely B, Maurovich-Horvat P. (2017) The effect of

- four-phasic versus three-phasic contrast media injection protocols on extravasation rate in coronary CT angiography: a randomized controlled trial. *Eur Radiol*, 27: 4538-4543. **IF: 4.027**
17. Karolyi M, **Kolossvary M**, Bartykowszki A, Kocsmar I, Szilveszter B, Karady J, Merkely B, Maurovich-Horvat P. (2019) Quantitative CT assessment identifies more heart transplanted patients with progressive coronary wall thickening than standard clinical read. *J Cardiovasc Comput Tomogr*, 13: 128-133. **IF: 3.316**
  18. Karolyi M, Szilveszter B, **Kolossvary M**, Takx RA, Celeng C, Bartykowszki A, Jermendy AL, Panajotu A, Karady J, Raaijmakers R, Giepmans W, Merkely B, Maurovich-Horvat P. (2017) Iterative model reconstruction reduces calcified plaque volume in coronary CT angiography. *Eur J Radiol*, 87: 83-89. **IF: 2.843**
  19. **Kolossvary M**, Szilveszter B, Merkely B, Maurovich-Horvat P. (2017) Plaque imaging with CT-a comprehensive review on coronary CT angiography based risk assessment. *Cardiovasc Diagn Ther*, 7: 489-506. **IF: 0.000**
  20. **Kolossvary M**, Szekely AD, Gerber G, Merkely B, Maurovich-Horvat P. (2017) CT Images Are Noninferior to Anatomic Specimens in Teaching Cardiac Anatomy-A Randomized Quantitative Study. *J Am Coll Radiol*, 14: 409-415 e402. **IF: 3.393**
  21. **Kolossvary M**, Kellermayer M, Merkely B, Maurovich-Horvat P. (2018) Cardiac Computed Tomography Radiomics: A Comprehensive Review on Radiomic Techniques. *J Thorac Imaging*, 33: 26-34. **IF: 2.078**
  22. **Kolossvary M**, De Cecco CN, Feuchtner G, Maurovich-Horvat P. (2019) Advanced atherosclerosis imaging by CT: Radiomics, machine learning and deep learning. *J Cardiovasc Comput Tomogr*, 13: 274-280. **IF: 3.316**
  23. Korosi B, Vecsey-Nagy M, **Kolossvary M**, Nemcsik-Bencze Z, Szilveszter B, Laszlo A, Batta D, Gonda X, Merkely B, Rihmer Z, Maurovich-Horvat P, Eorsi D, Torzsa P, Nemcsik J. (2019) Association between Cyclothymic Affective Temperament and Age of Onset of Hypertension. *Int J Hypertens*, 2019: 9248247. **IF: 1.865**
  24. Kovacs A, Molnar AA, **Kolossvary M**, Szilveszter B, Panajotu A, Lakatos BK, Littvay L, Tarnoki AD, Tarnoki DL, Voros S, Jermendy G, Sengupta PP, Merkely

- B, Maurovich-Horvat P. (2018) Genetically determined pattern of left ventricular function in normal and hypertensive hearts. *J Clin Hypertens (Greenwich)*, 20: 949-958. **IF: 2.444**
25. Kovacs K, Szakmar E, Meder U, **Kolossvary M**, Bagyura Z, Lamboy L, Elo Z, Szabo A, Szabo M, Jermendy A. (2017) [Hypothermia treatment in asphyxiated neonates - a single center experience in Hungary]. *Orv Hetil*, 158: 331-339. **IF: 0.322**
26. Lakatos A, **Kolossvary M**, Szabo M, Jermendy A, Bagyura Z, Barsi P, Rudas G, Kozak LR. (2018) Novel structured MRI reporting system in neonatal hypoxic-ischemic encephalopathy - issues of development and first use experiences. *Ideggyogy Sz*, 71: 265-276. **IF: 0.113**
27. Lakatos A, **Kolossvary M**, Szabo M, Jermendy A, Barta H, Gyebnar G, Rudas G, Kozak LR. (2019) Neurodevelopmental effect of intracranial hemorrhage observed in hypoxic ischemic brain injury in hypothermia-treated asphyxiated neonates - an MRI study. *BMC Pediatr*, 19: 430. **IF: 1.983**
28. Maurovich-Horvat P, Tarnoki DL, Tarnoki AD, Horvath T, Jermendy AL, **Kolossvary M**, Szilveszter B, Voros V, Kovacs A, Molnar AA, Littvay L, Lamb HJ, Voros S, Jermendy G, Merkely B. (2015) Rationale, Design, and Methodological Aspects of the BUDAPEST-GLOBAL Study (Burden of Atherosclerotic Plaques Study in Twins-Genetic Loci and the Burden of Atherosclerotic Lesions). *Clin Cardiol*, 38: 699-707. **IF: 2.431**
29. Nemcsik J, Vecsey-Nagy M, Szilveszter B, **Kolossvary M**, Karady J, Laszlo A, Korosi B, Nemcsik-Bencze Z, Gonda X, Merkely B, Rihmer Z, Maurovich-Horvat P. (2017) Inverse association between hyperthymic affective temperament and coronary atherosclerosis: A coronary computed tomography angiography study. *J Psychosom Res*, 103: 108-112. **IF: 2.947**
30. Szelid Z, Lux A, **Kolossvary M**, Toth A, Vago H, Lendvai Z, Kiss L, Maurovich-Horvat P, Bagyura Z, Merkely B. (2015) Right Ventricular Adaptation Is Associated with the Glu298Asp Variant of the NOS3 Gene in Elite Athletes. *PLoS One*, 10: e0141680. **IF: 3.057**

31. Szilveszter B, Elzomor H, Karolyi M, **Kolossvary M**, Raaijmakers R, Benke K, Celeng C, Bartykowszki A, Bagyura Z, Lux A, Merkely B, Maurovich-Horvat P. (2016) The effect of iterative model reconstruction on coronary artery calcium quantification. *Int J Cardiovasc Imaging*, 32: 153-160. **IF: 1.896**
32. Szilveszter B, **Kolossvary M**, Karady J, Jermendy AL, Karolyi M, Panajotu A, Bagyura Z, Vecsey-Nagy M, Cury RC, Leipsic JA, Merkely B, Maurovich-Horvat P. (2017) Structured reporting platform improves CAD-RADS assessment. *J Cardiovasc Comput Tomogr*, 11: 449-454. **IF: 3.095**
33. Szilveszter B, Nagy AI, Vattay B, Apor A, **Kolossvary M**, Bartykowszki A, Simon J, Drobni ZD, Toth A, Suhai FI, Merkely B, Maurovich-Horvat P. (2019) Left ventricular and atrial strain imaging with cardiac computed tomography: Validation against echocardiography. *J Cardiovasc Comput Tomogr*, 2019: 1-7. **IF: 3.316**
34. Szilveszter B, Oren D, Molnar L, Apor A, Nagy AI, Molnar A, Vattay B, **Kolossvary M**, Karady J, Bartykowszki A, Jermendy AL, Suhai FI, Panajotu A, Maurovich-Horvat P, Merkely B. (2019) Subclinical leaflet thrombosis is associated with impaired reverse remodelling after transcatheter aortic valve implantation. *Eur Heart J Cardiovasc Imaging*, In press: In press. doi: 10.1093/ehjci/jez256. **IF: 5.260**
35. Varga A, Di Leo G, Banga PV, Csobay-Novak C, **Kolossvary M**, Maurovich-Horvat P, Huttli K. (2019) Multidetector CT angiography of the Circle of Willis: association of its variants with carotid artery disease and brain ischemia. *Eur Radiol*, 29: 46-56. **IF: 3.962**

## 11. ACKNOWLEDGEMENTS

I would like to extend my sincerest gratitude and appreciation to all those who made this PhD thesis possible.

First and foremost, I would like to thank to my mentor and supervisor Pál Maurovich-Horvat for his guidance and continued support during my student researcher and PhD years. I would like to also express my sincere gratitude to Prof. Béla Merkely for giving me the opportunity to carry out my research projects and who provided the background required for my research. I would also like to express my sincerest gratitude to Prof. Shenghan Lai from Johns Hopkins University from who I have learnt a great lot about statistics and also humbleness and decency needed for scientific research.

I am also grateful to my friends: Bálint Szilveszter, Judit Simon and Júlia Karády for all the encouragement and support they gave to me during my PhD years. I would like to also thank all the student researchers at the Cardiovascular Imaging and Research Group, especially Lili Száraz and Milán Vecsey-Nagy. Without them none of our achievements would have been possible.

Finally, I would like to thank to my Parents and my Brother for helping in whatever way they could whenever I needed it.